Title

Systemic Therapy of Inactivated-Bisphosphonate-Conjugated PEGylated NELL-1 (BP-NELL-PEG) for Spaceflight-Induced Osteoporosis

Permalink

https://escholarship.org/uc/item/0bk9h299

Author

Shi, Jiayu

Publication Date

2019

UNIVERSITY OF CALIFORNIA

Los Angeles

Systemic Therapy of Inactivated-Bisphosphonate-Conjugated PEGylated NELL-1 (BP-NELL-PEG) for Spaceflight-Induced Osteoporosis

A dissertation submitted in partial satisfaction of the

requirements for the degree Doctor of Philosophy

in Oral Biology

by

Jiayu Shi

2019

ABSTRACT OF THE DISSERTATION

Systemic Therapy of Inactivated-Bisphosphonate-Conjugated PEGylated NELL-1 (BP-NELL-PEG) for Spaceflight-Induced Osteoporosis

by

Jiayu Shi

Doctor of Philosophy in Oral Biology

University of California, Los Angeles, 2019

Professor Kang Ting, Chair

Osteoporosis affects more than 200 million people worldwide. Therapeutic approaches to osteoporotic bone loss have focused primarily on anti-resorptive agents but with significant clinical limitations. Therefore, there is pressing need to develop new agents, particularly anabolic therapies that promote bone formation. Microgravity-induced bone loss is an important medical consideration of long-duration space flight and has been measured to degrade bone at a rate up to four times faster than disuse atrophy on Earth. As such, the microgravity model of osteoporosis serves as a proxy for extreme cases of disuse osteoporosis on the ground.

NELL-1 is a potent pro-osteogenic protein most studied for its local bone forming effects. Studies have demonstrated that recombinant NELL-1 acts as a combined anabolic and anti-osteoclastic agent to protect against osteoporotic bone loss. In addition, through PEGylation, we successfully increased the circulation half-life of NELL-1 (NELL- PEG) to be up to six times longer. In this study, the therapeutic effects of NELL-PEG were further amplified by conjugation with inactivated bisphosphonate (BP) to increase bone binding affinity. We verified inactivated BP acts *only* as a targeting molecule to optimize NELL-PEG deposition in bone and does *not* exert its own anti-osteoclastic effect. This has led to my **central hypothesis that systemic BP-NELL-PEG therapy will prevent bone loss and promote new bone formation in long-duration spaceflight**. This study was a part of the Rodent Research 5 spaceflight mission and supported by the Center for the Advancement of Science in Space (CASIS) and the National Aeronautics and Space Administration (NASA).

I tested my hypothesis through two AIMs: (1) Pre-Flight **Ground Operation** to optimize the delivery route and dose of systemic BP-NELL-PEG for the reversal of ovariectomy (OVX)-induced osteoporosis in mice; (2) **Flight Operation** to examine the effects of optimized systemic delivery of BP-NELL-PEG for the reversal of microgravity-induced osteoporosis in mice. Results showed that systemic BP-NELL-PEG therapy successfully prevented bone loss from long-duration spaceflight by promoting new bone generation. Furthermore, our findings with inactivated BP conjugation introduce a promising platform for improving skeletal delivery of systemic therapeutics for bone diseases.

The dissertation of Jiayu Shi is approved.

Wenyuan Shi

Chia Soo

Shen Hu

Kang Ting, Committee Chair

University of California, Los Angeles

2019

TABLE OF CONTENTS

LISTS OF FIGURES AND TABLES

ACKNOWLEDGEMENTS

This PhD dissertation would not have been possible without the generous support of the many friends and role models I have encountered throughout the program. First and foremost, I would like to thank Dr. Kang Ting for his excellent mentorship over the last 5 years; his guidance both in research and in life has shaped my development into a capable, confident scientist and person. Especially meaningful to me was his willingness to contribute to my tuition, demonstrating the lengths a caring mentor would go to to ensure the success of a student. I would like to also thank Dr. Wenyuan Shi, Dr. Chia Soo and Dr. Shen Hu, who I am honored to have had as committee members, and whose advice, insights, guidance, and encouragement created a nurturing and stimulating environment for personal and intellectual growth. I would like to thank Dr. Jin Hee Kwak, Project Manager for the Rodent Research 5 mission, and Dr. Xinli Zhang for their support and care, and Dr. Benjamin Wu and Dr. Yulong Zhang from the UCLA Samueli School of Engineering for their guidance and collaboration during my PhD project.

My accomplishments are the result of group effort, achieved only through the support and contributions of superb lab members and dear friends. I want to thank all current and past members of the Ting Lab for their dedicated support and stimulating discussions. I would like to especially thank Dr. Pin Ha and Dr. Hsin-Chuan Pan for their love and care in my personal life and their great support in my experiments. I also would like to thank Mr. Luan Tran and Dr. Tam Duong for their generous help in data analysis. Many thanks to Mr. Matthew Dingman in the Oral Biology department for his patience and guidance in the circumvention of countless difficult administrative situations. I would like to thank NIH, AAOF and CASIS for supporting my research (grant number: NIH/NIDCR K08DE026805, NIH/NIAMS R01AR066782, R01AR068835, R01AR061399, UCLA/NIH CTSI UL1TR000124, CASIS GA-2014-154, AAOF's OFDFA and BRA awards and

Colgate's CARE award for J.H.K.). I would like to acknowledge the journal, *Tissue Engineering Part C: Methods* and the publisher *Mary Ann Liebert, Inc., New Rochelle, NY.* for allowing me to include my published data from "Guidelines for Dual Energy X-Ray Absorptiometry Analysis of Trabecular Bone-Rich Regions in Mice: Improved Precision, Accuracy, and Sensitivity for Assessing Longitudinal Bone Changes". Portions of the **Discussion section (3.1.5-3.1.10),** have been adapted from a co-authored article, "Efficacy of Intraperitoneal Administration of PEGylated NELL-1 for Bone Formation" published in *BioResearch Open Access*, 2016;5(1):159-70. Epub 2016/06/30. doi: 10.1089/biores.2016.0018. PubMed PMID: 27354930; PMCID: PMC4921932.

Finally, I would like to acknowledge my family for their accommodation and support during my studies. I would not have made it this far without you.

BIOGRAPHICAL SKETCH

Name: Jiayu Shi

Education and Training

Institution	Degree or Position	MM/YY	Field of Study
Sichuan University, West China School of Stomatology	D.D.S	09/2009 - 06/2014	Dentistry
University of California, Los Angeles, School of Dentistry	Ph.D. Program	09/2014 - Present	Oral Biology
University of California, Los Angeles, School of Dentistry	Orthodontics Resident	07/2017 - Present	Orthodontics

Position and Employment

2014-Present	Graduate Student, Division of Oral Biology, UCLA School of Dentistry
2017-Present	Orthodontics Resident, Department of Orthodontics, UCLA School of Dentistry

Other Experience and Professional Memberships

2014-Present	Student Member, American Association of Dental Research (AADR)
2015-Present	Student Member, American Society for Bone and Mineral Research (ASBMR)
2017-Present	Resident Member, American Association of Orthodontics (AAO)

Publications

1. **Shi J**, Lee S, Pan HC, Mohammad A, Lin A, Guo W, Chen E, Ahn A, Li J, Ting K, Kwak JH. Association of Condylar Bone Quality with TMJ Osteoarthritis. Journal of dental research. 2017;96(8):888-94. Epub 2017/05/10. doi: 10.1177/0022034517707515. PubMed PMID: 28476093; PMCID: PMC5502961.

2. **Shi J**, Lee S, Uyeda M, Tanjaya J, Kim JK, Pan HC, Reese P, Stodieck L, Lin A, Ting K, Kwak JH, Soo C. Guidelines for Dual Energy X-Ray Absorptiometry Analysis of Trabecular Bone-Rich Regions in Mice: Improved Precision, Accuracy, and Sensitivity for Assessing Longitudinal Bone Changes. Tissue engineering Part C, Methods. 2016;22(5):451-63. Epub 2016/03/10. doi: 10.1089/ten.TEC.2015.0383. PubMed PMID: 26956416; PMCID: PMC4870654.

3. **Shi JY**, Zhou H, Mao RY, Chen Y, Li JT, Huo HY. A preliminary study on the key factors contributing to the attractive lips of Chinese children. Asian Pacific journal of tropical medicine. 2012;5(4):318-22. Epub 2012/03/28. doi: 10.1016/s1995-7645(12)60047-9. PubMed PMID: 22449526.

4. **Shi J**, Shi B, Zheng Q, Yin H. [Magnetic resonance imaging of the levator veli palatini of the cleft palate patients after operation]. Zhonghua kou qiang yi xue za zhi = Zhonghua kouqiang yixue zazhi = Chinese journal of stomatology. 2010;45(10):587-91. Epub 2010/12/24. PubMed PMID: 21176592.

5. Zhang BH, **Shi JY**, Lin YS, Shi B, Jia ZL. VAX1 gene associated non-syndromic cleft lip with or without palate in Western Han Chinese. Archives of oral biology. 2018;95:40-3. Epub 2018/07/27. doi: 10.1016/j.archoralbio.2018.07.014. PubMed PMID: 30048854

6. Li L, **Shi JY**, Zhu GQ, Shi B. MiR-17-92 cluster regulates cell proliferation and collagen synthesis by targeting TGFB pathway in mouse palatal mesenchymal cells. Journal of cellular biochemistry. 2012;113(4):1235-44. Epub 2011/11/19. doi: 10.1002/jcb.23457. PubMed PMID: 22095742.

7. Meng T, **Shi JY**, Wu M, Wang Y, Li L, Liu Y, Zheng Q, Huang L, Shi B. Overexpression of mouse TTF-2 gene causes cleft palate. Journal of cellular and molecular medicine. 2012;16(10):2362-8. Epub 2012/02/07. doi: 10.1111/j.1582-4934.2012.01546.x. PubMed PMID: 22304410; PMCID: PMC3823429.

8. Tanjaya J, Zhang Y, Lee S, **Shi J**, Chen E, Ang P, Zhang X, Tetradis S, Ting K, Wu B, Soo C, Kwak JH. Efficacy of Intraperitoneal Administration of PEGylated NELL-1 for Bone Formation. BioResearch open access. 2016;5(1):159-70. Epub 2016/06/30. doi: 10.1089/biores.2016.0018. PubMed PMID: 27354930; PMCID: PMC4921932.

1 INTRODUCTION

1.1 Review of Osteoporosis

1.1.1 Osteoporosis and Current Therapies

Osteoporosis is the most common metabolic bone disease and affects over 200 million people worldwide with 10 million people affected in the United States alone[1-6]. It contributes to approximately 1.5 million fractures annually, resulting in over $25 billion in medical care spending per annum[7]. The biomedical impact of osteoporosis and its associated complications is immense, and predicted to cost over $25 billion worldwide by 2025[8-10]. Current treatments aim either to prevent bone resorption (anti-resorptive agents) or to enhance bone formation (anabolic agents)[11, 12]. Although several approved anti-resorptive agents exist, including bisphosphonates (BP) and RANK ligand antibodies, each demonstrates a limiting side effect profile. Furthermore, these agents do not induce bone formation[13-15]. The only FDA-approved anabolic therapy is parathyroid hormone (PTH)[12, 16-18], however its use is limited to 24 months due to multiple, unwanted side effects—including risk of osteosarcoma, as determined from rat preclinical studies[19]. Consequently, there is pressing need to develop innovative therapies that will promote bone formation with improved efficacy and safety for the treatment of osteoporosis.

1.1.2 Signaling Pathways in Bone Homeostasis

Wnt/β-catenin signaling is a key regulator in bone homeostasis. Broadly, osteoporosis occurs from excessive bone resorption resulting from imbalance between osteoblast (OB) and osteoclast (OC) activities. Among a multitude of signaling pathways, β-catenin dependent wingless protein signaling has emerged as a critical component in governing OB and OC activity during fracture repair, bone maintenance, and skeletal development[20, 21]. The presence or absence of Wnt signaling determines the fate of β-catenin. When Wnt signaling is active, increased levels of β-catenin can mobilize to the nucleus and ultimately activate Wnt target genes[22-24]. Osteoporosis can result from reduced Wnt signaling activity, while increased Wnt signaling via inactivation of endogenous Wnt inhibitors (i.e. Dkk1 or Sclerostin) can lead to increased OB number and activity, reduced OC number and activity, and consequent increases in BMD[20, 21]. Manipulation of Wnt/β-catenin signaling offers therapeutic opportunities for effectively treating bone pathologies. However, developing Wnt ligands to directly activate Wnt/β-catenin has been challenging. In particular, recombinant Wnt proteins are not suitable for clinical settings, owing to their high lipophilicity and insolubility[25-27]. The insolubility of Wnt proteins challenges its production and clinical delivery, since it requires lipid vesicle tethering[28] for bioactive delivery[20, 29]. Research efforts have therefore focused on the inhibition of Wnt inhibitors, such as Dkk1, GSK3β, and Sclerostin, via neutralizing antibodies and small molecules. However, tissue-specific targeting and long-term safety remain a current challenge[30], thus novel approaches to activate Wnt signaling would constitute significant breakthrough.

1.1.3 Microgravity-induced Osteoporosis

Microgravity-induced bone loss is an important medical consideration of long-duration space flight[31-34]. The microgravity environment serves as a proxy for extreme cases of osteoporosis resulting from disuse atrophy from long-duration bedrest immobilization, injury, illness, or casting on the ground. The **central hypothesis of this study is that systemic BP-NELL-PEG therapy will protect against bone loss and promote new bone formation in long-duration spaceflight**. This study was a part of the Rodent Research 5 spaceflight mission, supported by the Center for the Advancement of Science in Space (CASIS) and the National Aeronautics and Space Administration (NASA). The central hypothesis was tested in two AIMs: (1) Pre-Flight **Ground Operation** to optimize the systemic BP-NELL-PEG delivery method and dose for the reversal of ovariectomy (OVX)-induced osteoporosis in mice; (2) **Flight Operation** to examine the effects of optimized systemic BP-NELL-PEG delivery in the reversal of microgravity-induced osteoporosis in mice. SpaceX CRS-11 (SpaceX-11) was the rocket used for Flight Operations, and was successfully launched on June 3rd, 2017.

We utilized a spaceflight-induced osteoporosis model in aged mice because it provides three key benefits. [1] Microgravity generates an extreme state of osteoporosis that is not replicable by a single osteoporosis model on the ground. According to the International Osteoporosis Foundation, 1 out of 3 women over 50 will experience osteoporotic fractures, as will 1 out of 5 men[35-37]. On average, while we lose around 0.5% of bone per year after the age of 50, astronauts lose around 1.5% of bone per month spent in space[38, 39], which is 36 folds more than on Earth. With respect to the rate of bone loss in mice, we obtained micro computed tomography (micro-CT) and dual-energy x-ray absorptiometry (DXA) data from two recent spaceflight mouse studies in similar research settings to ours (data not shown, courtesy of University of Colorado and University of North Carolina) and confirmed that (i) older mice (8 months old, middle-age female, B6 strain) lose bone volume and density four times faster than by ovariectomy (OVX) on the ground (micro-CT-measured bone mineral density (BMD) and bone volume/tissue volume (BV/TV) reduced by 15% and 30%, respectively, in RR-1 mission) and (ii) younger mice (3 months old, young adult female, B6 strain) lose twice as much bone density than by OVX on the ground (DXA-measured BMD decreased by 20%, in RR-2 mission). As such, we expected a considerable amount of bone loss in a spaceflight-induced osteoporosis model. [2] Microgravity also accelerates the cellular and physiologic effects of aging. Exposure to microgravity induces rapid degeneration in various cell systems that mimic aging in older populations. Thus, it can be considered an excellent model for degenerative diseases and allows us to efficiently study biological processes that occur in the normal aging process[40-42]. [3] Another benefit of utilizing a microgravity model for this study is that it allows investigation of key mechanisms for osteoporosis while excluding the factor of estrogen deficiency, since the most common way of inducing osteoporosis on the ground is by ovariectomy (OVX).

1.2 Review of NELL-1

1.2.1 What is NELL-1

NEL-like molecule-1 (NELL-1) is a unique secretory molecule and was first implicated in bone formation by its overexpression in human craniosynostosis[43]. NELL-1 is a 700 kDa protein that is recognized to be potently pro-osteogenic [43, 44] and is most often studied for its local bone forming effects[45-51]. Previously, an association between NELL-1 and osteoporosis was described, where a genome-wide linkage study identified NELL-1 polymorphisms in patients with reduced BMD[52].

Consistent with this, we have discovered a protective role of NELL-1 in bone maintenance. While complete Nell-1 deficiency results in neonatal lethality[49], mice haplo-insufficient for Nell-1 (generated by N-ethyl-N-nitrosourea (ENU)-induced mutagenesis), develop an osteoporotic phenotype with age. This includes a reduction in BMD of the lumbar spine (as determined by micro-CT), as well as reduced bone anabolism (as measured by F18 radioisotope uptake, a surrogate measure of bone formation activity). This newly discovered protective function of NELL-1 signaling led us to pursue the therapeutic use of recombinant (r)NELL-1 for the reversal of osteoporosis.

Our preliminary studies indicate that, like Wnt/β-catenin, NELL-1 can also act as a combined anabolic and anti-osteoclastic agent to protect against osteoporotic bone loss. Not only are Nell-1 deficient mice more prone to osteoporosis, but local delivery of rNELL-1 also reverses osteoporotic bone loss in both small and large animal models[48, 53]. For example, in a femoral intramedullary injection model, local rNELL-1 treatment significantly increased trabecular and endosteal bone formation in rats[48]. rNELL-1 induces robust osseous healing of critical-sized rat femoral segmental and calvarial defects[45, 54, 55,56]. rNELL-1 also promotes lumbar spinal fusion in rats, sheep[49-51], and non-human primates[57]. In addition, the bone forming effects of rNELL-1 have been verified by other independent research groups[58, 59]. We have also expanded the known functions of rNELL-1 to include suppression of OC activity, promotion of mesenchymal stem cell (MSC) numbers, and suppression of adipogenesis[53, 60] .

Mechanistically, Nell-1selectively promotes osteochondroprogenitor cells and BMSC differentiation[44]. Alternatively, rNELL-1 protein induces osteoblastic differentiation, apoptosis, and mineralization only in the pre-osteoblastic cell lines and primary calvarial cells, but not in the fibroblastic cell line[61, 62]. Also, while Nell-1 was overexpressed in the MC3T3 cells, the expression level of early gene markers for osteobastogenic differentiation (Alp and osterix) were inhibited, which indicates that Nell-1 may act to promote bone differentiation at a relatively late stage. Nell-1 can drive the differentiation of BMSCs towards osteochondral lineage *in vitro* and endochondral bone formation *in vivo*[44]. Previous findings demonstrated that Nell-1 selectively promotes osteochondral differentiation in both cells of osteochondrogenic lineage and multipotent cells. Additionally, NELL-1 is directly regulated by Runx2 while also functioning as a downstream mediator of Runx2[55]. Lastly, NELL-1 can activate JNK and ERK pathways to initiate signaling transduction cascades. Regarding cell receptors of NELL-1, NELL-1 binds to the cell surface receptor integrin beta 1[63] and possibly to the receptor Cntnap 4[64]. [Note: *NELL-1* and NELL-1 indicate the human gene and protein, respectively; *Nell-1* and Nell-1 indicate the mouse gene and protein, respectively.]

1.2.2 PEGylation of NELL-1

The technical innovation of NELL-1 based therapy stems from the chemical modification of rNELL-1 for improved pharmacokinetics. Anti-Wnt inhibitors (anti Dkk1 or anti-Sost) in development were tested twice weekly in mice[65]. Systemic delivery of unmodified rNELL-1 given every 48 hours (3-4 doses/week) reversed osteoporotic bone loss in mice[53]. To decrease the frequency of rNELL-1 administration, we explored various PEGylation methods to increase the systemic half-life (t1/2) of rNELL-1. PEGylation is an effective and non-toxic[66-68] chemical process to modify a molecule's physiologic and pharmacokinetic characteristics using polyethylene glycol (PEG). PEGylation of NELL-1 increased plasma half-life in mice and increased the window for bone uptake. The FDA has approved at least 9 marketed PEGylated therapies[66]. After testing three PEGylation methods[69] delivering different PEG sizes and structures (PEG at 5000Da, 20000Da and 40000Da), we found that all three methods maintained osteoinductive bioactivity (82-95% of unmodified rNELL-1, as assessed by in vitro mineralization studies) while increasing the systemic half-life of rNELL-1 from 5.5 hrs to 16-31 hrs (as assessed by enzyme-linked immunosorbent analysis (ELISA) based detection of fluorescein isothiocyanate (FITC) conjugated rNELL-1).

1.2.3 Systemic NELL-PEG Therapy

Previously, systemic delivery of unmodified rNELL-1 administered every-2-days (q2d) reversed osteoporotic bone loss in mice[53]. As a result of PEGylation, systemic NELL-PEG therapy can be administered on a clinically feasible injection schedule. We successfully demonstrated the osteogenic capacity of systemic NELL-PEG to be comparable to that of unmodified rNELL-1 when IV injected either every 4 days (q4d) or every 7 days (q7d) in mice **(Fig. 1)**[70]. Considering that anabolic anti-osteoporosis agents currently in development are administered every 4 days, the success of this research could significantly reduce the treatment cost and improve patient compliance in chronic treatment settings. These exciting results encouraged us to further investigate NELL-PEG as a systemic therapy to treat and prevent osteoporosis. As a result, in this study we aimed to further enhance the pharmacokinetics of NELL-PEG therapy through the conjugation with inactivated BP.

1.3 Bisphosphonate (BP) As a Bone Targeting Molecule

There are numerous bone disease therapeutics on the market and in development. However, systemic drugs need prolonged and maintained concentrations in order to exhibit pharmacological activity at targeted peripheral sites[71]. Additional for consideration is that bone tissues possess a membrane of lining cells, which functions as a marrow-blood barrier, therefore limiting the access of exogenous large molecules to the bone surface[72].

Bisphosphonates (BP) are bone seeking agents that have been very well-characterized in recent years. Both *in vivo* and *in vitro* studies have shown that the main effect of BP is inhibition of bone resorption[73-75]. BP are compounds with a chemical structure similar to that of inorganic pyrophosphate (PPi), an endogenous regulator of bone mineralization[76, 77]. BP are comprised of two phosphonate groups linked by phosphoether bonds to a central (geminal) carbon atom (a P-C-P structure)[71, 76, 78]. Osteoclasts (OC) are highly endocytic during the bone resorption process and BP present in the resorption lacuna is likely to be internalized via endocytic vacuoles[76]. The P-C-P structure of BP is required for the chelation of Ca^{2+} ions by these compounds and hence for their tissue-selective targeting to bone. BP are rapidly and selectively trapped in calcified tissues after entering systemic circulation[79, 80]. A significant and unique feature of OC treated with BP therapy is the lack of a ruffled border[81-86], the convoluted region of plasma membrane adjacent to the bone surface that is essential for the resorption process. BP can also disrupt the cytoskeleton within the OC and cause the loss of actin rings, further inhibiting its functions[82, 87-89] .

After 50 years of clinical use, there are two distinct and clear intracellular mechanisms of BP—discovered in recent decades. A review published by Rogers et al.[90], provides a thorough summary of the signaling pathways involved in BP's effects. For simple BP, studies have provided convincing evidence that clodronate, etidronate and tiludronate act as prodrugs, being converted to AppCptype metabolites following intracellular uptake by OC *in vivo.* The accumulation of these metabolites has a cytotoxic effect on OC, thus inhibiting bone resorption by causing OC apoptosis[91-95]; for nitrogen-containing BP, the enzyme farnesyl pyrophosphate (FPP) synthase is inhibited, thereby disrupting the production of isoprenoid lipids in the mevalonate pathway. This prevents the prenylation of small GTPase proteins necessary for OC function and causes accumulation of toxic, isoprenoid-containing metabolites[96-99]. BP therapy itself is an excellent bone-specific drug-delivery system that can seek target tissue accurately and exert pharmacological effects preferentially on bone[71]. The P-C-P bond in BP is resistant to chemical and enzymatic hydrolysis[100], which helps BP to remain for longer periods of time once bound to bone.

The nitrogen moiety holds a critical role in BP's anti-OC function. Although the phosphate and hydroxyl groups are essential for BP affinity to bone matrix, the nitrogen (in the R2 position of N-BPs) bound to the central carbon is the primary determinant of a BP's potency for inhibition of bone resorption[101]. The presence of a nitrogen amino group can increase the antiresorptive potency by 10 to 10000 fold relative to non-nitrogen-containing BP[102, 103]. Recently determined crystal structures of farnesyl pyrophosphate (FPP) synthase with bound N-BPs revealed that the nitrogen in N-BP can form hydrogen bonds[104]. Interestingly, whereas farnesyl pyrophosphate synthase is ubiquitously expressed in mammalian cells and has a critical role in lipid production, cellular apoptosis induced by nitrogen-containing bisphosphonates appears to occur only in OC[101]. This likely results from bisphosphonates selectively adhering to and remaining within bone, which is the target of osteoclast endocytosis during osteoclast-mediated bone mineral dissolution and matrix digestion[101]. Theoretically, there are two ways to inactivate BP[104]: [1] Change the position of the nitrogen in BP or [2] Completely remove the nitrogen from BP. Changing the position of the nitrogen relative to the bisphosphonate group leads to a disruption in the hydrogen bond geometry of the crystal structure. This usually leads to a loss in initial potency and to a reduced ability to hold the enzyme–inhibitor complex in the isomerized state. With regards to Nitrogen removal, the resulting phenyl analogue shows complete loss of slow-binding kinetics and an overall reduction in potency, an indication that the nitrogen has a role both in the initial competitive phase of the inhibition and in stabilizing the final isomerized state. In this study, during the conjugation of BP to NELL-PEG, the BP is deactivated by altering the position of the nitrogen in BP. This change leads to the non-ideal orientation of the nitrogen atom in the active BP, significantly decreasing its pharmacological activity.

Due to the excellent bone binding characteristics of BP, we sought to use inactivated BP as a bone targeting molecule to be conjugated with the NELL-PEG protein. The efficiency and potency of this new systemic BP-NELL-PEG therapy was tested from multiple aspects in the following study.

2 MATERIALS AND MAETHODS

2.1 Experimental Groups

All mice were handled according to the guidelines of the Chancellor's Animal Research Committee at UCLA and NASA Institutional Animal Care and Use Committees (IACUC). The mice housed at UCLA were in pathogen-free ventilated cages, in a light and temperature-controlled environment, and were fed ad libitum.

2.1.1 Ground Operation

A. Develop new DXA guidelines

Previously, no standardized guideline for mice DXA imaging and analysis existed. Therefore, we developed a new guideline to help improve the accuracy and consistency of mice DXA usage and published this guideline in Tissue Engineering Part C, Method (2016;22(5):451-63)[105].

30 12-week-old female BALB/c mice were purchased from Charles River Laboratories.

B. Establish the bone maturation timeline of female BALB/c mice

24 12-week-old female BALB/c mice (Taconic Biosciences, NY) were used in this study to plot out the bone maturation timeline of this strain. 6 mice were harvested at each time point (week 0 (12-week-old), week 4 (16-week-old), week 14 (26-week-old) and week 20 (32-week-old)).

C. Pharmacokinetics Study

Since the white fur of BALB/c mice would interfere with optical imaging signals, CD-1 mice (black fur) were used in the NELL-1 biodistribution study.

20 12-week old female CD-1 mice (Charles River Laboratories, MA) were used for the NELL-1 biodistribution study, grouped as below:

(1) Control: Injected with saline (n=5)

(2) NELL-1 group: Injected with 1.25mg/kg rNELL-1 protein (n=5)

(3) NELL-PEG group: Injected with 1.25mg/kg NELL-PEG (n=5)

(4) BP-NELL-PEG group: Injected with 1.25mg/kg BP-NELL-PEG (n=5)

The 1.25mg/kg dose for all groups was based on NELL-1 protein content. For BP-NELL-PEG conjugation process, the ratio of the three components were maintained at 3:1:19.

All 20 mice were injected with the solution via lateral tail vein (100ul IV bolus dose) 48h before examination. The protein was labeled with VivoTag 680XL first and administered to the mice at a dose of 1.25 mg/kg. Organs were collected at 48h and imaged by the IVIS (In Vivo Imaging System) imaging system.

D. NELL-1 Based Therapy Optimization Studies

165 16-week-old female BALB/c mice (Taconic Biosciences, NY) were used. 16-week-old animals were used as studies have shown that mice of this strain reached young adulthood by 12-16 weeks of age. A sample size of at least 8 mice per group were used in all experiments. The detailed animal groups for each study are listed below.

1. Systemic Administration Route for NELL-1 Therapy
    (1) SHAM group: the non-osteoporotic control group
    (2) OVX group: the osteoporotic control group
    (3) Treatment groups:
        a. IP Injected with NELL-PEG at 10mg/kg dose
        b. SC Injected with NELL-PEG at 10mg/kg dose
2. Effective Treatment Dose of NELL-PEG Therapy
    (1) SHAM group: the non-osteoporotic control group
    (2) OVX group: the osteoporotic control group

(3) Treatment groups:

    a. Injected with NELL-PEG at 5mg/kg dose
    b. Injected with NELL-PEG at 10mg/kg dose

3. Treatment Effects Comparison Between NELL-PEG and BP-NELL-PEG

(1) SHAM group: the non-osteoporotic control group

(2) OVX group: the osteoporotic control group

(3) Treatment groups:

    a. Injected with NELL-PEG at 10mg/kg dose
    b. Injected with BP-NEL-PEG at 5mg/kg
    c. Injected with BP-NELL-PEG at 10mg/kg

4. Conjugated Bisphosphonates Has No Therapeutic Effects

(1) SHAM group: the non-osteoporotic control group

(2) OVX group: the osteoporotic control group

(3) Carrier control group: injected with BP-bovine serum albumin (BP-BSA) at 5.11 mg/kg dose. The component ratio of BP to BSA was 3:1 in the BP-BSA conjugation and the total molar concentration of BP molecules of BP-BSA was 5.11mg/kg; identical to the 10mg/kg BP-NELL-PEG group.

(4) Treatment groups:

    a. Injected with BP-NELL-PEG at 5mg/kg dose
    b. Injected with BP-NELL-PEG at 10mg/kg dose

2.1.2 Flight Operation

120 32-week-old female BALB/c mice (Taconic Biosciences, NY) were used. 32 weeks of age was selected based on our ground preparation study which showed that female BALB/c mice

reached their bone density plateau after 32 weeks of age. All mice were housed at Kennedy Space Center (KSC) for 4 weeks before rocket launch and were randomly divided into groups as shown in **Table 1**. On June 3rd, 2017, KSC-housed mice were transported to the ISS as part of SpaceX CRS-11. At 5 weeks and half-way through the research mission, half of the Flight group mice (n=20) were live-returned to earth and transported to the animal care facility at UCLA to continue therapy for 4 additional weeks. Half of the Ground group mice (n=20) housed at KSC were also transferred to UCLA for the same continued therapy. All mice returned to UCLA (n=40 in total) in this time period are referred to as the **Live-return groups (LAR)**. The other halves of Flight group (n=20) and Ground group mice (n=20) were kept on the ISS or at KSC for the full 9 weeks of experimentation (n=40 in total) and are referred to as the **Terminal groups (TERM)**. Starting at 1 week in orbit and every other week thereafter, mice received either PBS or BP-NELL-PEG injections. All treatment time points of the Ground control mice matched exactly with the Flight group mice in space. At the end of the study, all mice were euthanized. Carcasses from the remaining groups on the ISS and in KSC were frozen and later returned to UCLA for multi-team dissection and analyses **(Fig. 2).**

2.2 Surgical Procedures

2.2.1 OVX & SHAM Surgery

Animals were housed in a light- and temperature-controlled environment and given food and water ad libitum. All animals were handled in accordance with guidelines of the UCLA Chancellor's Animal Research Committee of the Office for Protection of Research Subjects.

(1) Ovariectomy (OVX). Buprenorphine was injected prior to any surgical incision. Mice were anesthetized by 1.5% isoflurane inhalation in the chamber. A 3cm x 3cm area was shaved from the iliac crest for each mouse. A 2cm dorsal incision between the bottom of the rib cage and the

front of the hind limbs was made on the flank of each mouse. The tip of a double sharp scissors was inserted through the muscle layer to separate the muscle fibers. The ovaries were grasped by the surrounding fat pads and pulled through the incision with blunt tweezers. High-temperature surgical cautery (Bovie Medical, Clearwater, FL) was used to dissect out the ovary and oviduct. The adipose tissue was replaced into the abdominal cavity after confirming hemostasis. The skin incision was closed using 4-0 vicryl sutures. Another incision was made in the contralateral fascia and the above procedures were repeated.

(2) SHAM. All the steps were performed as with OVX surgery until the fat pad was pulled through the incision with blunt tweezers. The fat pad was replaced into the abdominal cavity without removal of the ovary and oviduct. The skin incision was closed using 4-0 vicryl sutures. Another incision was made in the contralateral fascia and the above procedures were repeated.

2.2.2 Injection Procedures

(1) Intraperitoneal (IP) injection. Gently grab one mouse from the cage and restrain appropriately in the head-down position. The top of multi-dose vial was disinfected with 70% alcohol. The amount of solution to be administered (pre-warm if possible) was drawn up into the syringe. The injection site was in the animal’s lower right quadrant of the abdomen to avoid damage to the urinary bladder, cecum and other abdominal organs. Insert needle with bevel facing “up” towards the lower right quadrant of the abdomen. Insert needle to the depth until the entire bevel is within the abdominal cavity.

(2) Subcutaneous (SC) injection. Repeat the same steps as above for animal handling and disinfection. Hold the mouse on a flat surface and insert the needle into the loose skin over the neck and shoulder area.

2.2.3 Harvesting and Organs Retrieval Procedures

At the end of each experimental procedure, we harvested critical organs, tissues, and bones, listed below, from each mouse. Organs and tissues were dedicated for pathological evaluation while bone samples were reserved for micro-CT scanning and histological analysis. Each mouse was sacrificed by CO2 (3L/min) displacement of oxygen, continued for one minute after breathing stopped, and subsequent cervical dislocation to ensure euthanasia. Each mouse was dissected using precision forceps to carefully separate out each of the following organs and bone samples:

- Organs: liver, heart, ovary, lung, intestine, kidney, stomach, pancreas
- Bone samples: humerus, femur, tibia, lumber spine, cranium
- Tissues: inguinal fat (white fat), abdominal fat (white fat), intrascapular (brown fat)

All samples were placed in 4% paraformaldehyde (PFA) for 48h and transferred to 70% ethanol afterwards.

2.3 Imaging Analysis

2.3.1 High Resolution X-ray Imaging

Radiographs were taken using a high-resolution Faxitron LX-60 Cabinet radiography system at a resolution of 10 lp/mm. High-resolution Faxitron X-ray images of the knee joint and lumbar vertebrae were obtained using a setting of 47 kV. The sedated mice were positioned in the Faxitron just as they were during DXA scans —the standard position described in the new DXA guideline. The location of key anatomic landmarks (e.g., epiphyseal plate) in the distal femur, proximal tibia, and lumbar vertebrae (L5, L6) were defined using the Faxitron images and applied to DXA analyses.

2.3.2 DXA Scan and Analysis

DXA images were acquired and analyzed following the new guidelines we developed[105]. DXA images **(Fig. 3A)** were taken using a PIXImus 2 mouse densitometer (GE Lunar PIXImus) after sedation. The steps to improved DXA image acquisition are as follows: (1) Fast mice overnight to prevent calcified food pockets from appearing in the image. (2) Clean the whole imaging area to avoid any noise caused by animal feces, fur, and so on. (3) Lay the mouse prone with the head in the circular groove of the specimen tray. (4) Ensure that the tail of the mouse does not cross any of the long bones. (5) Move the legs of the mouse away from its body. (6) Apply gentle traction to the tail and back to straighten the spine and ensure that the skull is parallel to the sagittal plane. (7) Set the front legs at a 45 angle to the spine to prevent overlap in image. (8) Abduct the femurs so that when viewing a prone mouse from above the femurs appear at a 90 angle to the spine. (9) Set knees to an angle of 90. (10) Check every image immediately after each DXA scan, and rescan poor quality images **(Fig. 3A)**.

2.3.3 Micro-CT Scan and Analysis

The femurs, tibiae, and lumbar vertebrae were scanned using micro-CT (SkyScan 1172; Bruker Micro-CT N.V.) at an image resolution of 10 um (55 kV and 181 mA radiation source, 0.5mm aluminum filter). Previously published methods[70] were followed for the micro-CT reconstruction and analysis. 3D images were reconstructed from the 2D X-ray projections by implementing the Feldkamp algorithm and appropriate image corrections, including ring artifact correction, beam hardening correction, and fine-tuning, were processed using NRecon software (SkyScan 1172, Belgium). After acquisition and reconstruction of datasets, images were first reoriented on each 3D plane using DataViewer software (SkyScan 1172, Belgium) to align the long axis of the femur, tibia, or lumbar vertebrae parallel to coronal and sagittal planes. Next, 3D morphometric analyses of the distal femur, proximal tibia and the body of lumbar vertebrae were performed using CT-Analyzer software (SkyScan 1172, Belgium). The region of interest (ROI) is specified for each study in the figure legends separately. For trabecular bone analysis, ROIs were delineated using a freehand drawing tool while maintaining 3.5-pixel clearance from the endosteal surface. A clearance of certain distance was maintained from the growth plate (specified in the figure legend for each study). For cortical bone analysis, cortical bone ROIs were generated by taking whole bone ROIs (delineated for the outline of the entire bone, for each bone) and subtracting trabecular bone ROIs, leaving only the cortical bone area. Morphometric parameters were then computed from the binarized images using direct 3D techniques (marching cubes and sphere-fitting methods), and included bone mineral density (BMD, g/cm^3), percent bone volume (BV/TV, %), trabecular number (Tb.N, mm^{-1}), trabecular thickness (Tb.Th, mm) and trabecular separation (Tb.Sp, mm). All quantitative and structural parameters followed the nomenclature and units recommended by the American Society for Bone and Mineral Research (ASBMR) Histomorphometry Nomenclature Committee[106].

2.4 Motor Function Test

Motor Function tests were performed in consultation with UCLA's Behavior Testing Core Facility. Mice were housed five per cage in a room with a 12 hr light/dark cycle (lights on at 7:00 A.M.) with ad libitum access to food and water. Motor function tests were performed between 9:00 A.M. and 6:00 P.M. Mice were handled gently for three to five days prior to testing. All cages were transferred to the behavior testing room 60 min before the first trial began.

The previously described rota rod method described by Shiotsuki et al.[107] was adopted for motor function testing. A rota rod machine with automatic timers and falling sensors (MK-660D, Muromachi-Kikai, Tokyo, Japan) at UCLA's behavioral core facility was used. Mice were placed on a 9cm diameter drum whose surface was covered with hard chloroethylene to prevent gripping. Before training sessions, mice were habituated to stay on the stationary drum for 3 min. Habituation was repeated every day for 1 min just before the session. Rotational acceleration was abandoned and the rotation was set at a relatively slow speed (10 rpm, 2.8 m/min on the surface) to make the task easier for learned animals. Mice were placed back on the drum immediately after falling, up to 5 times in one session. A fall was overlooked when the animal remained on the drum for 180 seconds.

2.5 Histology and Cell Culture

2.5.1 Histology, Immunohistochemical Analysis and TRAP staining

For histology, all samples were fixed in 70% ethanol until completion of micro-CT scanning. Bone samples were decalcified in 19% EDTA solution for 14 days, dehydrated, then processed for paraffin embedding. Five-micron-thick longitudinal sections were cut and the slides were stained with haematoxylin and eosin (H&E), Masson's Trichrome, tartrate-resistant acid phosphatase (TRAP) staining (Sigma-Aldrich) and with markers of OB (osteocalcin (OCN)) and OC (receptor activator of nuclear factor kappa-B ligand (RANKL)) as per standard protocols. Histological and immunohistochemical (IHC) specimens were analyzed using the Olympus BX51 microscopes and images were taken with a MicroFire digital camera and Picture Frame software (Optronics, Goleta, CA).

2.5.2 Dynamic Histomorphometric Analyses

For bone fluorescent-labelling studies, mice were injected intraperitoneally with calcein (20 mg/kg), alizarin red complexon (50 mg/kg), then calcein (20 mg/kg) again at weeks 3, 5 and 7 post-launch, respectively. Femur samples were dissected, fixed in 70% ethanol, dehydrated, embedded, and decalcified in methyl methacrylate. Coronal sections at 5 mm thickness were analyzed using the OsteoMeasure morphometry system (Osteometrics, Atlanta, GA, USA). For dynamic histomorphometry, the mineral apposition rate (MAR, mm per day), which is the distance between the midpoints of the two labels divided by the time interval between the midpoints, were measured in unstained sections under ultraviolet light and used to calculate bone formation rate with a bone surface referent (BFR/BS, $um^3 * um^{-2}$ per year). The bone formation rate per bone surface (BFR/BS) is the volume of mineralized bone formed per unit time and per unit bone surface. The fixed area and location beneath growth plate of distal femur trabecular bone was selected as the ROI (3 measurement fields per sample). All image acquisition and analyses were repeated three times and performed in a blinded manner.

2.5.3 Colony-forming Unit Fibroblast Assay

For the colony-forming unit fibroblasts (CFU-F) assay, bone marrow mesenchymal stem cells (BMSCs) were freshly harvested from left and right humeri by flushing with 27 gauge needles. Isolated marrow cells were seeded on 6-well plates ($1x10^6$ cells/well), and cultured for 14 days in Complete MesenCult Medium (STEMCELL Technologies, Inc., Canada) with osteogenic induction (10mM beta glycerophosphate and 50 mM ascorbic acid, Fisher Scientific, Pittsburgh, PA) at 37 °C with 5% CO2. CFU-F derived colonies were stained using Alkine phosphonate staining kits (Sigma-Aldrinch, USA) first and then Giemsa Staining Solution (EMD Chemicals, Inc., NJ). Colony numbers were counted under a microscope.

2.5.3 Osteoclasts Isolation and Culture

OC were cultured and quantified according to previously described methods by Longaker et al.[108] Bone marrow was flushed from mice humeri, and the remaining bone tissue gently crushed by pestle and mortar in flow cytometry buffer. Bone marrow flush was centrifuged at 200 x g for 5 min at 4 °C to yield a cell pellet which was then resuspended and layered onto commercially available density gradient cell separation media. Isolated marrow cells were seeded on 24-well plate ($2x10^5$ per well) and cultured in macrophage stimulating media (PGE2, Mr 352.465 g/mol at 10^{-7} M, M-CSF at 10ng/ml) for 3 days at 37 °C. OC induction media (PGE2, Mr

352.465 g/mol at 10^{-7} M, M-CSF at 10ng/ml, RANKL at 10ng/ml) was then used for 5-7 days with daily change until large, multinucleated osteoclasts appeared on the culture plate.

2.5.4 TRAP Staining

The TRAP staining was performed per standard methods by Longaker et al.[108] as follows: OC were fixed by adding 4% PFA solution to culture plates and incubated for 1 hr at 4 °C. TRAP stain (Sigma-Aldrinch 387A) was pre-warmed to 37 °C. After 1 hr in PFA, PFA solution was aspirated and the cells washed with PBS. 1 ml of pre-warmed TRAP stain was added into each well. The cell plate was then placed into an incubator at 37 °C for 1 hr and protected from light. After 1 hr, the wells were washed 3 times with pre-warmed deionized water. Gill's Hematoxylin was used to counterstain for 1–2 min, after which the wells were washed with deionized water until adequate color intensity was achieved.

2.5.5 Biomechanical Analysis (Finite element analysis, FEA)

FEA was performed on a bone mesh model generated from micro-CT images which were converted to DICOM files using a SkyScan Dicom Converter software (DicomCT application, Skyscan 1172F, Skyscan). Tetrahedral 3D mesh models were created using a volume of interest (VOI) of distal femur using the ScanIP software (Simpleware Limited). A constant thickness of 1mm was used for all VOIs. FEAs were performed using the ABAQUS software (Dassault Syste`mes) with boundary conditions set as encastre, constrained in all directions. Next, we applied a uniform compressive pressure of 0.5 MPa on the superior surface of the VOI. The force comes from a superior to inferior direction, loading onto the axial cross-section. (This force direction was chosen for the femur as it best simulates normal physiological conditions in humans. The limitation, however, is that in rodents loading is not parallel to the long axis of the femur, as it is in humans). Blue colored regions represent bone regions which are stronger and therefore more resistant to fracture, while yellow and red colored regions represent weaker bone. The von Mises stress experienced and total strain energy of the samples were analyzed.

2.6 BP-NELL-PEG Synthesis

2.6.1 NELL-PEG preparation

In accordance with previously published conjugation methods[109], NELL-PEG was synthesized from linear PEG-NHS Mw 5 k (PEG 5k, Sigma-Aldrich, USA) [69]. Briefly, 0.5 mg of NELL-1 (10 mg/mL) was diluted to a concentration of 2 mg/mL in PBS buffer (pH = 6.5, 0.1 M), then added to 10 ml of 62.5 mg/mL PEG 5k at a NELL-1 to PEG molar ratio of 1:100. The PEGylation system was reacted under 300 rpm magnetic stirring for 12 hrs at 4 °C. The obtained NELL-PEG was purified by loading the reaction mixture onto a Sephadex G-25M column (Sigma-Aldrich, USA), eluting with 3 mL of PBS solution (pH = 7.4), and collecting fractions (0.25 mL/fraction) which mainly consisted of NELL-PEG as determined by GPC method. 24 hrs of dialysis against distilled water was then performed using suitable dialysis cassettes (Fisher, USA) to remove any unreacted PEG molecules.

2.6.2 BP Conjugation and Inactivation

BP-NELL-PEG was synthesized in the following seven steps: (1) BP treatment: BP was dissolved by 5M HCl, precipitated with 95% ethanol, centrifuged (8k rpm, 2 min) to remove supernatant, washed three times with 95% ethanol, and dried in a biohood for 24 hrs; (2) Preparation of stock solution including NELL-PEG (5 mg/ml, 100 mM PBS, pH = 7), NEM stock solution and100 mM Sulfo-SMCC stock solution; (3) NELL-PEG labeled with sulfo-SMCC: NELL-PEG was incubated with 5 mM NEM for 60 min at 4 °C , then reacted with 10 mM Sulfo-SMCC for 5 hrs and dialysis against dd water for 24 hrs at 4 °C ; (4) BP-IT synthesis: treated BP (20 mM in 100 mM PBS, pH = 7) was thiolated with equal volume of IT (10 mM in 100 mM PBS, pH = 7) for 2 hrs; then the mixture was directly added to the above solution and reacted for 3 hrs at 4 °C ; (5) Purification: the product was dialyzed against dd water for 24 hrs at 4 °C (Mwco,12000 Da); (6) lyophilization: transfer the solution in dialysis bag to a glass vial, freeze 24 h, and dry 24 hrs on lyophilizer; (7)Reconstitution: the lyophilized protein was reconstituted by PBS (pH = 7.4), gently vortex (level 1, 1 min) to get dissolved, then stored at -80 °C prior to usage.

The average conjugation ratio of BP-NELL-PEG was estimated by fluorometric assay to be 3:1:19. BP-PEG-NELL solution (1.0 mg/ml, PBS, pH 8.0) was mixed with fluorescamine solution (in DMSO at a concentration of 1.0 mg/mL) and incubated for 15 min at 25 °C. NELL-PEG was used as a control to determine the amount of unreacted amine groups of the BP-NELL-PEG solution. The fluorescence intensity of the solution was determined by plate reader (Infinite F200, Tecan Group Ltd.) at an excitation wavelength of 390 nm and an emission wavelength of 475 nm. The degree of conjugation was calculated by comparing pre-conjugation free amine levels to post-conjugation free amine levels. The protein amount before and after synthesis was determined by GPC (gel permeation chromatograph E2695, waters technologies corporation), and the ratio between them was defined as the yielding ratio (the amount of obtained protein divided by the amount of protein used x 100). NELL-PEG was used as a control in GPC analysis as well. The yielding ratio was estimated to be 90% for NELL-PEG and 80% for BP-NELL-PEG.

2.7 Statistics

Statistics were performed in consultation with the UCLA Institute for Digital Research and Education, Statistical Computing Group. All experiments presented in figures are representative of at least three independent repetitions. Numerical data and histograms are expressed as the mean ± standard error of the mean or mean ± standard deviation. In comparisons between two groups, two tailed Student's t-test was performed. In multiple group comparisons, one way or two-way

ANOVA was employed with Tukey's method as a post-hoc adjustment. The precision of DXA data generated by the new guideline was assessed by intra-class correlation (ICCs) coefficients. The ICCs for one-way random effect models were used to assess intra-observer reliability, and ICCs for two-way random effect models were used to assess inter-observer reliability. To model the trajectory of DXA BMD over time, a linear mixed model was used, with a random intercept term to account for repeated measures within each mouse for each bone site analyzed. In the DXA methodology study, Levene's equal variance test was performed to determine differences between variances of conventional method and new method data sets. The accuracy of DXA BMD and BMC data was assessed by Pearson's correlation coefficient (r) and the standard error of estimate (SEE) of a linear regression. In the Flight Operation DXA analysis, the fixed effects of the linear mixed model include four-way interaction of the factors TIME, BP-NELL-PEG/PBS, FLIGHT/GC, LAR/TERM and all lower-order terms to allow for flexibility in modeling of effects. Linear mixed models were followed by likelihood ratio tests to assess 1) the cumulative contribution of all factors to the fit of the model and 2) the individual contribution of each factor (TIME, BP-NELL-PEG, FLIGHT, LAR) to the fit of the model (by testing model fit against a model where a factor is omitted). When a test for an individual factor was significant, pairwise comparisons were performed to test for specific effects of that factor across levels of the other factors. For lipid count analysis in histology, a linear mixed model was used with random intercept by mouse, and fixed effects of BP-NELL-PEG/PBS, FLIGHT/GC, and their interaction. Pairwise contrasts were then performed to test for specific effects of BP-NELL-PEG/PBS and FLIGHT/GC. All statistical analyses were performed with Stata 14 (StateCorp) software. Only *p*-values less than 0.05 were considered statistically significant.

3 RESULTS AND DISCUSSION

3.1 Ground Operation

3.1.1 Osteoporosis Model on Ground by Ovariectomy

Significant BMD decrease

4 weeks after OVX induction, OVX and SHAM groups were scanned by DXA. As shown in **Fig. 4A-C**, all three bone sites (distal femur, proximal tibia and lumber vertebra) showed significant decreases in BMD, induced by OVX. This confirms successful establishment of the osteoporosis model. Between OVX and SHAM groups, BMD at 4 weeks post-OVX differed by 8.12% at distal femur, 7.76% at proximal tibia and 12.61% at lumbar vertebra ($p < 0.05$).

Uterus Atrophy

Uteri were carefully dissected and weighed from each mouse at time of harvest. OVX groups showed significant uterus atrophy compared to SHAM **(Fig. 4D-E)**.

3.1.2 Establishment of New DXA guideline

This part of study was published in Tissue Engineering Part C, Method (2016;22(5):451-63), Shi & Lee et al.[105]

Anatomic analysis

Anatomic analysis data were acquired from high resolution X-ray images of 60 femurs (30 left, 30 right), 60 tibiae (30 left, 30 right), and 60 lumbar vertebrae (30 L5, 30 L6). The X-ray images revealed that the proximal end of the patella was located 0.47mm (standard deviation [SD] – 0.09) inferior to the epiphyseal plate of the distal femur when the knee was flexed 90 **(Fig. 5A)**. Thus, placing the DXA ROI distal to the femur growth plate excluded the patella from the analysis. The mean distances and angles measured for the distal femur, proximal tibia, and lumbar vertebrae are shown in **Table 2**.

Precision of the new method

Inter-observer reliability tests showed substantial agreement across sites. The distal femur had the highest inter-observer reliability with an ICC of 0.945 followed by proximal tibia (ICC= 0.932) and L6 (ICC= 0.801). L5 had the lowest inter-observer reliability with an ICC of 0.743. These values are similar to inter-observer reliability values across skeletal sites **(Table 3)**.

Longitudinal analysis of BMD for 14 weeks (Fig. 6)

After obtaining longitudinal DXA data from both the new method (i.e., localized ROI) and the conventional method (i.e., broad ROI), linear mixed models were used to reflect the growth trajectory of DXA BMD at each location. Regardless of the method used, models that included the quadratic effects of time yielded the best model fit for distal femur and linear function for proximal tibia and lumbar vertebrae ($p < 0.01$ at all sites). All three sites using either method showed significant changes in DXA BMD over time, compared to baseline.

Although both methods had similar linear mixed models, when the new method was applied to the longitudinal DXA study, BMD gradually increased over time. In contrast, the conventional method had higher variance in percent change/ 2 weeks. The range of non-outliers (i.e., all data between the T-bars above and below the box plot in **Fig. 6B**) was similar between the new and conventional methods, but the conventional method had more outliers for the distal femur and proximal tibia. Lumbar vertebrae had a much larger range of non-outliers for the conventional method than the new method **(Fig. 6B)**. Levene's test of equal variances was performed to determine whether there was a significant difference between the variances from each method and showed that the data obtained by the conventional method had significantly higher variances at all sites ($p < 0.05$) **(Table 4)**.

Accuracy of the New Method

Correlation coefficients between DXA BMC and micro-CT BMC were 0.846 for the distal femur, 0.879 for the proximal tibia, and 0.678 for lumbar vertebrae, significant at all sites with $p < 0.01$ **(Fig. 7A)**. Because DXA BMD and micro-CT BMD are in different units (g/cm^2 and g/cm^3, respectively) the results showed a similar trend, but lesser correlation than that of DXA versus micro-CT BMC ($r = 0.752$ for distal femur, $r = 0.764$ for proximal tibia, and $r = 0.465$ for lumbar vertebrae; $p < 0.01$ at all sites). The linear regression of DXA BMC against micro-CT BMC obtained by the new method for the distal femur, proximal tibia, and lumbar vertebrae resulted in SEEs of 0.00026, 0.00024, and 0.0006 g, respectively. The SEEs of all three sites were smaller than the SD of micro-CT BMC measurements (SD: 0.00047 g for distal femur, 0.00049 g for proximal tibia, and 0.00079 g for lumbar vertebrae).

3.1.3 Bone density plateau of BALB/c female mice

In order to confirm skeletal maturation of the female BALB/c mice, we performed a longitudinal DXA study to monitor the BMD change while the mice aged until 32-week old. The BMD of distal femur, proximal tibia and lumbar vertebrae gradually increased with age. The plateau of BMD was reached in femur and tibia around 26-28wks old, while in lumbar at around 30-32wks. According to literature[110-112], mice in general reach skeletal maturity around 28-32wks, though there is large variance between different sexes and strains. Considering our longitudinal BMD monitoring results along with data from literature, we decided to use 32-week old BALB/c female mice in our Flight Operations to ensure that no further skeletal growth occurred.

3.1.4 Discussion for 3.1.1-3.1.3

From multiple aspects, we confirmed that OVX is a suitable model for osteoporosis, in agreement with literature[113], and can mimic postmenopausal osteoporosis or general bone loss caused by disuse atrophy. From our study, we confirmed that with the OVX model: (1) BMD significantly decreased (around 10-15%, variable by sites); (2) uterus atrophy was observed (3) a small number of nucleated epithelial cells and few leukocytes were observed in virginal smear analysis for diestrus stage (data not shown here). These results furthered our confidence in employing OVX as a reliable animal model for the study of osteoporosis.

The dynamic measurement of BMD in live subjects is an important step in musculoskeletal tissue engineering research. DXA is currently the most widely used noninvasive technique to assess BMD and BMC in animal research due to its simple, quick, low-radiation, and cost effective features. DXA is incapable of trabecular bone analyses because a DXA scan yields a 2D projection image that represents the full thickness of the mouse, similar to an X-ray image. Thus, any DXA ROI containing trabecular bone will also contain the tissues that are above and below the trabecular bone within the ROI. To our knowledge, this is the first study designed to develop a protocol to obtain precise and accurate BMD measurements specific to trabecular bone-rich regions, via DXA and could provide great benefit to osteoporosis investigators.

The results of this methodology study show that adherence to the new method can improve the precision and accuracy of DXA BMD measurements; which will reduce the need for micro-CT and the number of animals used in longitudinal research.

This study was initially designed during preparation for the later Flight Operation that collaborated with CASIS-NASA. The method developed in this study was implemented in later studies of our systemic therapy for microgravity-induced osteoporosis. DXA was chosen to quantify the changes in BMD throughout the longitudinal medical therapy study on the ISS because it is fast, easy to perform, economical, and suitable for space use. In addition, for spaceflight, DXA is the only method of BMD analysis that can be carried out onboard the ISS and also the only radiographic equipment available in the same model at all locations involved in the research project (the animal vendor, ISS, KSC in Florida, and UCLA). To enhance the accuracy and reproducibility of DXA measurements in all experiments, we conducted this separate study to standardize the scanning and analysis methods (**Fig. 8** summarizes the workflow for the new standardized method). This part of the research was published in Tissue Engineering Part C, Method (2016;22(5):451-63) and was officially adopted by NASA to use in all the future space flight rodent missions.

Apart from standardizing the animal model and DXA scanning and analyses methods, another important part of preparation was to determine the appropriate age for mice in the spaceflight mission. In the literature, it is stated that for female C57BL/6J mice, there are two physiological BMD peaks. The first peak in BMD is reached at 17 weeks of age, followed by slight decline and fluctuations until around 30 weeks of age, at which point bones will reach the second BMD peak[114]. Also, Buie et al.[111] published a comprehensive study which includes lumbar vertebra and tibia of C57BL/6, BALB/c and C3H/HeN mice. Their study concludes that for all three strains, peak BMD is not reached until around 32 weeks of age and is consistently preceded by a slight increasing trend of BMD. Beamer et al.[110] confirmed this in a longitudinal study utilizing CT analyses on mouse femurs. Beamer's results showed that bone density does not stabilize until around 8 months of age, observed in four different mouse strains. Due to the information from the afore discussed literature, we monitored BMD changes until 32 weeks of age, however, observed peak BMD at around 28 weeks of age. Femur and tibia data are generally more consistent, with lumbar BMD having more fluctuation. With these results and literature in consideration, we decided to age the mice to 32 weeks of age before transportation to the ISS to ensure full skeletal maturity.

3.1.5 BP-NELL-PEG Activity Test and Biodistribution Study

Conjugation of inactivated-BP with NELL-PEG was one of the key technologies we performed to overcome the challenges in this project. The hydroxyapatite binding test was carried out to test the binding affinity of the conjugates to bone. As shown in **Fig. 9A**, the binding affinity of BP-NELL and BP-NELL-PEG were significantly higher than the unmodified NELL-1 and NELL-PEG groups. With conjugation to inactivated-BP, BP-NELL-PEG had binding affinity that was 3 times stronger than NELL-PEG. Thermal shifting tests **(Fig. 9B)** showed that compared to unmodified NELL-1, BP-NELL-PEG had significantly higher thermal stability (4.75 °C higher). For *in vitro* bioactivity testing **(Fig. 9 C-D)**, both Alkaline phosphatase (ALP) staining and Alizarin red (AR) staining corroborated that BP-NELL-PEG has comparable osteogenesis activity to unmodified NELL-1 and NELL-PEG, all of them significantly increasing osteogenic ability compared to control.

Additionally, the conjugated protein was labeled with VivoTag 680XL and injected systemically into mice. 48h post tail vein injection, the protein was visualized by an optical imaging system. A comparison of saline control, NELL-1, NELL-PEG and BP-NELL-PEG accumulation in each of the mouse organs 2 days after IV injection is presented in **Fig. 10**. PEGylation increased the circulation half-life of the protein and also increased the deposition in bone tissues such as femur, tibia, and vertebrae. BP conjugation further enhanced protein specificity to bone, resulting in significantly increased NELL-1 deposition in the bones, including femurs, tibias and the maxillary and mandibular bones for the first time in NELL-1 research (data not shown). This result suggests that this inactivated-BP conjugated therapy could be used for dental bone loss defects, such as in periodontal disease and TMD. Also, there was significantly less accumulation in the metabolic and excretory organs such as the liver, spleen, and lungs compared to earlier forms of NELL-1. For all types of NELL-1, there was no accumulation in critical organs (heart and brain). These results inspired confidence in systemic use and possible reduction of off-target side effects after administration.

3.1.6 Systemic Administration Route for NELL-1 Therapy

Due to technical limitations on the ISS, astronauts are unable to perform tail vein injections in space. In order to explore an easier, effective injection method, we investigated systemic treatment by IP or SC injections in OVX- induced osteoporotic mice for 8 weeks, administered every other week (4 injections in total). Trabecular bone analysis results are shown in **Fig. 11**. Both IP and SC injection groups reflected treatment effects, however, no significance between the SC group and OVX control was observed. The IP injected group showed significant treatment results in most of the parameters in both distal femur and proximal tibia. For distal femur, IP injected NELL-PEG increased the BMD by 21.3% and BV/TV by 16.6%; for proximal tibia, the BMD was increased by 10.6% and BV/TV by 18.7%. From these results, we can conclude that an IP injection route is more effective than SC injection and can promote bone growth similarly to previous IV injection studies (measured by micro-CT changes in trabecular bone, 15% BMD increase at distal femur and 12% at lumbar vertebrae).

3.1.7 Effective Treatment Dose of NELL-PEG Therapy

After selecting IP injection as the administration route, we further tested treatment doses that could generate consistent treatment effects. As shown in **Fig. 12**, the 5mg/kg NELL-PEG significantly increased BMD in lumbar vertebrae (15.8%) but not distal femur. Tb.Th at both lumbar vertebrae and distal femur were increased. However, 10mg/kg treatment had more consistent results, with BV/TV (17.6% at distal femur, 12.5% at lumbar vertebrae), BMD (16.8% at distal femur, 20.9% at lumbar vertebrae) and Tb.Th all significantly increased and with no site difference. From these results we conclude that although 5mg/kg NELL-PEG generates decent treatment results, 10mg/kg dosage has more stable, systemic improvements.

Additionally, to assess bone strength, we applied simulated biomechanical tests on micro-CT image sets of the trabecular bone using FEA by generating bone mesh models of cubic trabecular regions, selected from consistent femoral locations across all groups. **Fig. 12C-D** shows the results of simulated biomechanical tests between 10mg/kg IP NELL-PEG treated group and OVX control. Blue regions and lower Von Mises Stresses represent bone which is stronger and more resistant to fracture, observed in the NELL-PEG treated group. Yellow and red regions and higher Von Mises Stresses, as shown in the OVX control group, represent bone which is weaker **(Fig. 12D)**. The 10mg/kg IP injection group had markedly improved anti-compression ability versus control.

In addition, we looked into the treatment effects of systemic NELL-PEG therapy for dental alveolar bone. Excitingly, we found that NELL-PEG therapy increases the density, volume, and quality of alveolar bone as well. As shown in **Fig. 13**, the BMD and BV/TV of the ROI under mice maxillary first molar was significantly higher in NELL-PEG treated group and accompanied by greater Tb.Th. These signified stronger and more functional dental bone in all dimensions. This first peak into the dental alveolar bone effects of NELL-PEG systemic therapy was promising and encouraged further investigation, executed in our later experiments.

3.1.8 Treatment Effects Comparison Between NELL-PEG and BP-NELL-PEG

Results of BP-NELL-PEG experimentation, which employed IP injections of different treatments at every other week for 8 weeks, are shown in **Fig. 14**. For all three bone sites, 10mg/kg BP-NELL-PEG showed the most consistent and strongest treatment effect of all groups. Interestingly, with bone-specific targeting of BP, bone density and bone volume improvements exceeded Sham control levels at distal femur and proximal tibia sites. Although the 5mg/kg BP-NELL-PEG group showed treatment effects as well, they were slightly lower than the 10mg/kg treatment group. The 10mg/kg NELL-PEG group also showed increased bone density and volume compared to OVX control, but were not always significant. DXA results **(Fig. 14)** were consistent with trabecular bone micro-CT results, with 10mg/kg BP-NELL-PEG having the strongest treatment effects, increasing BMD by 8-10% in general. Again, although the 5mg/kg BP-NELL-PEG group had similar treatment effects, they were not as appreciable as in the 10mg/kg BP-NELL-PEG group. From these results, we conclude that with the help of BP, NELL-PEG can bind to bone with greater affinity and for longer durations and presents more osteogenesis even with reduced dosage.

The BMSCs colony assay results showed trends consistent with our *in vivo* data. As shown in **Fig. 15**, humeri-flushed BMSCs cultured for 14 days showed differential colony formation in each group. The results display a statistically significant increase in both BMSCs numbers and ALP expression in the 10mg/kg BP-NELL-PEG treated group compared to other groups, except for Sham, suggesting that after the BP conjugation BP-NELL-PEG further enhances the proliferation of BMSCs when administered systemically. The 5mg/kg BP-NELL-PEG and 10mg/kg NELL-PEG treatment groups increased BMSCs number as well, however not as effectively. This result further confirmed that BP modified NELL-PEG at 10mg/kg dose has the strongest osteogenic effects.

3.1.9 Validation of inactivation of bisphosphonate (BP)'s anti-osteoclastic effects.

In order to confirm that conjugated BP is inactivated, we performed 4 injections every other week in our OVX control group, Sham control group, 5.11mg/kg BP-BSA group (the dose of BP in this group matching the BP in BP-NELL-PEG group) and 10mg/kg BP-NELL-PEG group. A

BP-BSA group was employed as a carrier control since the conjugation method between BP and BSA was exactly the same as BP-NELL-PEG conjugation. At the end of the study, all mice were harvested and scanned with micro-CT to quantify trabecular bone quality and quantity. From micro-CT results **(Fig. 16)**, both distal femur and proximal tibia showed significant increases to BMD and BV/TV with 10mg/kg BP-NELL-PEG treatment. For lumbar vertebrae, some increases to BMD and BV/TV with BP-NELL-PEG treatment were observed but were not statistically significance. In DXA analysis, there were 8.7%, 10.5% and 12.3% BMD increases at distal femur, proximal tibia, and lumbar vertebra, respectively. For the BP-BSA group, BMD and BV/TV were maintained at baseline levels as OVX control and showed no difference (<3% in DXA) compared to the starting point. These results prove inactivated BP exhibits no therapeutic effects *in vivo*.

We further validated the inactivation of conjugated BP *in vitro*. Bone marrow cells were flushed from mouse femurs then cultured according to the previously mentioned OC induction protocol. There were four groups in total: control group, BP-BSA group (408.8ng/ml), BP-NELL PEG group (800ng/ml), NELL-PEG group (800ng/ml). Treatments were added to OC induction medium, after macrophage induction stages, every day for 6 days continuously. According to the results in **Fig. 17**, OC suppression effects of BP-NELL-PEG are comparable to NELL-PEG, with no significant differences between BP-BSA and blank control, indicating that the anti-OC effects of NELL-PEG was not altered by BP conjugation and that inactivated BP completely loses its anti-OC effects.

3.1.10 Discussion for 3.1.5-3.1.10

Before proceeding to Flight Operations, we optimized NELL-1 based therapy's administration route, dosage, and structural modification to make the treatment more effective. Partial results of our study of IP vs SC injections of NELL-PEG therapy has been published in

BioResearch Open Access (2016;5(1):159-70.)[115]. The rationale for and difference between IP and SC administration routes are as such: In the laboratory setting, IV, IP, and SC routes constitute the most frequently used drug delivery methods[116]. While IV administration allows rapid dispersal of the drug into the circulatory system, the method is quite challenging to master and entails noteworthy risks of inflammation, thrombophlebitis of the vein, and necrosis of the surrounding tissues. IP administration, however, is less invasive than IV administration and facilitates absorption due to the large surface area of the abdominal cavity and abundant blood supply at the injection site. Conversely, SC administration has the slowest rate of absorption. Compared with the IV route, the IP and SC routes are more favorable for drug delivery because they are not only less invasive but also allow for a greater volume of injection that serves as a slow-release and long-acting deposit of the drug[116, 117]. For long-term drug delivery formulations in humans, factors such as the drug safety profile, ease of administration, subject accessibility and mobility, target area and injection site, and cost of therapy should be taken into consideration. Nonetheless, in laboratory settings, the IP route has been more widely used due to its induction of greater drug effects in a shorter period[116-119]. In addition, IP injection was preferred over SC by NASA to reduce the risk of needle prick injury to astronauts.

In a biodistribution study (data not shown), we found that in comparison to the SC group, the IP group showed greater NELL-PEG signal intensities in the liver, fat, and ovary, suggesting that the protein was absorbed and metabolized via the IP route but not via the SC route. This observation may be attributable to the high molecular weight of NELL-PEG (863.1kDa), which hinders diffusion into the capillaries near the injection site and subsequent distribution by systemic circulation. For the *in vivo* study, the mice were injected every 14 days and treatment effects were examined at the end of 8-weeks. IP injection had greater treatment effects compared to SC, suggesting that an IP route facilitates slow absorption of the protein from the injection site and thus maintaining higher protein concentrations for longer periods.

For treatment dosage, we previously found 1.25mg/kg of NELL-PEG to be effective, however with IV administrated injection interval every 7 days maximal. Going from IV to IP and doubling the injection interval to every 14 days was a significant change, the extreme microgravity environment notwithstanding. In order to ensure that treatment effects of NELL-PEG were not lost with this change, we tested treatment with doses 4 times (5mg/kg) and 8 times (10mg/kg) of the initial basic dose of 1.25mg/kg. From the results in **3.1.8**, we conclude that 10mg/kg treatment works much better than 5mg/kg. However, due to the challenging injection protocol, even the high dose of 10mg/kg only achieved about the same level of bone volume increase as previous IV injections at 2 to 4 days. These results prompted us to consider how to further improve the treatment efficiency in ways other than increasing dose.

BP are among the most well-known drugs and are frequently used as bone targeting tools. They can be easily conjugated with protein drugs if there are proper molecular structures can be matched. The BP molecule used in this study is alendronate, one of the two most widely prescribed BP therapeutic (Alendronate (Fosamax) and Risedronate (Actonel)) medicines in the United States. Also, long-term safety and efficacy of alendronate (10 years results) for postmenopausal osteoporosis treatment has been demonstrated[120]. Alendronate shows stronger binding affinity compared to most other BPs, because of its unique structure[88, 121, 122]. In a study by Nancollas et al.[123], under conditions likely to simulate BP binding onto bone, there were significant differences in affinity constants among the BP for HA growth (pH 7.4) with a rank order of zoledronate > alendronate > ibandronate > risedronate > etidronate > clodronate. In addition, the rank order of urinary excretion 24 h after first dose, in clinical studies, was zoledronate (38%) < alendronate

(44%) < risedronate (65%) < clodronate (73%)[124]. This is consistent with results for binding affinity, which suggest that BP with higher binding affinities have lower 24 hrs urinary excretion. 3-D configuration and nitrogen orientation in nitrogen-containing BP (N-BP) may play an important role in mineral binding affinity as well. Alendronate is able to form N-H-O bonds at 132°, which favors H bonding[124].

Also, for molecular structure, Alendronate has an amine group (-NH2) which can be used for conjugation with NELL-PEG. Interestingly, the conjugation may decrease the antiprenylation effect of BPs in bone, reported by Dunford. et al.[104]. They found that even very small changes in nitrogen position relative to the BP motif leads to movement of the nitrogen group which disrupts hydrogen bond geometry significantly. This usually leads to a loss in initial potency and reduced ability to hold the enzyme–inhibitor complex in the isomerized state. The degree of reduced activity of BP depends on cleavage of the linkage between BP and NELL-PEG, which releases free BPs in the cell, and the enzymatic degradation of drug in the liver. Therefore, the BP activity of BP-PEG-NELL could be inactivated or significantly decreased.

From other peer-reviewed structure-activity relationships studies, we infer that the specific orientation of the nitrogen atom in active BP, such as alendronate, risedronate, zoledronate, et al., is responsible for pharmacological activity[104]. Thus, suboptimal nitrogen orientation and enzyme binding will significantly decrease pharmacological activity, effectively inactivating BP even under normally effective concentrations.

Because these reasons, Alendronate was used in this study, conjugated to PEG-NELL, to enhance the bone-seeking function in BP-NELL-PEG. Furthermore, recent reports on BP-modified proteins illustrate the feasibility of bone-specific delivery of biologically active protein drugs[125, 126] such as cytokines and growth factors. In our case, BP-NELL-PEG is the conjugation of BP with large pentamer protein (NELL-PEG) to achieve prolonged local exposure of bone to high concentrations of the targeting drug and thereby enhancing pharmacological efficacy and minimizing systemic side effects.

3.2 Flight Operation

3.2.1 Motor Function

Rota Rod tests were performed to evaluate the motor function of rodents immediately upon live return and after 4 weeks of recovery on the ground. To quantify motor function level, we evaluated the length of time and maximal rotational speed that mice could endure. The results shown in **Fig. 18** suggests that after 5 weeks of space travel, flight group was 20% weaker than the ground control when coming back from space despite of the NELL-1 treatment or not, indicating that microgravity can weaken the motor function of the mice significantly. The mice partially recovered (10%) after 4 weeks back on Earth in the PBS groups. This is in line with human studies which show that post-flight recovery period for astronauts is twice the period of spaceflight and can take up to 9 months to recover 50% of lost bone. Excitingly, we found that in NELL-1 treated groups, motor function recovery rate was significantly increased. Over 20% of recovery were observed in the length of time that mice could stay on the rod and maximum rod speed tolerated. Within the same housing conditions, NELL-1 treated groups showed two-fold more recovery as compared to PBS groups.

3.2.2 Systemic BP-NELL-PEG Therapy in Space

In order to longitudinally monitor BMD change, we performed DXA scans for all groups pre-flight, at the live return time point (half way of study), and at the terminal time point. DXA results showed significant treatment effects of BP-NELL-PEG therapy regardless of whether in space or on ground. BP-NELL-PEG treated groups showed significantly higher BMD% change compared to PBS groups and was clearly observed in both flight and ground animals. In addition, similar trends were observed at both live return (5wks in Space, or 0wk on Earth) and terminal time points (9wks in Space, or 4wks on Earth). These results show that strong and consistent BP-NELL-PEG treatment effects (up to 18% increase of BMD) can be achieved under different conditions and at different time points. Microgravity effects on bone loss were also observed in the DXA data. For the terminal groups, significant microgravity-induced bone loss was observed in proximal tibia by both 5 weeks and 9 weeks of spaceflight, which was improved successfully by treatment. For live-returned mice, microgravity effects were observed immediately upon return to Earth, but were gradually eliminated by the final time point due to reambulation and recovery. Treatment expedited bone gain. In lumbar vertebrae, similar microgravity-induced bone loss was noticed, but in lower magnitude than observed in proximal tibia. The details of the DXA data are presented in **Fig. 19**.

All groups were harvested at the same end time point at week 9 (in space, at KSC or at UCLA) with subsequent high resolution micro-CT scanning of bone samples. In cortical bone analysis for distal femur and proximal tibia **(Fig. 20B and 21B)**, more bone volume was observed in BP-NELL-PEG treated groups in both LAR and TERM groups. For trabecular bone analysis, the BP-NP treated groups have consistently higher BMD and BV/TV regardless of loading environment (on ground or in space) **(Fig 20C and 21C)**. In lumbar analysis, growth plate regions were selected and customized for each sample, the results are presented in **Fig 22**. Comparable to long bones, significantly higher BMD and BV/TV was observed in all BP-NELL-PEG treated groups compared to PBS controls.

At the time of harvest of live return mice, bone marrow was flushed from humeri and cultured. Pre-macrophage cells were isolated and induced into OC. As shown in **Fig. 23**, the BP-

NELL-PEG treated flight group had significantly higher OC numbers compared to its PBS control. The flight treatment group had significantly higher numbers of osteoclasts than the ground treatment group. The BMSCs were also flushed out and cultured for CFU-F assays for 14 days. As shown in **Fig. 24**, the colonies were stained with ALP and Giemsa sequentially to show the number of osteogenic colonies and total colonies. ALP staining shows significantly more osteogenic colonies for both BP-NELL-PEG treated groups, regardless of whether in space or on ground. There are no differences between flight BP-NELL-PEG treated groups and ground control BP-NELL-PEG treated groups, which suggests that treatment can recover BMSC osteogenesis ability to ground levels. For the Giemsa staining, significantly more colonies were present in the BP-NELL-PEG treated group compared to their PBS controls, regardless of whether on ground or post-microgravity. There were significantly fewer colonies in both of the flight groups compared to their ground controls, indicating that microgravity induced decreases in colony formation.

We performed dynamic histomorphometric analyses for all TERM groups to further evaluate bone formation rate **(Fig 25).** The BP-NELL-PEG treated flight group showed significantly wider space between labels, which translates to higher MAR and BFR/BS during quantification. The ground control group treated with BP-NELL-PEG showed slightly higher bone formation rate as well, compared to PBS groups.

Histology staining confirmed increased bone formation and trabeculation in the metaphyseal area of the distal femur in the BP-NELL-PEG treatment group **(Fig. 26)**. Consistently with these results, OCN immunostaining demonstrated increased OB numbers and both RANKL immunostaining and TRAP staining demonstrated increased OC numbers as well in the BP-NELL-PEG treated group compared to the PBS control groups **(Fig. 26)**.

Additionally, there were significant increases in bone marrow fat caused by microgravity exposure (flight PBS group) **(Fig. 27)**. We observed that in the femoral bone marrow area close to growth plate, drastically more lipid vacuoles were present in the flight PBS group. The flight and ground treatment groups have significantly fewer number of lipid vacuoles compared to their PBS controls.

3.2.3 Discussion for 3.2 and Future Directions

Our spaceflight mission was the first live-return of drug-treated rodents from the space environment. Through collaboration with the UCLA Behavior Testing Core Facility, we were able to conduct motor function tests on live-returned mice immediately upon return to Earth and after 4 weeks of recovery. Results show that motor function recovery doubled in NELL-1 treated groups as compared to PBS controls.

Abundant *Nell-1* was reported by other groups to be found in developing and adult neural systems[64, 127] [Note: Nell-1 (protein) and *Nell-1* (gene): in mice; NELL-1 (protein) and *NELL-1* (gene): in human]. Transcriptome analyses have implicated *Nell-1/NELL-1* in several neurodegenerative and neuropsychiatric disorders such as ASD and Alzheimer's disease[64, 128-130]. This has linked NELL-1 to cognitive function and neurologic development. Recent behavioral studies from our lab (unpublished data) have shown that *Nell-1* $^{+/6R}$ mice developed attention deficient hyperactivity disorder (ADHD)-like symptoms. For example, in marble bury assays, *Nell-1* $^{+/6R}$ mice buried almost all 12 marbles, while *Nell-1* $^{+/+}$ mice did not bury any in the same amount of time.

The large molecular weight of NELL-1 (90kDa before N-glycosylation and oligomerization) prevents it from penetrating the blood-brain barrier. Therefore, we hypothesized that NELL-1's cognitive functions are realized through either paracrine or endocrine systems. A possible candidate molecule which might work with NELL-1 on the cognitive function is osteocalcin (OCN). OCN is an osteoblast- and osteocyte-derived factor with endocrine actions[131]. OCN secreted by OB was found to regulate systemic glucose and energy metabolism, reproduction and cognition[131]. OCN-null mice displayed severe behavioral phenotypes such as deficit in spatial learning and memory with decreased synthesis of all monoamine neurotransmitters, while intracerebroventricular infusion of OCN corrected the neurotransmitter deficiency and defect in cognition[131]. Also, OCN favors hippocampal development by preventing neuronal apoptosis[131-133]. Our lab previously found higher OCN levels in SHAM or OVX+ systemic rhNELL-1 treated mice compared to non-treated OVX or SHAM control[53].

Both literature and our previous studies link NELL-1 and OCN to possibly explain the faster motor function recovery by NELL-1 treatment observed in our study. Further investigations will be needed to explore the roles and mechanisms of NELL-1 in cognitive function from multiple aspects.

From the study, we observed significant osteogenic effects of BP-NELL-PEG systemic therapy at both the tissue and cellular level. Surprisingly, we found that BP-NELL-PEG promoted both OB and OC activities. From our previously reported data, Nell-1 haploinsufficient mice (Nell-$1^{+/6R}$) exhibited impaired OB and excessive OC activity and systemic NELL-1 treatment showed both pro-OB and anti-OC effects[53]. Our current results lead us to assess the reasoning behind the discordant observations. From literature, we hypothesize that close coupling of OB and OC activity along with the increased bone-specificity and direct effect of NELL-1 on bone is involved. It has been proposed by Martin et al.[134] that activated OC are necessary for the control of bone formation response by OB in bone remodeling. There are multiple different mechanisms proposed for the coupling effects, such as matrix-derived signals[135], secreted contributors (IL-60/gp130 and cardiotrophin-1)[134, 136, 137], membrane bound contributors (RANK drives reverse signaling through

RANKL in the OB lineage, perhaps in co-operation with other paracrine factors, and thus providing another possible coupling pathway)[138], signals to and from other marrow components (hemotopoietic stem cells)[139, 140], etc.

Our hypothetical model for BP-NELL-PEG's mechanism of action incorporates BP's strong bone affinity and NELL-PEG's osteogenic stimulation. First, a reservoir of BP-NELL-PEG is formed on remodeling bone surface via BP's high bone-affinity as a pyrophosphate analog—binding to HA by electrostatic interaction with BP's phosphonate groups. Then, as OC resorb the bone, BP-NELL-PEG is released and binds to OB receptors, promoting bone formation. Some molecules are thought to be ingested by OC while others are degraded by lysosomes and eventually released as free particles in the extracellular matrix. NELL-1 is deemed to have an advantage over other protein drugs (e.g. BMP2, 26kDa) because its molecular mass (400 kDa) allows it to withstand several surface modifications without notably affecting bioactivity[109]. Also, even with PEGylation and inactive-BP conjugation, the protein (in nano scale) is significantly smaller than the diameter of capillaries (through which red cells of 6-8 micrometer diameter travel) and allows systemic administration. In our biodistribution study **(Fig. 10)**, we show that BP makes NELL-PEG more bone-specific, which could lead NELL-1 to exert a direct therapeutic effect on both OB and OC, enhancing their coupling effect. This could be verified in future OB and OC co-culture experiments. Separated by porous membranes permeable to soluble molecules, we could observe NELL-1 treatment induced changes between OB and OC signaling interactions.

Another possible reason for increased OC activity is the effect of microgravity. Microgravity is known to robustly increase OC bone resorption pit formation[141] and upregulate osteoclastogenesis by increasing OB RANKL/OPG ratios[142]. However, simulated microgravity (e.g. via hindlimb suspension rodent model and *in vitro* rotating wall vessel) may not have the same effects on OC. The hindlimb unloading (HLU) model is a well-known *in vivo* model for simulated microgravity, but there have been conflicting reports regarding the effects of HLU on bone resorption, with some reporting that HLU increases bone resorption[143] while others suggesting that bone resorption remains unaltered[144, 145]. Stressful situations due to tail wounds can interfere with experimentation. For the *in vitro* simulation system, the high-gradient magnetic fields directly affect pre-osteoclasts survival and differentiation[146] and fluid shear stress may introduce artifacts as well[147]. Simulated microgravity cannot mimic real microgravity with complete fidelity. *In vitro* exposure to microgravity causes modifications in the morphology, cell viability, cytoskeleton, gene expression, and matrix proteins of bone cells[147]. Further investigation of microgravity + BP-NELL-PEG's effect on OC would require another spaceflight study. In the meantime, for the use of the therapy on the ground, i.e. for immobilized osteoporotic patients, we could utilize a hindlimb suspension rodent model. Immobilization (mechanical unloading) is a common clinical scenario in osteoporotic fracture patients and not only impedes fracture healing, but also aggravates osteoporotic conditions and increases risk of more fractures. As such, BP-NELL-PEG's effect on preventing and treating osteoporosis either induced or complicated by mechanical unloading, as we have tested via this spaceflight mission, is highly clinically relevant.

Another exciting discovery of this study were the changes in bone marrow adipocytes with microgravity and treatment. As presented in **Fig. 27**, there was significant difference in marrow fat volume between treatment and non-treatment groups and between flight and ground control groups. This drastic and consistent difference leads us to ponder the cause of fat composition differences and which types of fat are mainly affected. From this study, we conclude that NELL-1 can reverse the severe bone marrow adipogenesis caused by microgravity.

Immobility and spaceflight alike induce fat cell formation in the bone marrow cavity, which is deemed to impair MSC activity and HSC niches in bone. Literature reports a close partnership between the two distinct somatic stem-cell types and a unique niche in the bone marrow made of the heterotypic stem-cell pairs[148-151]. Due to the interplay of MSC and HSC, increased bone marrow adipogenesis not only defers MSCs from osteogenic differentiation, but also inhibits HSC differentiation into blood cells, platelets, and immune cells. Adipocytes not only compete with OB for limited pool of BMSC, thereby influencing the structure and mechanical strength of bone, but also release adipokines to negatively affect bone health[152-154]. They also replace hematopoietic elements of the bone marrow and are associated with hematological problems leading to anemia, propensity to infection, inflammation and allergy, as well as impaired wound healing[155, 156], which collectively contribute to delayed or compromised fracture healing. In a 6-month bedrest study, patients showed increased marrow fat and disrupted hematological values (suspected to have resulted from fat replacement of hematopoietic elements in the marrow) that did not return to normal after 1 year of resuming normal daily activity[156]. NASA's Twin Study on Scott and Mark Kelly astronaut twin brothers also released preliminary finding showing that "93% of Scott's gene expression returned to normal after landing but the remaining 7% point to possible longer term changes in genes related to his immune system, DNA repair, bone formation networks, hypoxia, and hypercapnia"[157]. Recognizing the clinical importance of regulating marrow adipogenesis for health, NASA has initiated "The Marrow Study" in late 2018 to investigate the extent of spaceflight effects and recovery in bone marrow and blood cells. As such, a therapy that can simultaneously promote bone healing and inhibit pathologic marrow adipogenesis would be phenomenal in protecting both bone and general health. NELL-1 was known to suppress adipogenesis, previously reported[60], but the mechanism and the effects on hematopoietic stem cells are not clear. Combined with our recent spaceflight study results, there is need to further investigate how NELL-1 affects bone marrow hematopoietic stem cells.

DXA and Micro-CT analyses showed bone loss from 2 months of spaceflight was less than initially expected, based on literature and previous flight experiments. RR-1 (C57BL/6, 32 weeks old) showed around 15% bone loss at proximal tibia (BMD measurement by Micro-CT) after 21 days in space. RR-2 (C57BL/6, 12 weeks old) showed up to 20% bone loss at distal femur, proximal tibia and lumbar vertebrae (BMD measurement by DXA) after 54 days in space. RR-3 which used 12 weeks old BALB/c mice showed 7% decrement in BMD by DXA and 11% in BV/TV by Micro-CT at distal femur [findings provided by ISS Mission Scientist Dr. Yasaman Shirazi]. We propose two possible reasons for this: (1) An animal habitat component known as an "Enrichment Hut" was developed by the NASA Ames Research Center to provide animals with the ability to rest and huddle during long duration space travel. The enrichment hut is made of stainless steel mesh with an interior volume of 473ml (2.33" high, 5.5" wide and 4.75" deep). Our RR-5 mission was the first habitat configuration to use this enrichment hut and video monitoring analysis showed that mice did use the hut on orbit for significant amounts of time. According to the on-orbit video analysis, it was common for multiple (up to 5-6) mice to squeeze into the small hut space, taking up to 24% of the total volume or more. This crowding is equivalent to having five people in a closet that is 6.5ft high and 3x3ft wide. Studies have shown that huddling events are abundant in mice social behavior, more frequent during the light cycle than during the dark cycle, and can account for 55% of video frames during monitoring[158]. Enrichment huts are just like igloo houses in regular laboratory mice cage setting, which offers the mice a small and relatively enclosed space with meshed wall, thus any distances between the mice or between the mice and a surface would be small and could support pushing off and loading of the limbs.

Considering the tendency of mice to huddle and push in small spaces, having 5-6 mice in the enrichment hut could incur an “exercising effect”. This may have provided the mice with significant opportunity for the musculoskeletal loading with pushing, jostling and climbing, and may have decreased the amount of bone loss compared to previous RR missions. Additionally, the enrichment hut is designed for better animal welfare, possibly reducing the stress of the mice and allowing them to sleep better with better thermoregulation. This may have further prevented bone loss as well. (2) Another possible cause for the observed decrease in bone loss are the effects of strain and age used. Muscle atrophy was not observed in RR-6 (C57BL/6, 30-40 weeks old at launch) which used the same enrichment hut configuration (bone not yet analyzed). There may possibly be a strain effect, with bone loss patterns differing from previously used C57BL/6 strains. In general, the magnitude of bone loss seems to be less in BALB/c mice compared to C57BL/6 mice in RR spaceflight studies. However, literature show BALB/c mice to be a good model for osteoporotic therapy testing because it responds well to OVX and subsequent therapies compared to other strains[159]. In our preflight preparations as well, we validated the osteoporosis model in 4 months old BALB/c mice by inducing osteoporosis via OVX and monitoring BMD for 3 months. We showed significant bone loss by OVX in 4-5 weeks, and therefore selected the strain and age for Flight operations. While there is a chance that strain / age effects could have reduced the total bone loss by microgravity that was not foreseen in OVX model, this is thought to be a less likely cause.

For the micro-CT analysis, we can further refine and detail our data by looking into different bone layers. As observed in our samples, most treatment effects were localized near the growth plate. We can further differentiate bone layers in our analyses to endosteal and periostel surfaces to look into the differences in outer and inner bone formation affected by microgravity and NELL-1 treatment.

With space travel to Mars on the horizon, microgravity exposure on the order of 2-3 years is forthcoming. The muscular skeletal system, bone marrow hematologic function and immunity to fight against infections are key considerations for research. Potentially, NELL-1 based therapies could one day be used to help astronauts maintain better bone quality during space travel and upon return to Earth.

4 FIGURES AND TABLES

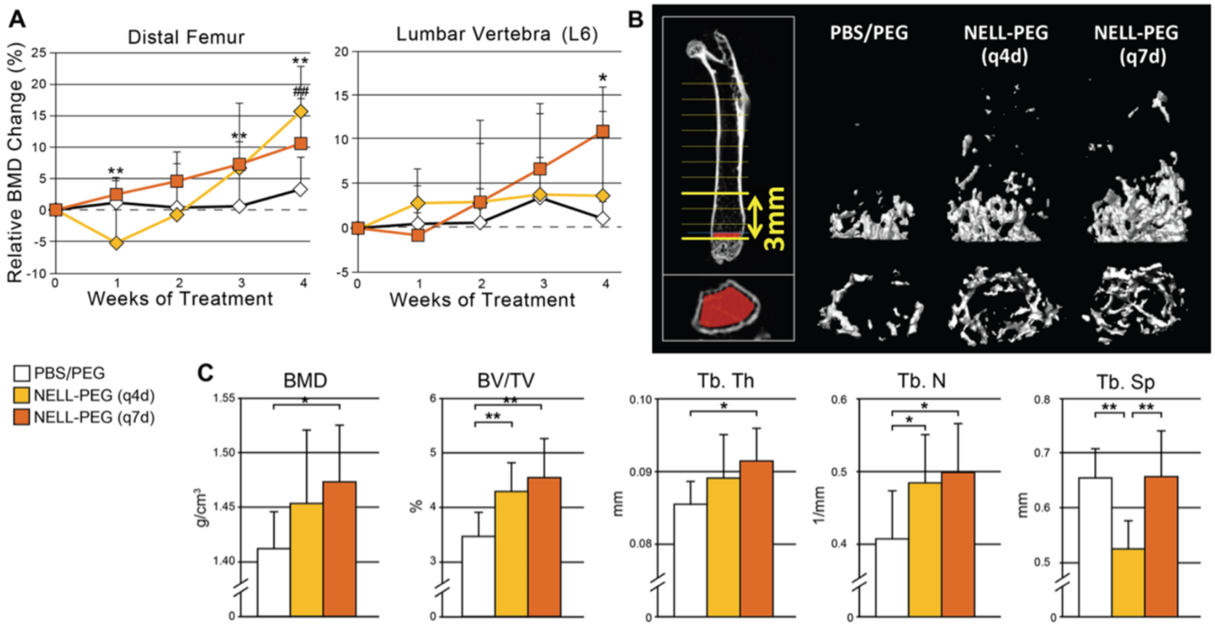

Figure 1. Systemic NELL-PEG therapy induces bone formation in mice (Figure excerpted from Kwak & Zhang, 2015, Biomaterials)[70]. NELL-PEG was IV injected (1.25 mg/kg, at q4d and q7d) for 4 weeks (n=6/group). (A) Weekly DXA analysis for femoral BMD, (B) high-resolution micro-CT 3D reconstruction, and (C) micro-CT quantification of the distal femur trabecular bone BMD, BV/TV, and Tb.Th, Tb.N, Tb.Sp after 4 weeks of treatment. The ROI for femoral trabecular bone analysis was defined as 3mm extending up from growth plate (a clearance of 0.1mm from the growth plate was maintained). Both q4d and q7d NELL-PEG groups presented statistically significant increase of bone quantity and quality compared to control, but with no substantial difference between each other. *p<0.05, **p<0.01. NELL-PEG, PEGylated NELL-1; BMD, bone mineral density; BV/TV, bone volume/tissue volume; Tb.Th, trabecular thickness; Tb.Sp, trabecular separation; ROI, region of interest.

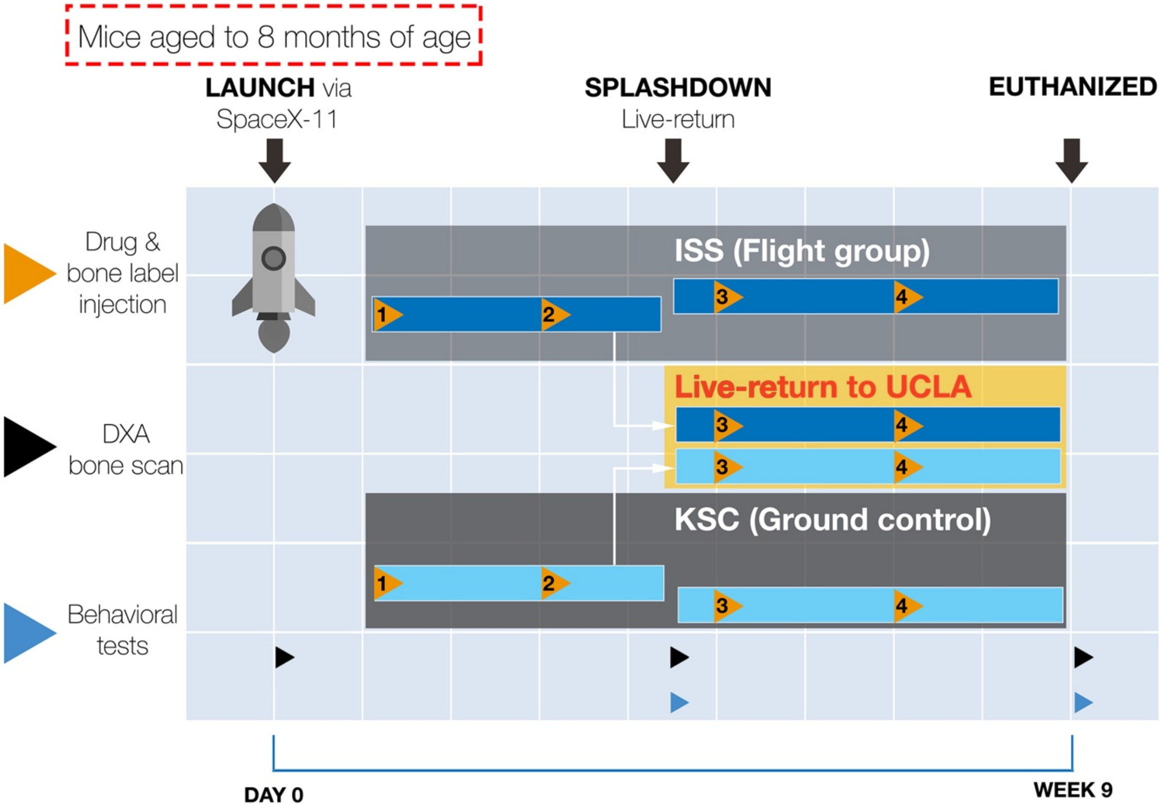

Figure 2. Timeline of flight operation (Rodent Research-5 mission). Mice were aged to 8 months at time of launch to ensure skeletal maturity. Flight groups were housed onboard the ISS (International Space Station). Matching Ground control groups were housed at the Kennedy Space Center (KSC) in Florida. Starting at approximately 1 week in orbit and every 2 weeks thereafter, mice received either BP-NELL-PEG or PBS injections. Fluorescent bone labels were injected simultaneously at week 3, 5, and 7 post-launch. Half way through the mission (after 4 weeks of treatment), half of the Flight group mice (n=20) were live-returned to Earth and transported to the animal care facility at UCLA to continue therapy for an additional 4 weeks. Half of Ground control mice (n=20) in KSC were also transferred back to UCLA for the same continued treatment. DXA scans and behavioral tests were performed before launch, after live return, and at the terminal time point. After 9 weeks of experimentation, all mice were euthanized. Carcasses from the remaining groups on the ISS and at KSC were frozen and later returned to UCLA for multi-team dissection and analyses. DXA, dual-energy x-ray absorptiometry.

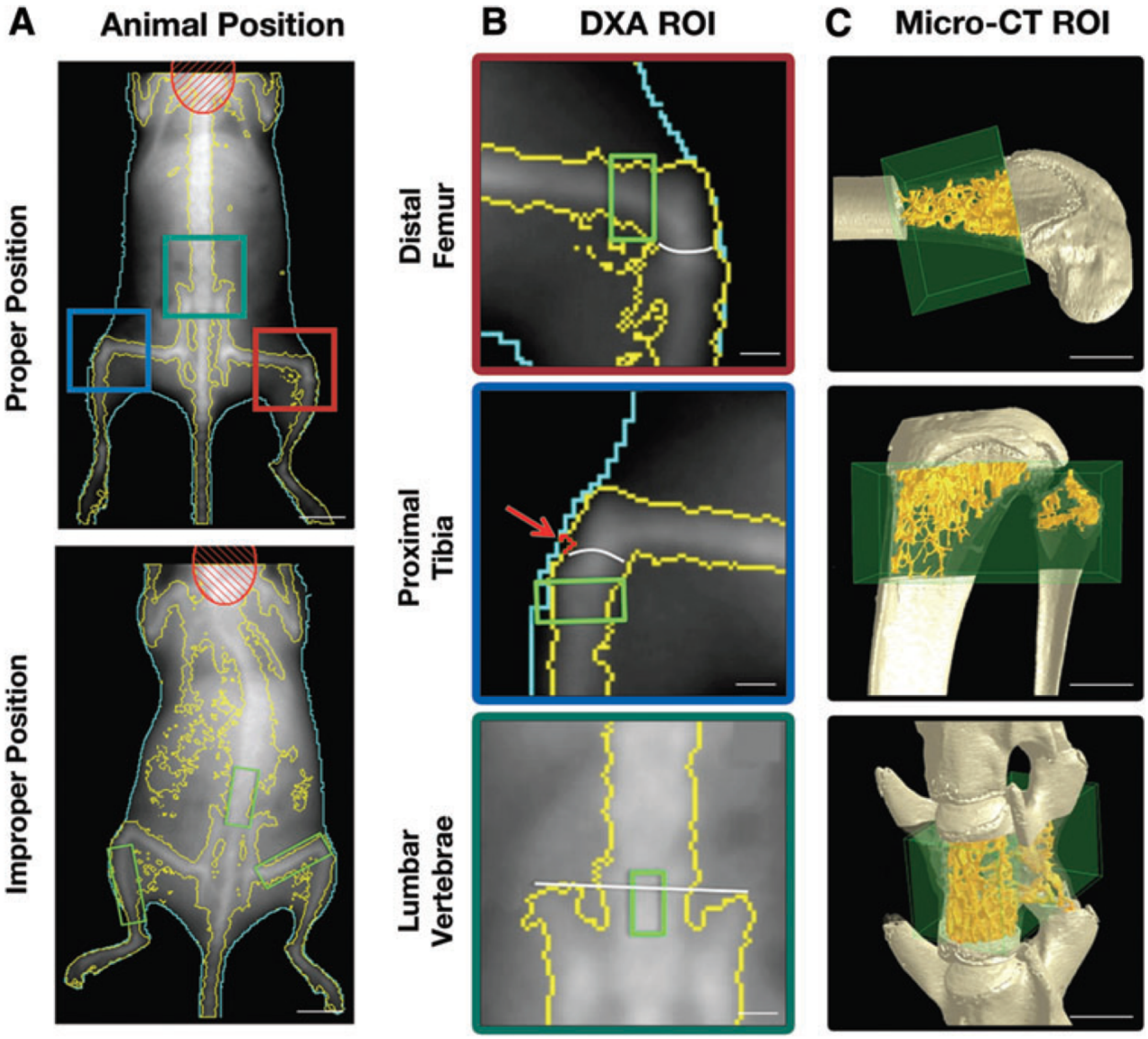

Figure 3. Mouse positioning and ROI locations in DXA and micro-CT. Proper mouse positioning is necessary for optimal DXA images. (A) The knee joint should be set to 90 degrees to pull down the patella and make the knee joint line obvious. The spine should be as straight as possible. Improper mouse positioning makes ROI placement difficult. The conventional method ROI (A: improper position) consisted of the whole bone. Knowing the location of trabecular bone-rich regions of interest and the location of the structures to exclude from analysis (e.g., epiphyseal plate and patella) allowed small ROIs specific to trabecular bone-rich regions to be properly positioned, consistently. The ideal ROI location for distal femur, proximal tibia, and lumbar vertebrae L6 are shown. (B) DXA ROIs. For the practical anatomical landmark, the indentation of the bone line (arrow) can be used to determine the end of the proximal tibia. To make proper comparisons between DXA and micro-CT, the same ROI was chosen in micro-CT as in DXA for the distal femur, proximal tibia, and lumbar vertebrae as shown in (C). Scale bar in A= 1 cm; B= 2 mm; C= 1 mm. ROI, region of interest; DXA, dual-energy x-ray absorptiometry.

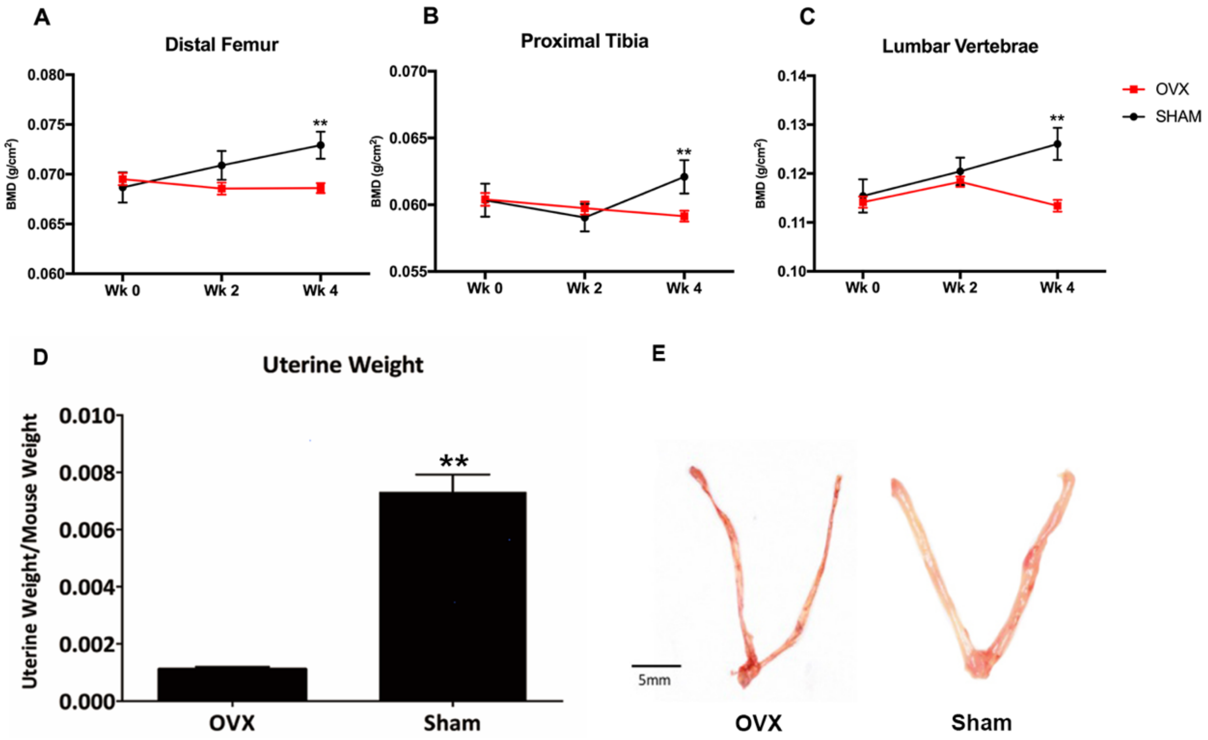

Figure 4. Successful establishment of the OVX induced osteoporosis model. 12-week-old female BALB/c mice underwent OVX surgery. The distal femur, proximal tibia, and lumber vertebra were scanned with DXA before and 4-weeks after surgery. (A-C) DXA results showed significant decrease of BMD at all three bone sites (8.12% at distal femur, 7.76% at proximal tibia and 12.61% at lumbar vertebra). (D) At the conclusion of the experiment, uteri of OVX and Sham groups were dissected and weighed. As shown in the bar graph, OVX mice had significantly atrophied uteri compared to the Sham group. (E) Representative images of an OVX and Sham mouse uterus. Scale bar = 5mm. * p<0.05, ** p<0.01. BMD, bone mineral density; DXA, dual-energy x-ray absorptiometry.

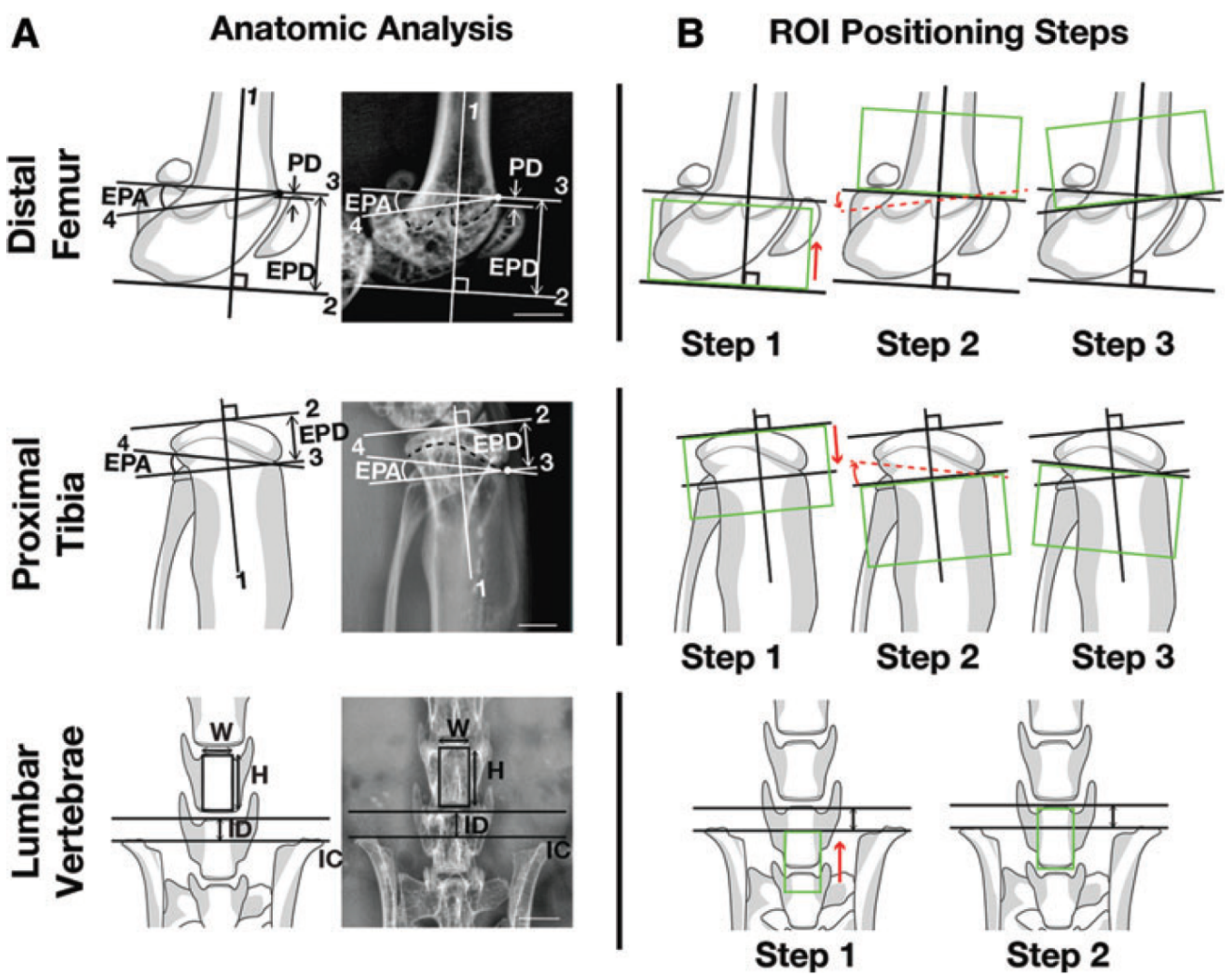

Figure 5. Key anatomic landmarks and proper DXA ROI placement steps. Anatomic analysis via high-resolution X-ray imaging. (A) For the distal femur and proximal tibia， the EPD and EPA were defined as the distance between ‘‘Line 2’’ and ‘‘Line 3’’ and the angle between ‘‘Line 3’’ and ‘‘Line 4’’ respectively. To ascertain the patella's location the knee joint was set to a 90 angle and the PD measured from the patella proximal tip to ‘‘Line 3.’’ To predict the location of lumbar vertebrae L5 and L6, the distance from the IC to the intervertebral space of L5/L6 was measured (ID). To fit the ROI in the vertebral body we measured the height (H) and width (W) of L5 and L6. The height was measured between the end plates and the width was measured at the cranial margin of each vertebral body. Following the anatomic analysis, ROIs were placed on each trabecular bone-rich region. (B) For the distal femur and proximal tibia each ROI was placed at the articular edge of the bone and aligned perpendicular to the longitudinal axis of the bone (Step 1). Then, the ROI was moved proximally (femur) or distally (tibia) as depicted in Step 2. The final step involved rotating the ROI (Step 3) based on the angles measured during the anatomic analysis. Proper lumbar ROI positioning required initial ROI placement parallel to IC at the middle of the lumbar vertebrae (Step 1). The ROI was then moved cranially to meet the cranial boarder of L6 (Step 2). Arrows in B show the direction of movement or rotation. Line 1: longitudinal axis of femur or tibia, Line 2: perpendicular line to ‘‘Line 1’’ that starts from the end of each long bone, Line 3: parallel line to ‘‘Line 2’’ that starts from the most proximal point of epiphyseal plate in femur and the most distal point of epiphyseal plate in tibia, Line 4: the line that connects the anterior and posterior margin of epiphyseal plate. DXA, dual energy x-ray absorptiometry; EPA, epiphyseal plate angle; EPD, epiphyseal plate distance; IC, intercristal line; ID, intercristal distance; PD, patella distance; ROI, region of interest. Scale bar = 2 mm.

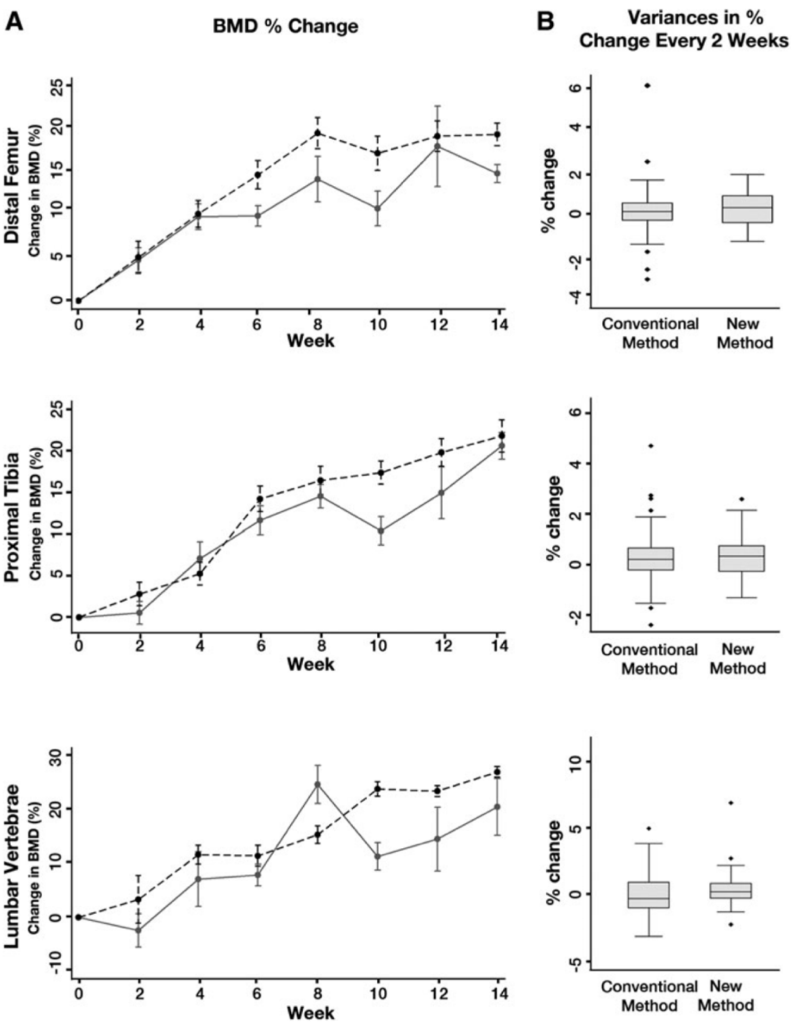

Figure 6. Longitudinal change of DXA BMD for 14 weeks at distal femur, proximal tibia, and lumbar vertebrae. To evaluate the precision of the new method, DXA BMD was analyzed longitudinally for 14 weeks. The longitudinal analysis of DXA BMD via the conventional method had higher variance compared to the new method for all sites (i.e., distal femur, proximal tibia, and lumbar vertebrae), as shown in (A). The solid line fluctuates significantly more than the dashed line, which reflects the greater BMD percent-change/2 weeks, as acquired by conventional method versus the new method. Box plots of percent-change/2 weeks show significant variance at all sites. (B) For distal femur and proximal tibia, the range of non-outliers (distances between T-bars above and below the box plot) for BMD percent change per 2-week interval was similar between the conventional and new method, with more outliers in the conventional method. There were no femur BMD measurement outliers for measurements obtained via the new method, but for the conventional method, 3.97% of the measurements were outliers. Tibial BMD outlier percentage was 0.74% by the new method, and 4.29% by the conventional method. Lumbar vertebral BMD outlier percentage was 2.21% for the new method and 0.71% for the conventional method, however the conventional method had a much wider range of non-outlier measurements compared to the new method. Levene's test of equal variances was performed to compare the variance from each method ($p < 0.05$ significance). Solid line: conventional method; dashed line: new method. DXA, dual-energy x-ray absorptiometry; BMD, bone mineral density.

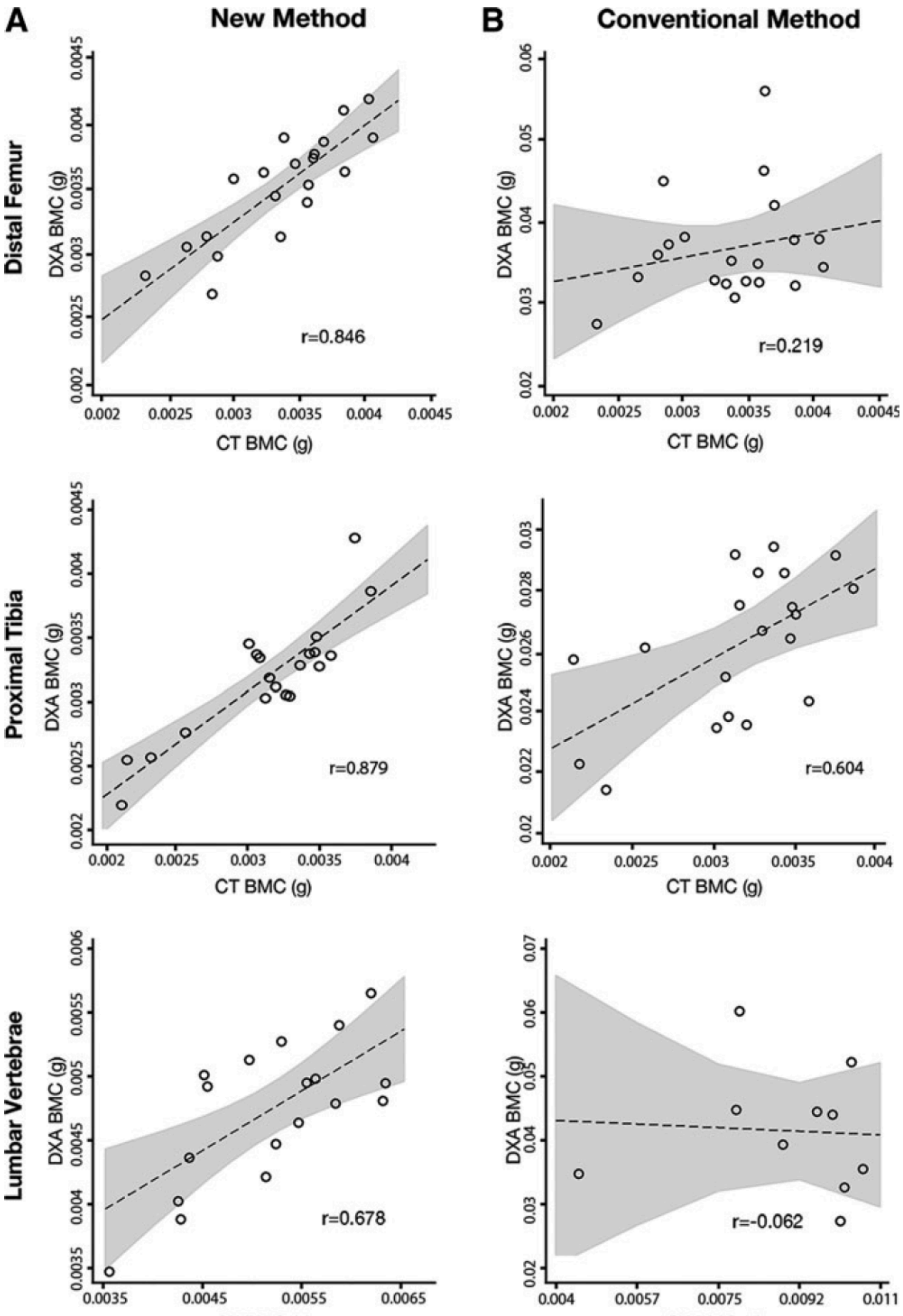

Figure 7. Correlation between DXA BMC and micro-CT BMC. Correlation analysis of the new method shows that the BMC of DXA significantly correlates with the BMC of micro-CT at all sites: distal femur, proximal tibia, and lumbar vertebrae (A) ($p < 0.01$). The correlation coefficient of the new method was greatest for proximal tibia (0.879), followed by distal femur (0.846), then lumbar vertebrae (L5, L6) with 0.678. However, the conventional method for DXA BMC does not significantly correlate with micro-CT BMC ($p > 0.05$ in all sites). (B) Pearson's correlation coefficients were used ($p < 0.05$ significance; r = correlation coefficient). DXA, dual-energy x-ray absorptiometry; BMC, bone mineral content.

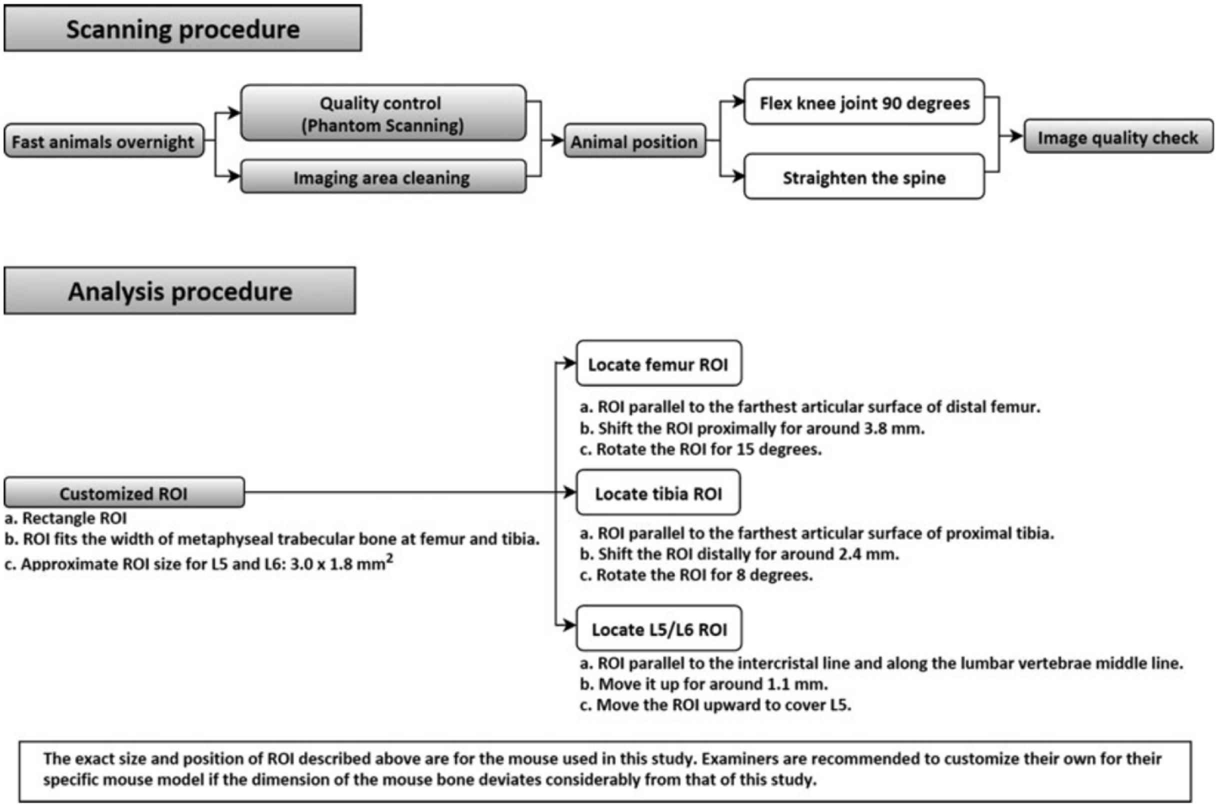

Figure 8. Flowchart of new DXA method. A brief guideline flow chart of the steps for the new DXA method of scanning and analysis. DXA, dual-energy x-ray absorptiometry.

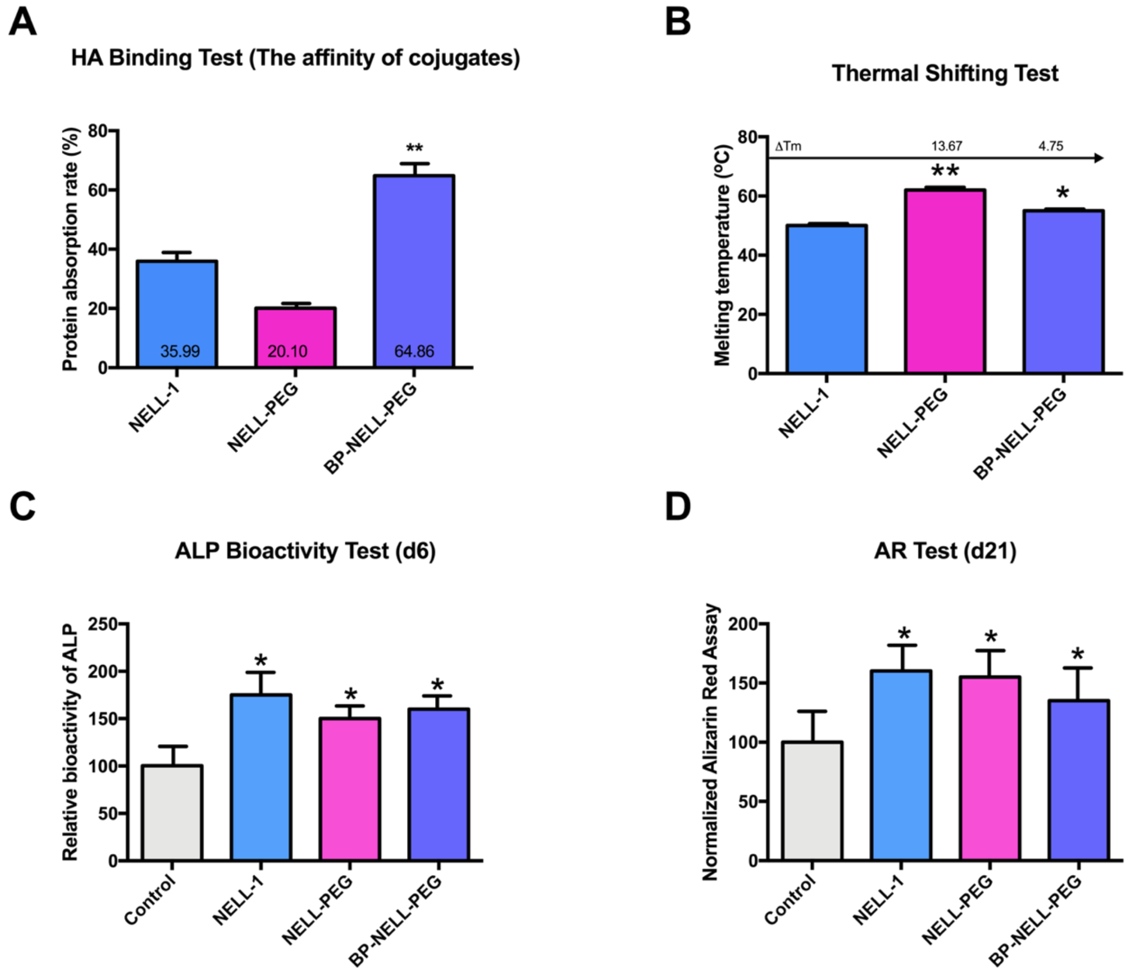

F**igure 9. BP-NELL-PEG binding affinity, thermal stability and bioactivity tests.** (A) The hydroxyapatite binding tests showed that after BP conjugation, binding ratio of BP-NELL-PEG increased up to 3 times compared to NELL-PEG. Meanwhile, (B) the thermal stability of BP-NELL-PEG was significantly higher compared to unmodified NELL-1. (C-D) Bioactivity tests showed activity levels between NELL-1, NELL-PEG and BP-NELL-PEG were comparable and were all significantly higher than control. *p<0.05, **p<0.01. HA, hydroxyapatite; ALP, alkaline phosphatase; AR, alizarin red.

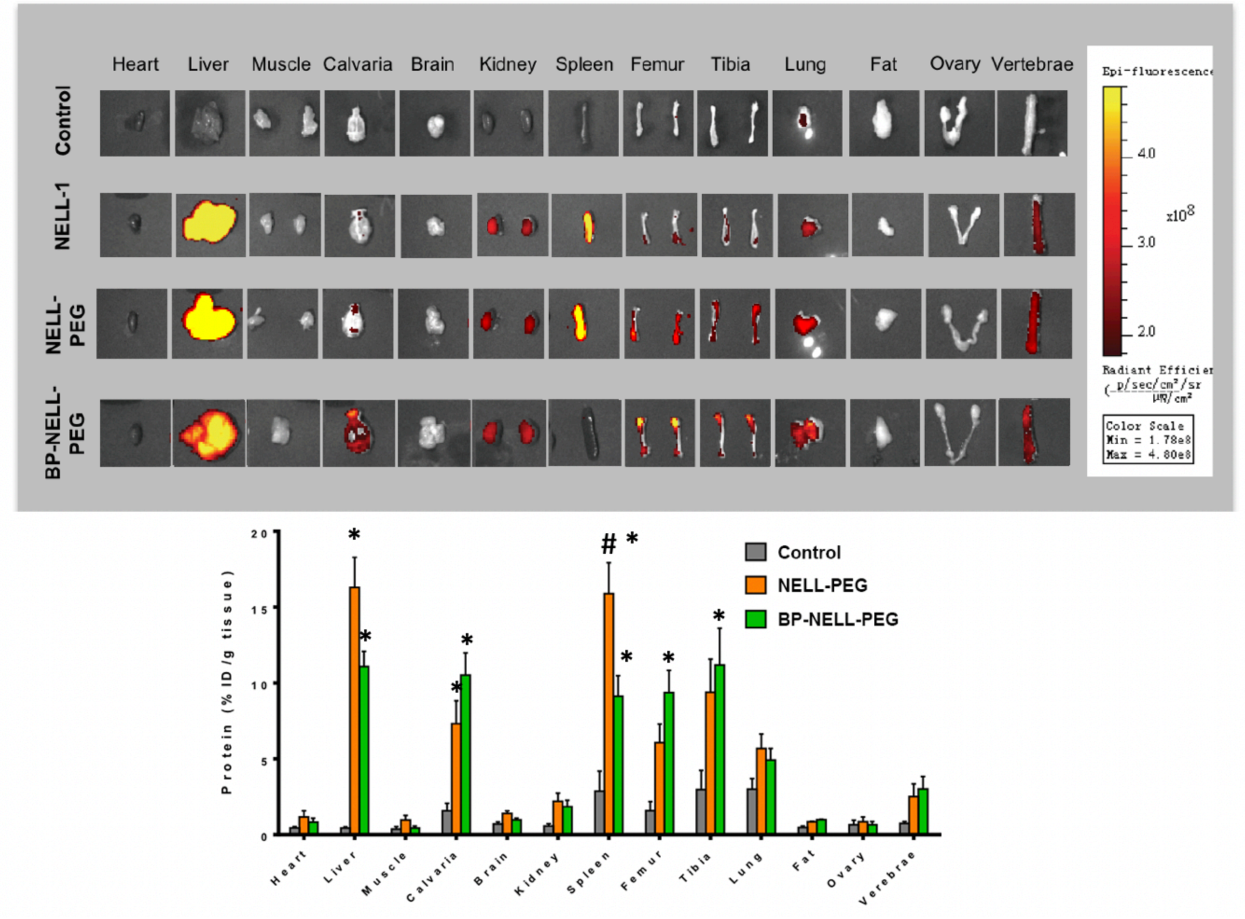

Figure 10. Biodistribution of NELL-1, NELL-PEG and BP-NELL-PEG. A biodistribution study was performed to compare the distribution of saline control (1st row), unmodified NELL-1 (2nd row), NELL-PEG (3rd row), and BP-NELL-PEG (4th row) labeled with VivoTag680XL. Organs were imaged ex vivo at 48h post-IV injection, using IVIS Lumina II optical imaging system. Compared with unmodified NELL-1 and NELL-PEG groups, BP-NELL-PEG showed a higher protein retention on the targeted bone tissues of femur, tibia, vertebrae, and the head, with reduced deposition in vital organs such as brain, lung, kidney, and spleen. The quantification of the protein retention amount in different organs is presented in the bar graphs at the bottom. NELL-PEG or BP-NELL-PEG vs control, *p<0.05, **p<0.01; NELL-PEG vs BP-NELL-PEG, #p<0.05.

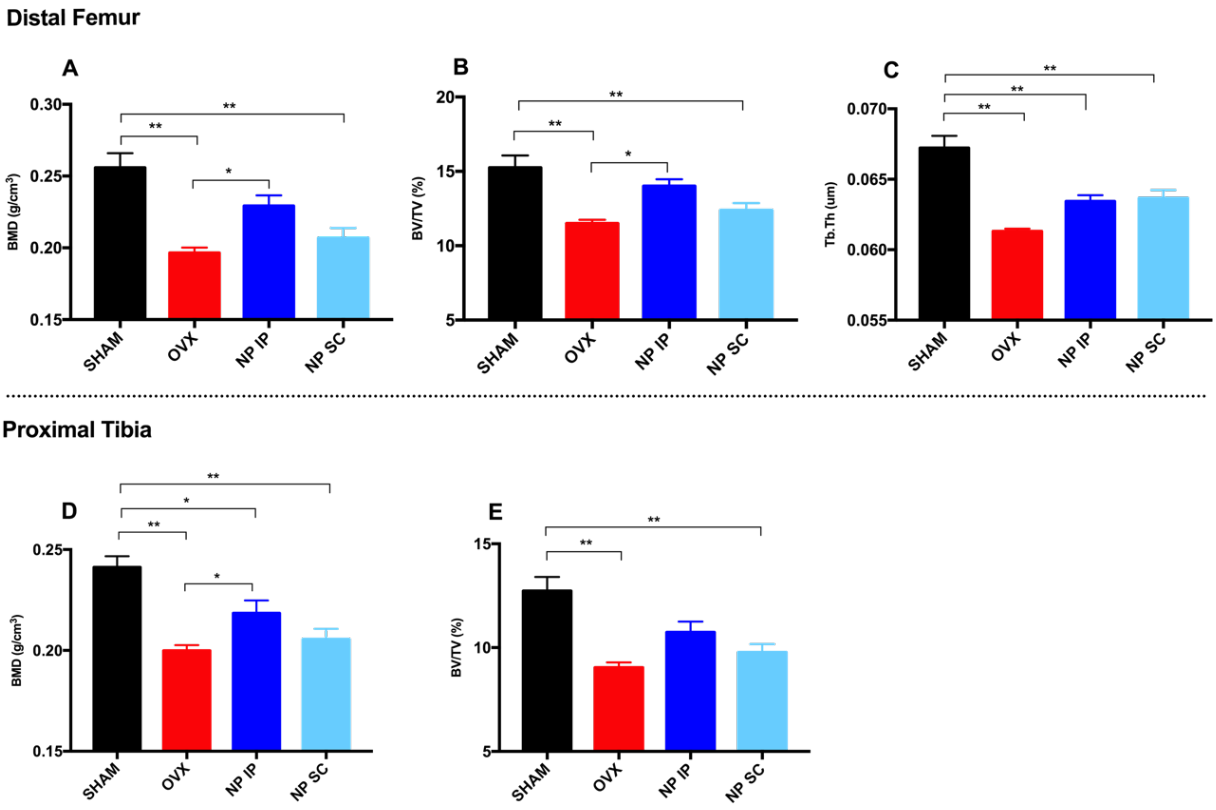

Figure 11. Micro-CT trabecular bone analysis of IP vs SC injection groups for NELL-PEG systemic treatment. OVX or Sham surgeries were performed on 12-week-old female BALB/c mic. 4 weeks later, mice were treated with PBS or NELL-PEG therapy (IP or SC injected). As shown in (A), trabecular bone BMD of distal femur increased by 21.3% compared to OVX. There is no significant difference between OVX and SC treated group. (B) The BV/TV of distal femur increased by 16.6% with IP injection, but did not significantly increase with SC injection. (C) Some increase was observed for Tb.Th with both IP and SC injections, although not significant. (D-E) For proximal tibia, BMD increased by 10.6% and BV/TV by 18.7% with IP injection. SC injection had comparable treatment effects but were not as strong as with IP injection. The region of interest for femoral and tibial trabecular bone analysis was defined as 3mm extending from the growth plate (a clearance of 0.1mm from the growth plate was maintained). * $p<0.05$, ** $p< 0.01$. BMD, bone mineral density; BV/TV, bone volume/tissue volume; Tb.Th, trabecular thickness; NP, NELL-PEG; IP, intraperitoneal; SC, subcutaneous.

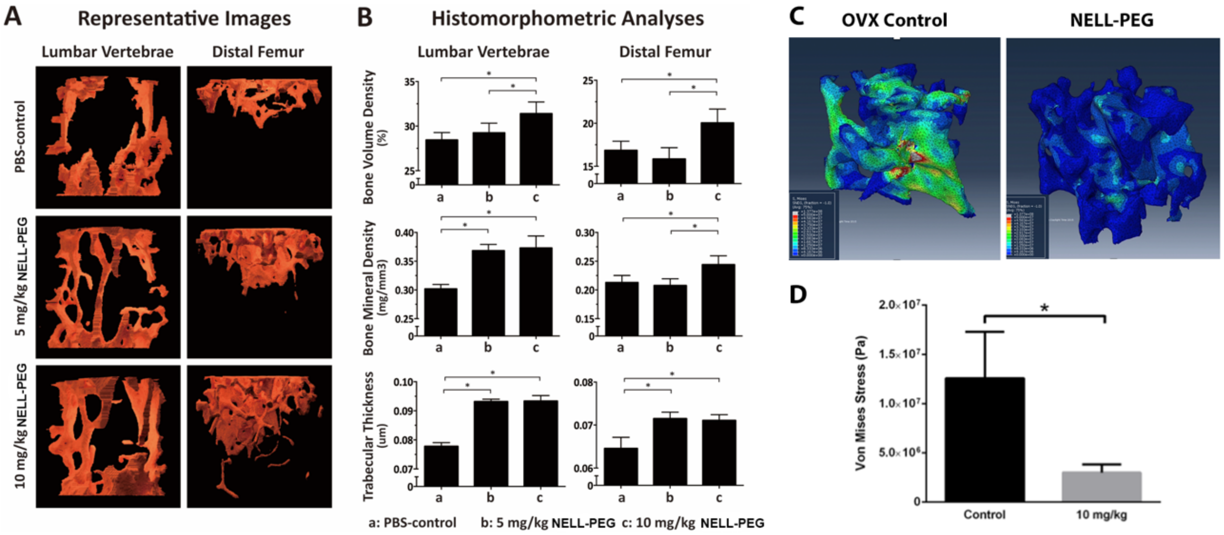

Figure 12. Micro-CT and biomechanical loading test results for systemic NELL-PEG therapy at different doses. (A-B) In order to further confirm the injection dose, we included a 5mg/kg IP injection group along with a 10mg/kg IP injection group (dose previously confirmed) and an OVX control group. (A) shows representative images for distal femur and lumbar vertebrae generated from 3D reconstruction of trabecular bone micro-CT datasets. There is appreciable increase in bone volume in treatment groups compared to control, both in lumbar and femur, with the 10mg/kg injection group showing more trabecular bone volume than 5mg/kg. (B) shows the quantified results for trabecular bone BMD, BV/TV and Tb/Th. As shown in the bar graphs, 5mg/kg NELL-PEG significantly increased BMD at lumbar vertebrae by15.8% but not at distal femur. Tb.Th at both lumbar vertebrae and distal femur were increased. However, 10mg/kg NELL-PEG therapy had more consistent results, BV/TV (17.6% at distal femur, 12.5% at lumbar vertebrae), BMD (16.8% at distal femur, 20.9% at lumbar vertebrae) and Tb.Th were all increased significantly by treatment and with no site differences. (C). Finite element analysis was utilized to test the ability to resist fractures of femoral trabecular bone. Trabecular bone mesh models of equal cubic volume and consistent femoral location were generated for each sample. The physiologic force was chosen to be 0.5 MPa (mega Pascals) based on literature for mice. The force was applied from a superior to inferior direction, loading the axial cross-section. Blue regions represent stronger bones which are more resistant to fracture, as shown in the NELL-PEG treated group, and yellow and red regions, as shown in the OVX control group, represent weaker bone. (D) The bar graph shows the Von Mises stress values for both groups. A high von Mises stress value denotes lower strength, while a lower value is indicative of higher strength. The OVX control group showed significantly higher Von Mises stress with larger variations compared to treatment group. For the micro-CT analysis, the region of interest for femoral and tibial trabecular bone was defined as 4mm extending up from the distal growth plate of femur and 3mm extending down from the proximal growth plate of tibia (a clearance of 0.1mm from the growth plate was maintained for all the samples). $^*p<0.05$. BMD, bone mineral density; BV/TV, bone volume/tissue volume; Tb.Th, trabecular thickness; Tb.Sp, trabecular separation.

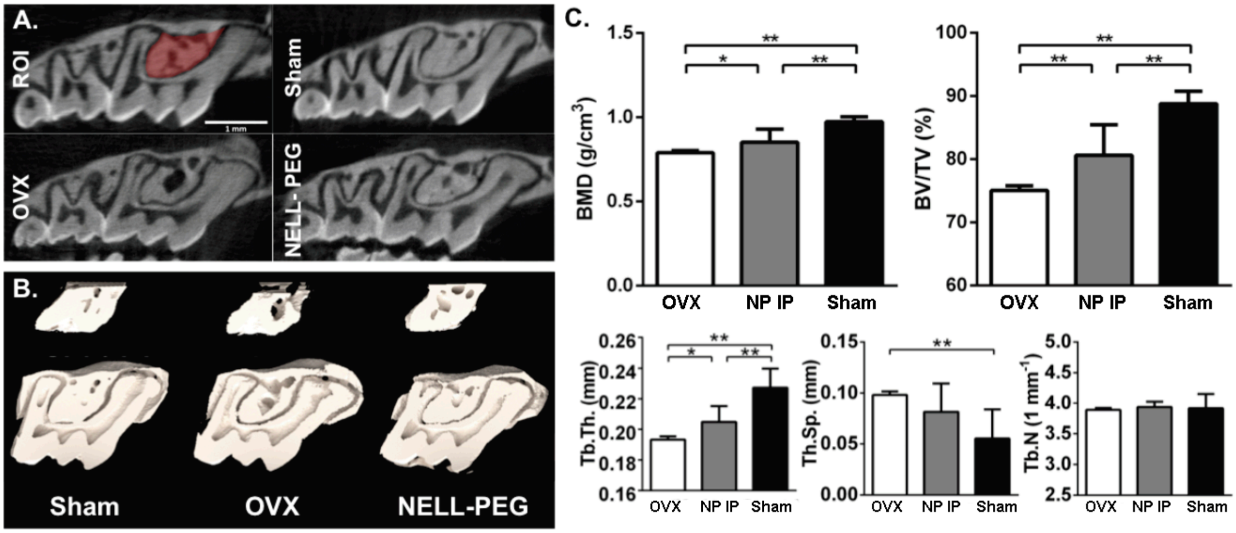

Figure 13. Systemic NELL-PEG therapy regenerates dento-alveolar bone in OVX mice. Micro-CT analysis was performed at 8 weeks of treatment (n=10/group). (A) 2D sagittal cuts through mid-crown of the maxillary first molar. ROI (in red) was hand-drawn to enclose intra-radicular space under the molar. (B) 3D reconstruction of the analyzed region (top row) and overview (bottom row). (C) Quantification of BMD, BV/TV, and Tb.Th, N, and Sp. *$p<0.05$, **$p<0.01$. NP, NELL-PEG; ROI, region of interest; BMD, bone mineral density; BV/TV, bone volume/tissue volume; Tb.Th, trabecular thickness; Tb.Sp, trabecular separation.

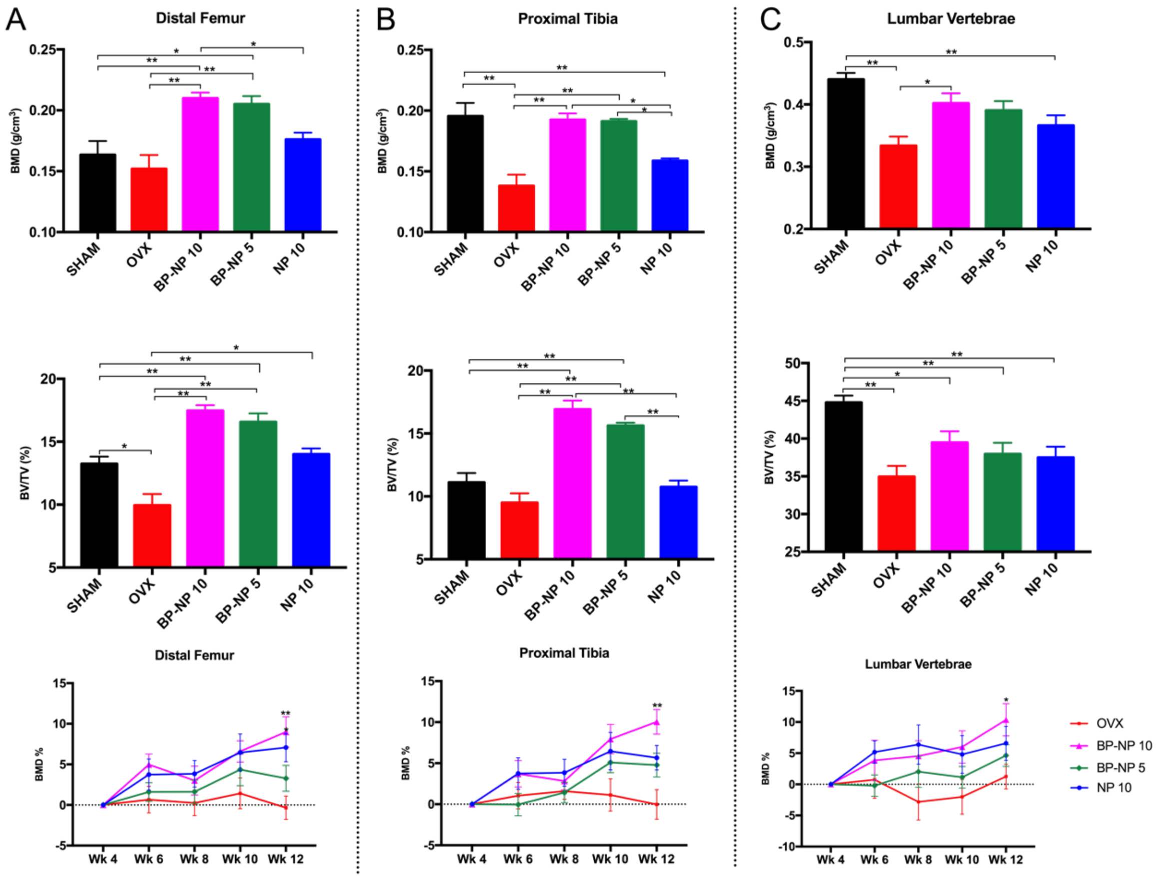

Figure 14. Micro-CT and DXA results of treatment effects comparison between NELL-PEG and BP-NELL-PEG. After the OVX model was confirmed to successfully induce bone loss, different treatment groups were injected with NELL-1 based therapies (n=8 per group). After 4 injections, performed every other week (8weeks of treatment in total), results were as shown above. For micro-CT analysis, the region of interest for femoral and tibial trabecular bone was defined as 4mm extending up from the distal growth plate of femur and 3mm extending down from the proximal growth plate of tibia (a clearance of 0.1mm from the growth plate was maintained for all the samples). (A) For the distal femur, both BP-NP at 10mg/kg or 5mg/kg increased BMD significantly. Both treatment groups increased BMD and BV/TV to levels higher than Sham control. Significant treatment effects were also present in the NP 10mg/kg group, but only in BV/TV, and were not as prevalent as with BP-NP groups. For DXA BMD at the distal femur, BP-NP 10mg/kg group had the highest BMD change at 8.6% at the end time point (Wk12). (B) Proximal tibia results had similar trends as distal femur. For both BP-NP 10mg/kg and 5mg/kg groups, significant increases in BMD and BV/TV were observed, compared to OVX control. There was no significant difference between Sham and BP-NP groups in BMD, but for BV/TV, both groups had higher bone volume than Sham. For proximal tibia, BP-NP 10mg/kg group showed significantly higher BMD changes compare to control at around 9.8%. BP-NP 5mg/kg and NP 10mg/kg group had comparable results of 5-6% increase to BMD. (C) For lumber vertebra, BP-NP 10mg/kg group showed significant increases in BMD compared to OVX control. Similar BMD changes were seen in lumbar vertebrae DXA results as well. The BP-NP 10mg/kg group had almost 10% increase in BMD. For all DXA analyses, the signifcance shown is in comparison to OVX control with only the end time point marked. * $p<0.05$, ** $p<0.01$. NP 10, NELL-PEG at 10mg/kg; BP-NP 5, BP-NELL-PEG at 5mg/kg; BP-NP 10, BP-NELL-PEG at 10mg/kg; BMD, bone mineral density; BV/TV, bone volume/tissue volume.

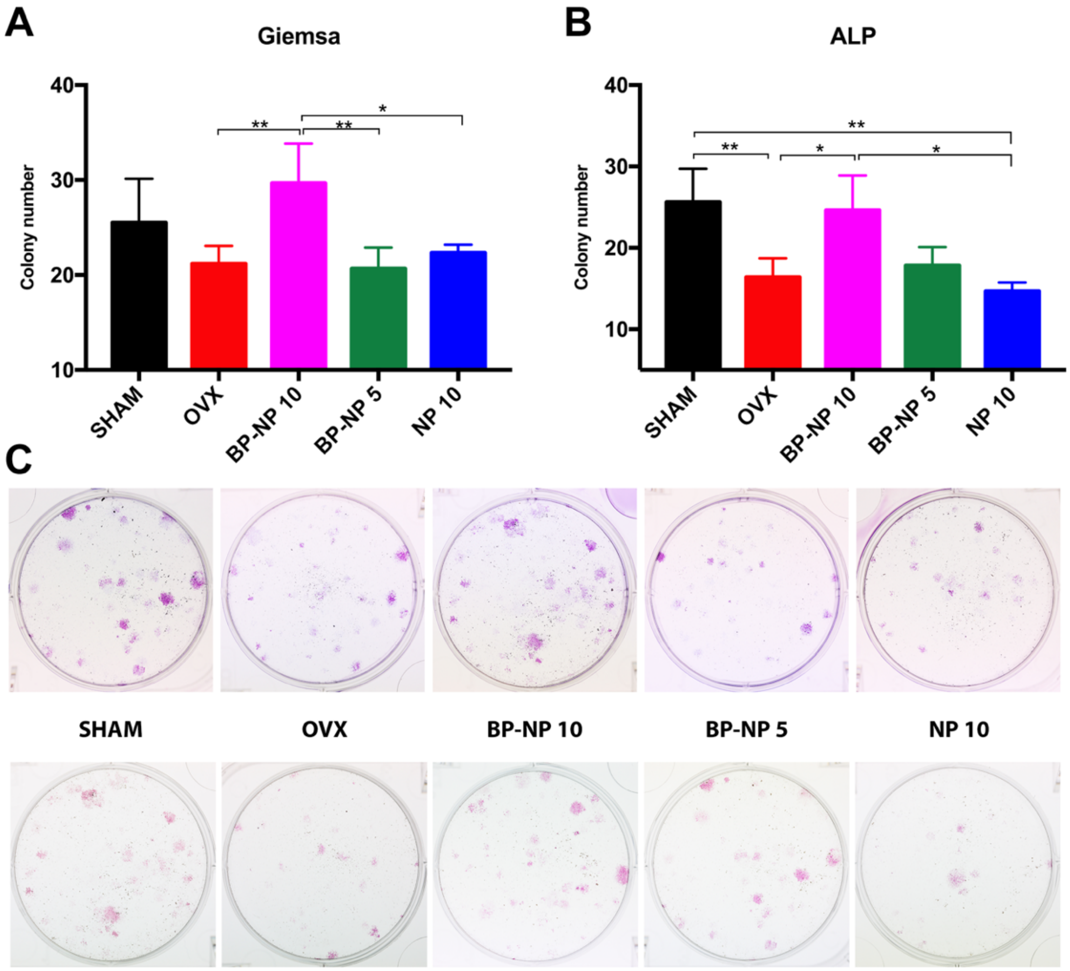

Figure 15. Colony-forming unit fibroblasts (CFU-F) assay results. (A) CFU-F-derived colonies were stained using Alkaline Phosphatase. ALP stained colonies were quantified by manual microscopy counting. The BP-NP 10mg/kg group exhibited significant increases in ALP expression compared to the control group. (B) Giemsa Stain Solution was used to stain the same colony culture plates to quantify total colony numbers. The BP-NP 10mg/kg group still had the most BMSC colonies, at around the same level as Sham control. Representative images of each group are presented below the bar graphs in (C). *p < 0.05, ** p<0.01. BMSC, bone marrow stem cell; NP 10, NELL-PEG at 10mg/kg; BP-NP 10, BP-NELL-PEG at 10mg/kg; BP-NP 5, BP-NELL-PEG at 5mg/kg; ALP, alkaline phosphatase.

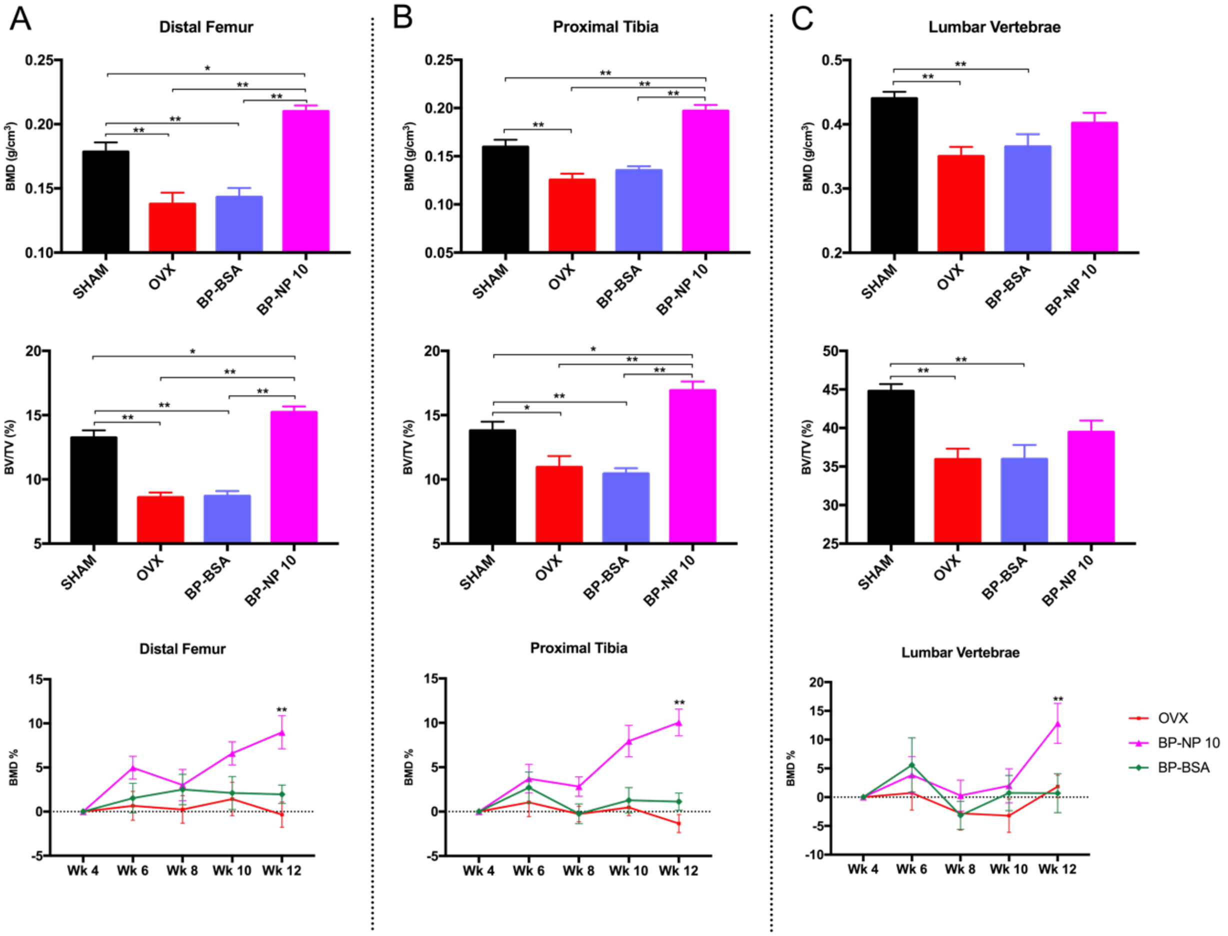

Figure 16. Conjugated bisphosphonate has no therapeutic effects in vivo. To further confirm that the BP conjugated to NELL-PEG was inactivated, we performed 4 injections, every other week, and scanned the samples at the end of the study to compare trabecular bone quality and quantity. For micro-CT analysis, the region of interest for femoral and tibial trabecular bone was defined as 4mm extending up from the distal growth plate of femur and 3mm extending down from the proximal growth plate of tibia (a clearance of 0.1mm from the growth plate was maintained for all the samples). For lumbar vertebrae, the region of interest covered the trabecular bone region of the entire vertebral body, not including the epiphyseal plate or cortical bone. (A-B) For distal femur and proximal tibia, BP-NP at 10mg/kg had significant treatment effects and increased BMD and BV/TV to levels greater than Sham control. There was no significant difference between OVX control and BP-BSA group, indicating that the injections did not promote bone growth. (C) For lumbar vertebrae, the BP-NP 10mg/kg group showed increases for both BMD and BV/TV, although not significant. As in long bone, BP-BSA did not exhibit any treatment effects. For (A-C) DXA, general trends of BMD change were consistent between all three bone sites. BMD at Wk 12 of both BP-BSA and OVX control groups did show significant differences from the starting point. The BP-NP 10mg/kg group showed significant bone growth at the end of the study. There were 8.7%, 10.5% and 12.3% of BMD increase at distal femur, proximal tibia and lumbar vertebra separately. *p<0.05, ** p<0.01. BP-NP 10, BP-NELL-PEG at 10mg/kg; BP-BSA, BP-Bovine serum albumin at 5.11mg/kg; Wk, week.

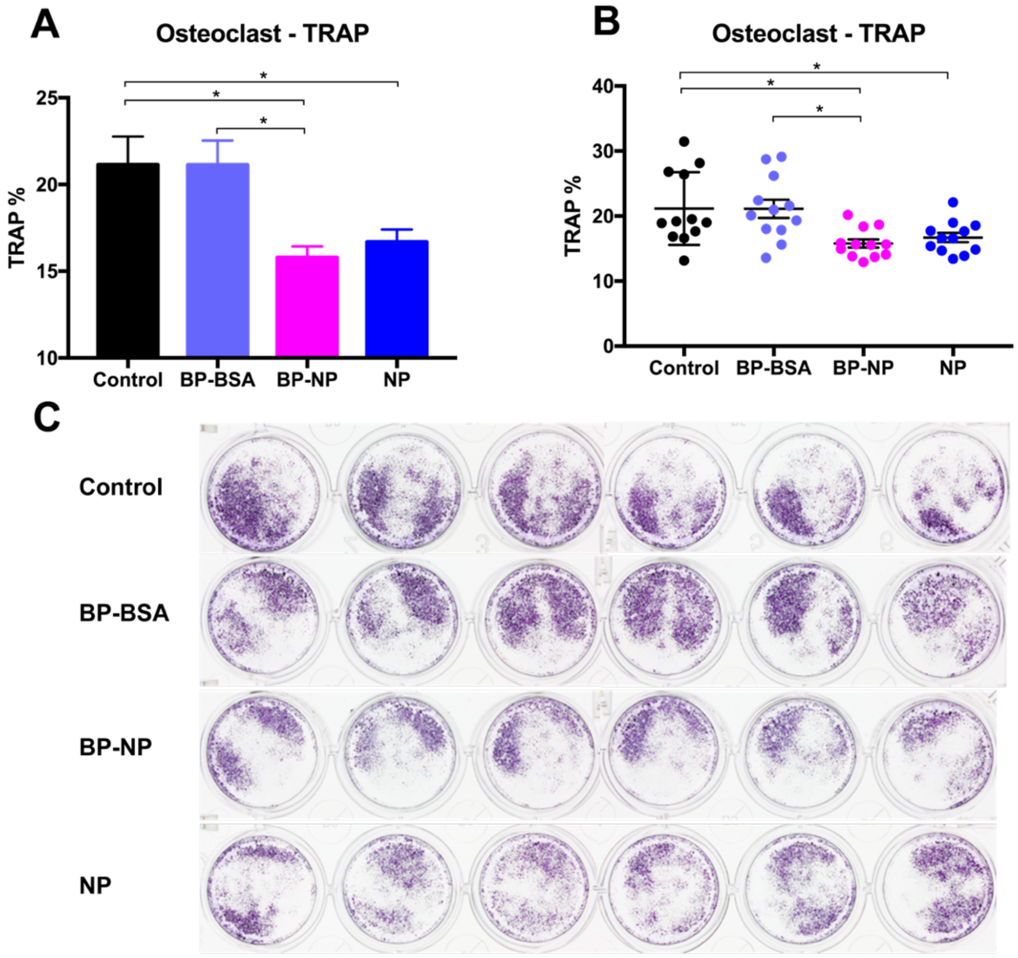

Figure 17. Osteoclasts culture with different in vitro treatments. Bone marrow cells were flushed from mouse humeri and cultured with different treatment agents for 6 days continuously during the osteoclasts induction stage (NP and BP-NP at 800ng/ml, BP-BSA at 408.8ng/ml of protein content to ensure the same molar concentration of BP molecules). (A) shows both BP-NELL-PEG and NELL-PEG treatment exhibited strong anti-osteoclasts effects, with no significant difference between them. There was no difference between blank control and BP-BSA, showing that BP conjugated to BSA is inactivated. (B) The dotted graph shows the distribution of TRAP staining for each group. (C) The representative images of TRAP staining. *p<0.05, ** p<0.01. NP, NELL-PEG; BP-NP, BP-NELL-PEG; BP-BSA, BP-Bovine serum albumin; TRAP, tartrate-resistant acid phosphatase.

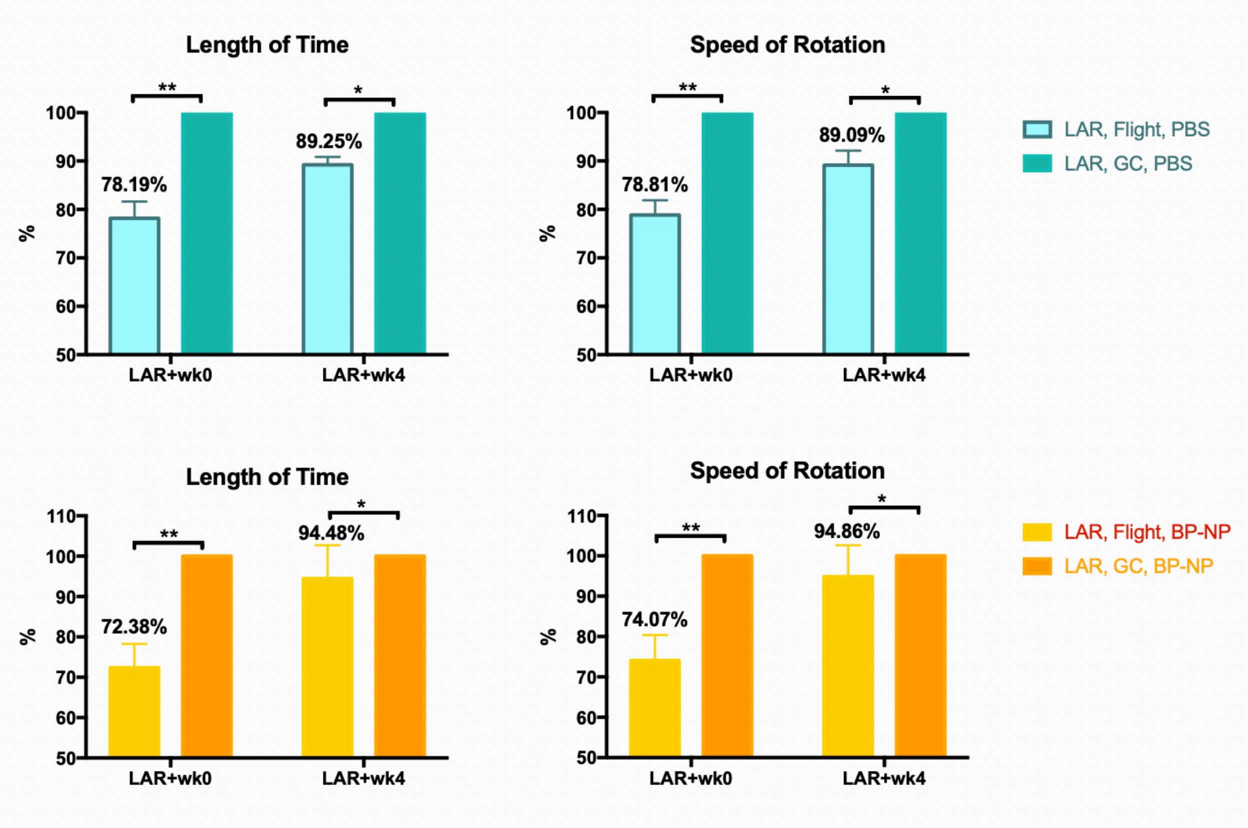

Figure 18. Motor function test of live-return groups. Rota rod tests were performed on live-return groups immediately upon live-return (LAR+wk0) and 4wks after (LAR+wk4). We found that 5 weeks of spaceflight caused 20% reduction in motor function compared to ground controls regardless of BP-NELL-PEG treatment (B) or not (A). Motor function was only recovered by around 10% after 4 weeks on earth in PBS groups, but the NELL-1 therapy treated groups recovered over 20% for both the length of time that mice can stay on the rod and the maximal speed that the mice can handle. *p<0.05, **p<0.01. LAR, live-return; Flight, space flight group; GC, ground control; BP-NP, BP-NELL-PEG.

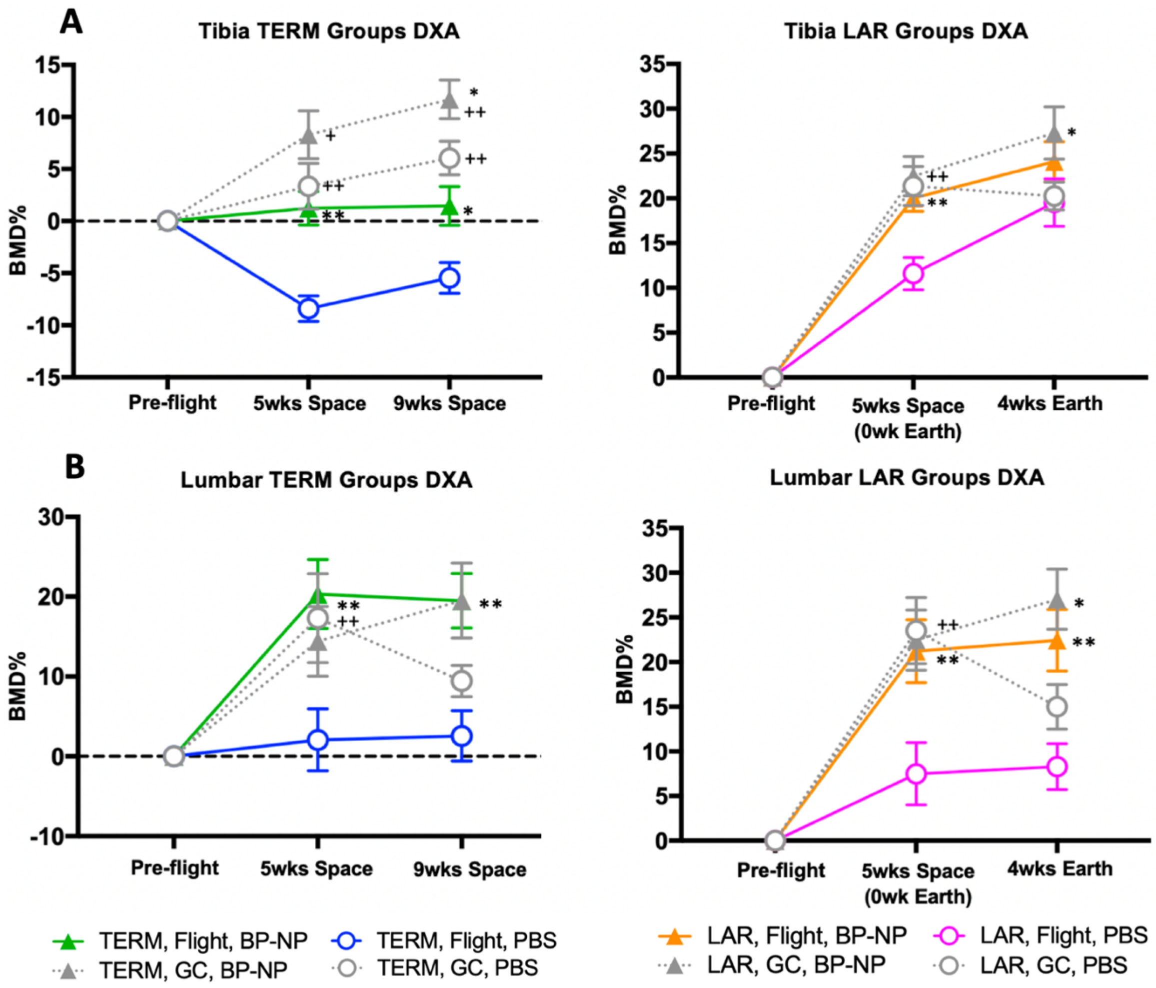

Figure 19. Flight Operation DXA results. (A) proximal tibia DXA comparison for terminal and live return groups. For TERM groups, microgravity exposure resulted in significant bone loss in proximal tibia after 5 and 9 weeks of space travel, for both BP-NELL-PEG treated and untreated animals, compared to ground controls (gray triangle vs green triangle, gray circle vs blue circle). For the flight treatment group (green triangle), the BMD% is significantly higher at both 5 and 9 weeks in space time points compared to flight PBS group (blue circle). For the ground treatment group (gray triangle), the BMD% is significantly higher at 9 weeks in space compared to ground PBS group (gray circle). For LAR groups, significant treatment effects were observed at 5 weeks into space flight for flight groups (orange triangle vs pink circle) and persisted even after 4 weeks of recovery on Earth (5 weeks in space followed by 4 weeks on Earth) for ground control groups (gray triangle vs gray circle). (B) lumbar vertebrae 6 DXA comparison for terminal and live return groups. For all groups, microgravity effects were observed only after 5 weeks in space for PBS groups (gray circle vs blue circle, gray circle vs orange circle). As for treatment, in TERM groups, BP-NELL-PEG treatment increased the BMD% significantly at both 5 weeks in space and 9 weeks in space in flight groups (green triangle vs blue circle). For LAR groups, treatment was significant at both 5 weeks in space time point and end time point (5 weeks in space followed by 4 weeks on Earth) in flight groups (orange triangle vs pink circle); ground groups showed significant treatment result at the end time point (gray triangle vs gray circle). * label for NELL-1 therapy treatment significance; + label for microgravity effects significance. *$p<0.05$, +$p<0.05$; +$p<0.05$, ++$p<0.01$. BP-NP, BP-NELL-PEG; TERM, terminal groups; LAR, live return groups; GC, ground control groups; Flight, flight groups.

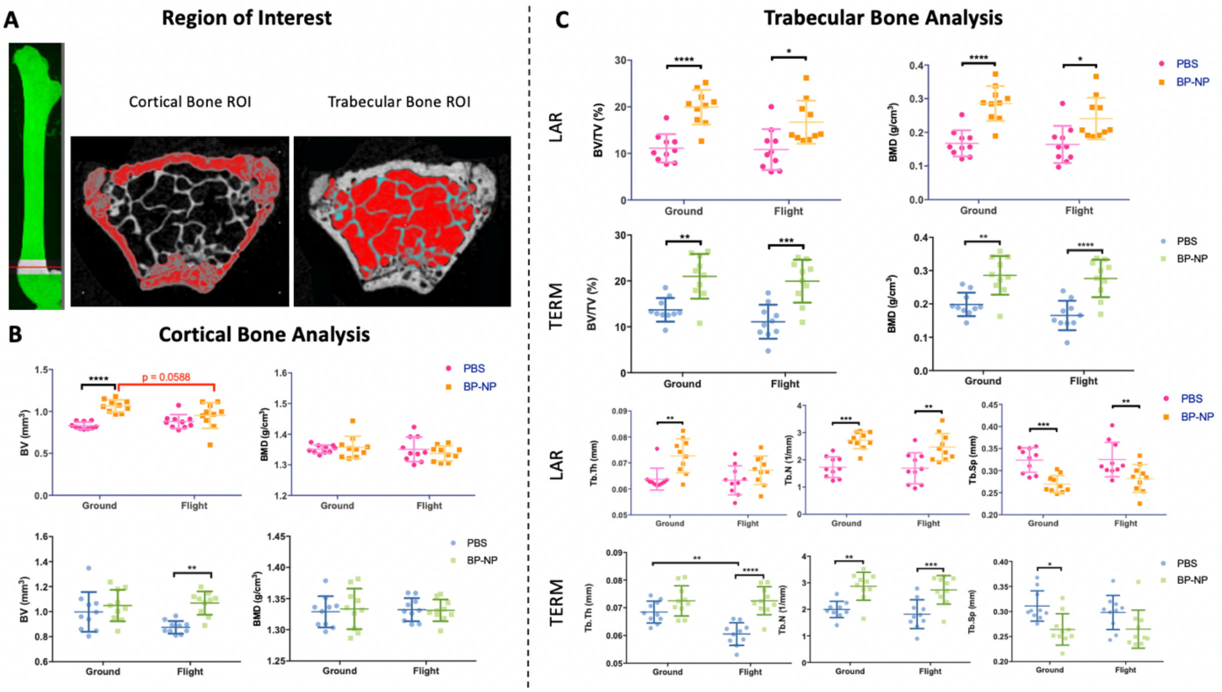

Figure 20. Micro-CT trabecular bone analysis of distal femur (flight operation samples). High-resolution micro-CT was used to scan femur samples for trabecular bone analysis. The region of interest for femoral trabecular bone was defined as 1mm extending up from the distal growth plate (a clearance of 0.3mm from the growth plate was maintained for all the samples). BP-NELL-PEG treatment increased bone quality and quantity in almost all measured parameters, regardless of whether animals were on ground or in space. Thresholds were set as 150 for cortical bone analysis and 90 for trabecular bone analysis. *$p<0.05$, ** $p<0.01$, ***$p<0.001$, ****$p<0.0001$. TERM, terminal groups; LAR, live return groups; BP-NP, BP-NELL-PEG; ROI, region of interest; BMD, bone mineral density; BV/TV, bone volume/tissue volume; Tb.Th, trabecular thickness; Tb.Sp, trabecular separation.

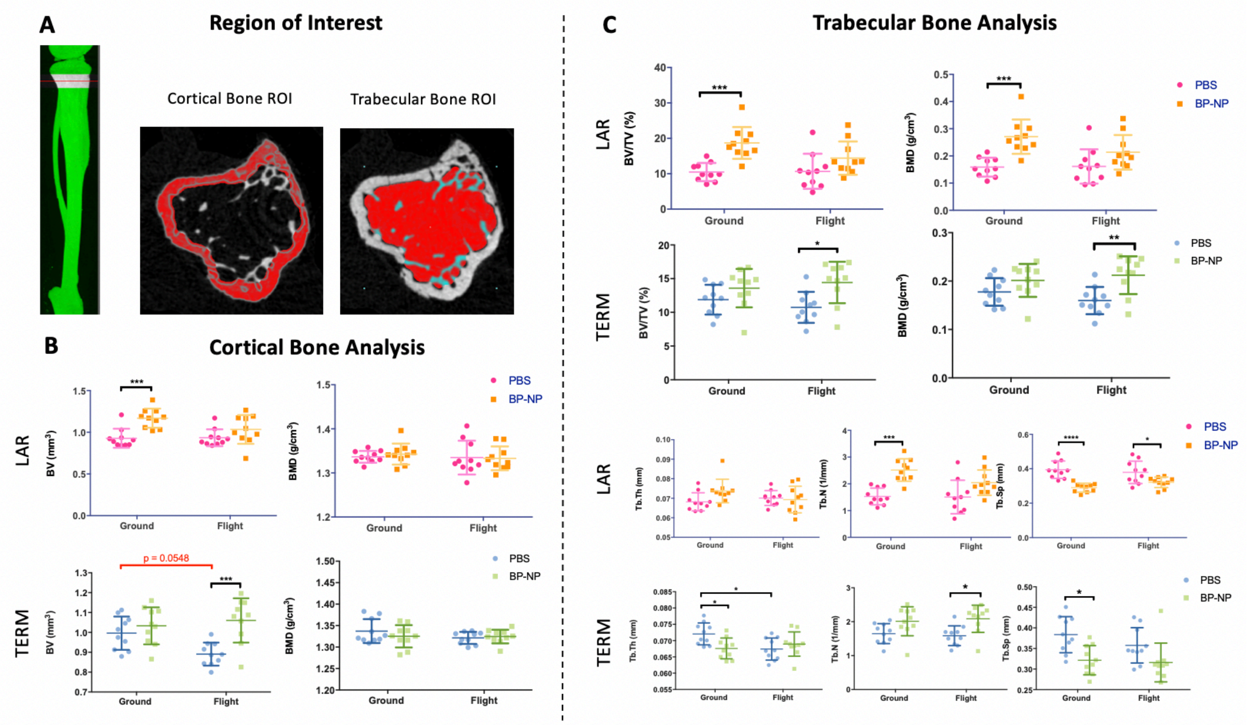

Figure 21. Micro-CT trabecular bone analysis of proximal tibia (flight operation samples). High-resolution micro-CT was used to scan tibia samples for trabecular bone analysis. The region of interest for tibial trabecular bone was defined as 1mm extending up from the proximal growth plate (a clearance of 0.1mm from the growth plate was maintained for all the samples). Thresholds were set as 150 for cortical bone analysis and 90 for trabecular bone analysis. BP-NELL-PEG treatment increased tibial bone quality and quantity regardless of whether animals were on ground or in space. $*p<0.05$, $** p<0.01$, $***p<0.001$. TERM, terminal groups; LAR, live return groups; BP-NP, BP-NELL-PEG; ROI, region of interest; BMD, bone mineral density; BV/TV, bone volume/tissue volume; Tb.Th, trabecular thickness; Tb.Sp, trabecular separation.

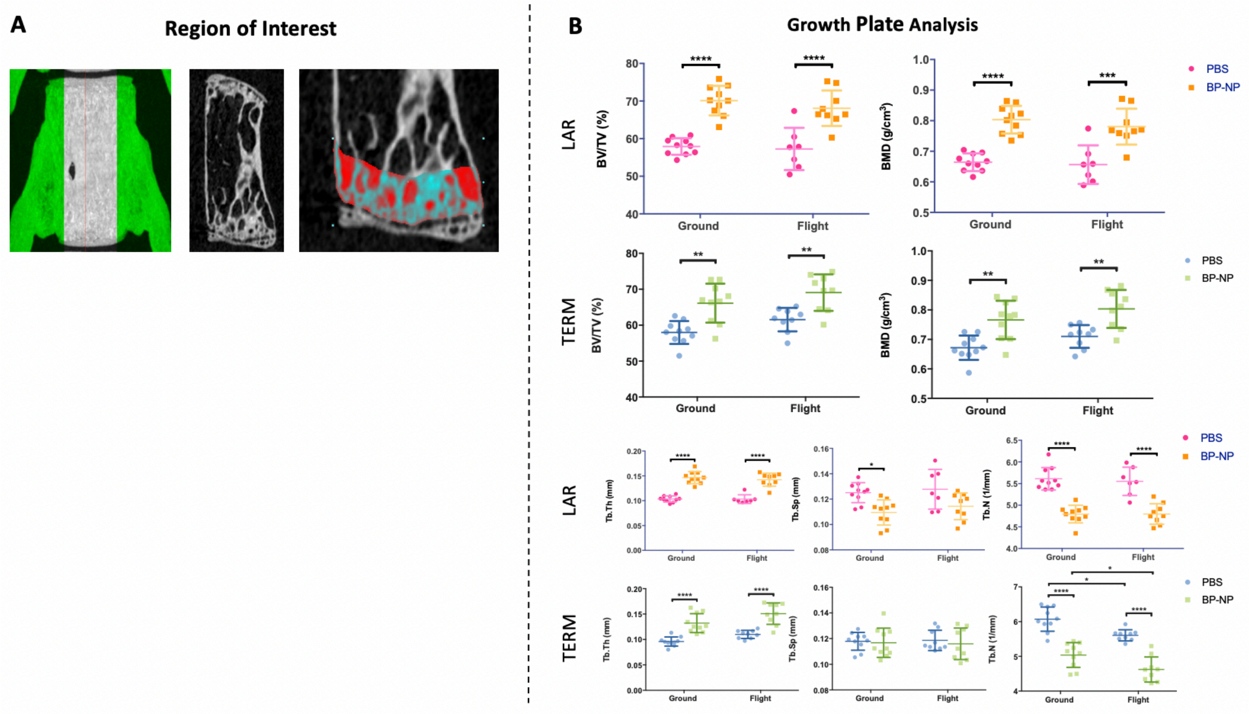

Figure 22. Micro-CT trabecular bone analysis of lumbar vertebrae (flight operation samples). High-resolution micro-CT was used to scan lumbar vetebrae samples for growth plate analysis. The region of interest for lumbar growth plate was individually specified, extending up from the distal fused zygapophyses to include the entire distal growth plate region. A threshold of 90 was used for analysis. BP-NELL-PEG treatment significantly increased bone quality and quantity, regardless of whether animals were on ground or in space. $^{*}p<0.05$, $^{**}p<0.01$, $^{***}p<0.001$, $^{****}p<0.0001$. TERM, terminal groups; LAR, live return groups; BP-NP, BP-NELL-PEG; ROI, region of interest; BMD, bone mineral density; BV/TV, bone volume/tissue volume; Tb.Th, trabecular thickness; Tb.Sp, trabecular separation.

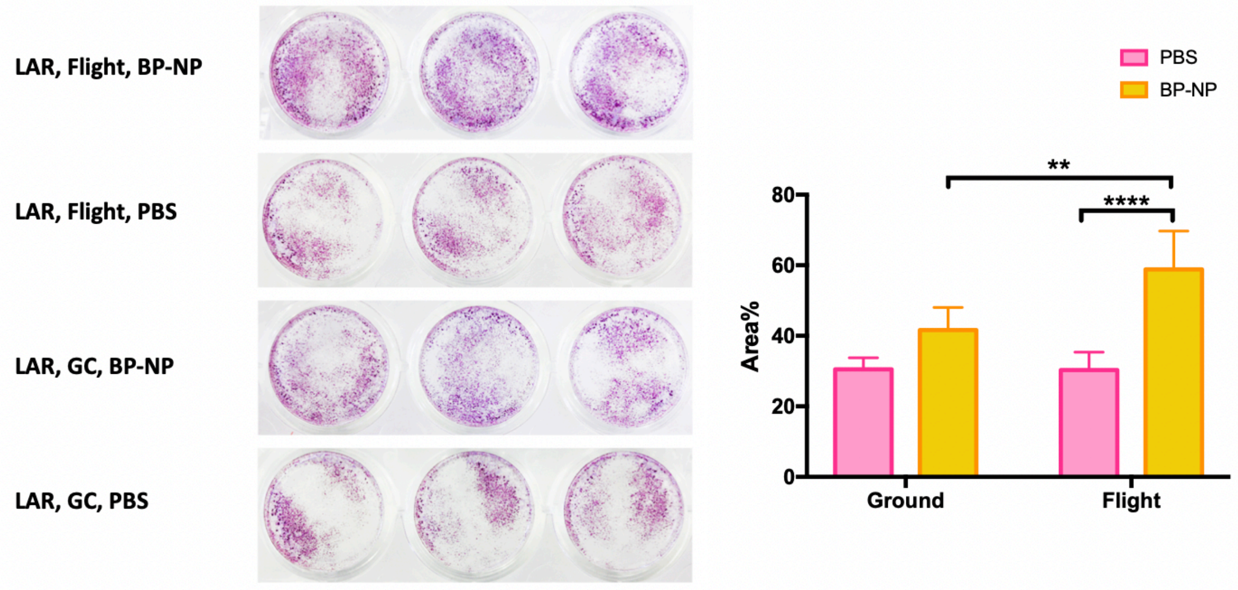

Figure 23. The osteoclasts TRAP staining results of the live return groups. Osteoclasts were isolated from flushed bone marrow cells and cultured for macrophage and osteoclast induction. TRAP staining was used to stain osteoclasts. The images on the left are representative of staining from each group. Quantification of TRAP staining is shown in the bar graph to the right. BP-NELL-PEG treated flight group had significantly higher osteoclast number compared to the PBS group. The flight treatment group had significantly higher osteoclast counts compared to the ground treatment group. **p<0.01, ****p<0.0001. LAR, live-return; Flight, flight groups; GC, ground control groups; BP-NP, BP-NELL-PEG; TRAP, tartrate-resistant acid phosphatase.

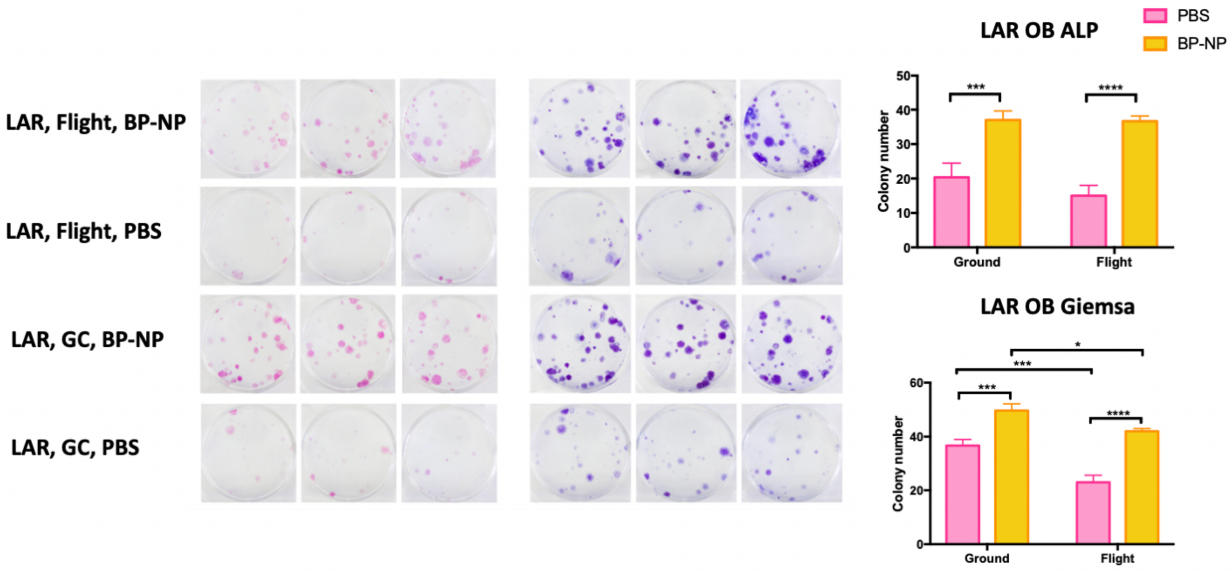

Figure 24. Colony-forming unit fibroblasts (CFU-F) assay results of the live return groups. BMSCs from all groups were flushed from mouse humeri and cultured. Colonies were first stained with ALP, then with Giemsa. BMSC content was quantified by counting colonies. Representative images for each group are shown on the left. ALP staining showed that in both BP-NELL-PEG treated groups, regardless of whether animals were in space or on ground, there were significantly more osteogenic colonies. There was no difference between flight and ground treatment groups. Giemsa staining showed significantly more colonies stained in both flight and ground treatment groups. Microgravity significantly reduced the number of colonies in both BP-NELL-PEG treated groups and PBS control groups. *$p<0.05$, **$p<0.01$, ***$p<0.001$, ****$p<0.0001$. LAR, live-return; Flight, flight groups; GC, ground control groups; BP-NP, BP-NELL-PEG; ALP, alkaline phosphatase.

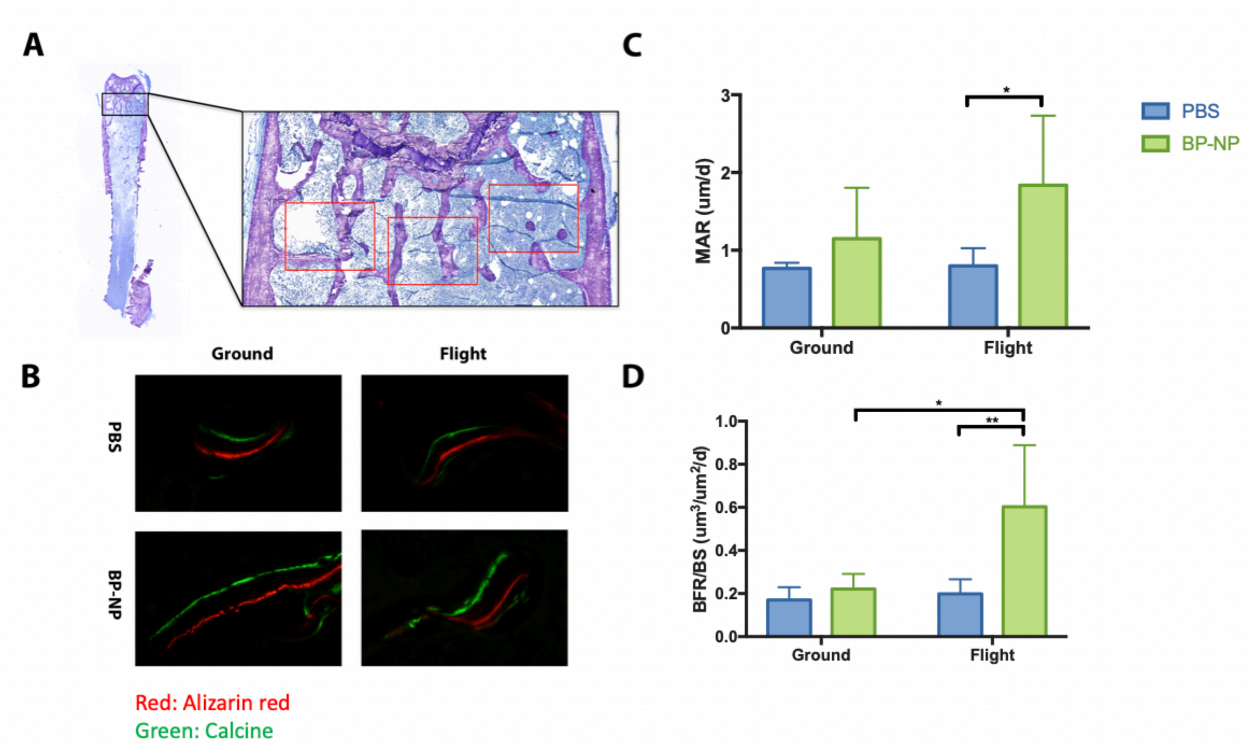

Figure 25. Dynamic histomorphometric analyses results of terminal groups. For bone fluorescent-labelling studies, mice were injected intraperitoneally with calcein (20 mg/kg), alizarin Dynamic histomorphometric analyses red complexon (50 mg/kg) and calcein (20 mg/kg) at week 3, 5 and 7 post-launch, respectively. (A) shows the region of interest (ROI) used for analysis. The_fixed area located beneath the growth plate of distal femur trabecular bone was selected as the ROI (3 measurement fields per sample). All image acquisition and analyses were performed in a blinded manner. (B) shows representative images of bone labeling of the different groups. Three lines of calcein and alizarin red are clearly visible. BP-NELL-PEG treated groups show generally wider distances between each label. (C) The quantification for dynamic histomorphometry. The MAR (mineral apposition rate, mm per day) were measured in unstained sections under ultraviolet light. The flight treatment group had significantly higher MAR compared to its PBS control. (D) The bone formation rate with a bone surface referent (BFR/BS, um^3*um^{-2} per year) was calculated from the MAR. The bone formation rate per bone surface (BFR/BS) is the volume of mineralized bone formed per unit time and per unit bone surface. Following the MAR trend, the BP-NP treated flight group had much higher BFR/BS rates compared to PBS controls. *p<0.05, **p<0,01. TERM, terminal groups; Flight, flight groups; GC, ground control groups; BP-NP, BP-NELL-PEG; MAR, mineral apposition rate; BFR/BS, bone formation rate per bone surface.

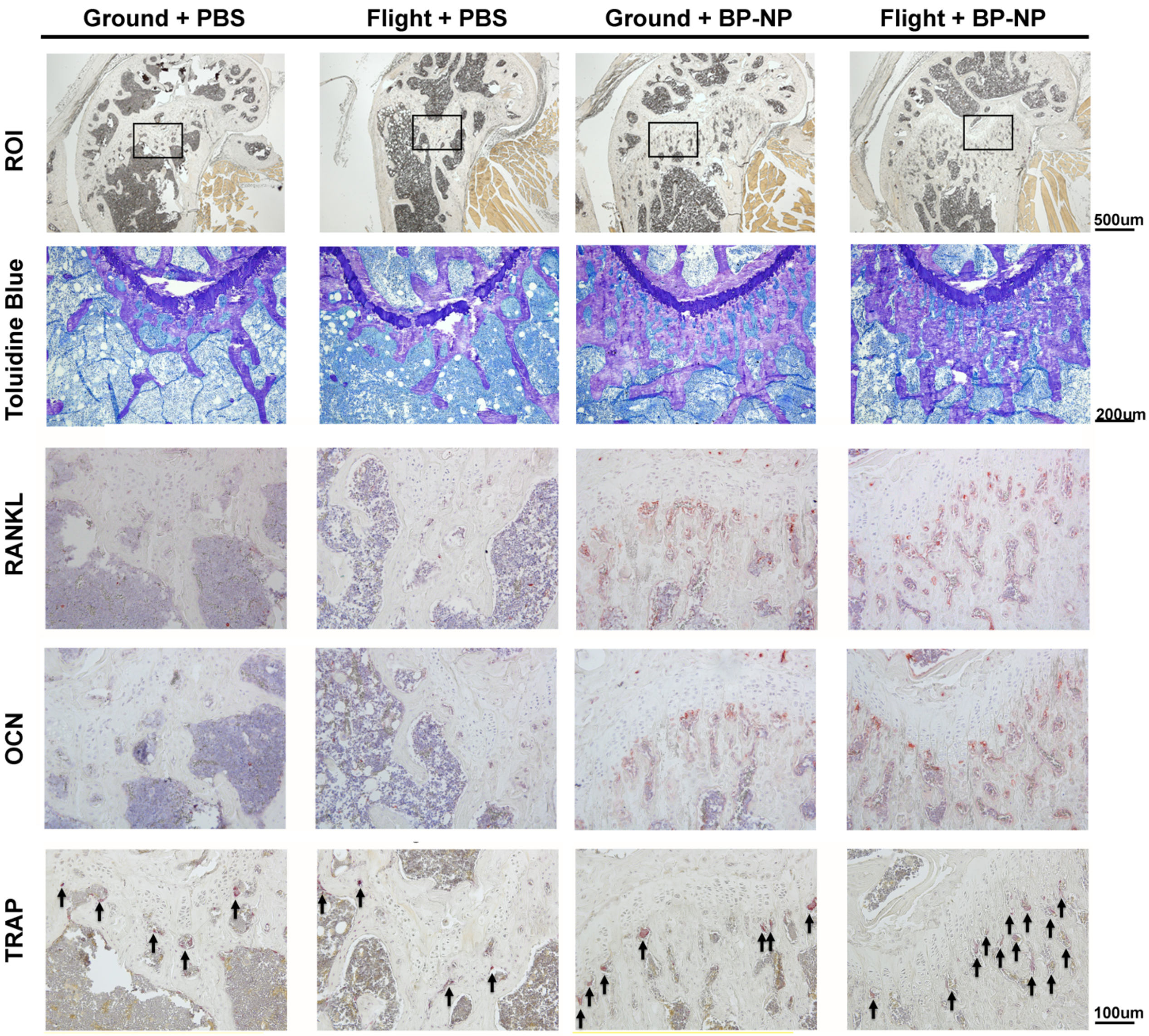

Figure 26. Histological, immunohistochemistry and TRAP staining of terminal groups. The black boxes in the 1st row of images show the region of interest for staining. H&E and toluidine blue staining exhibited greater trabecular bone formation at the distal femoral metaphysis in the BP-NP treated group compared to control. Osteocalcin (OCN) immunostaining exhibited a greater number of OCN positive cells with intense staining in the BP-NP treated groups and TRAP staining exhibited an increase in TRAP positive cells in treated femurs compared to control. ROI, region of interest; BP-NP, BP-NELL-PEG; TRAP, tartrate-resistant acid phosphatase.

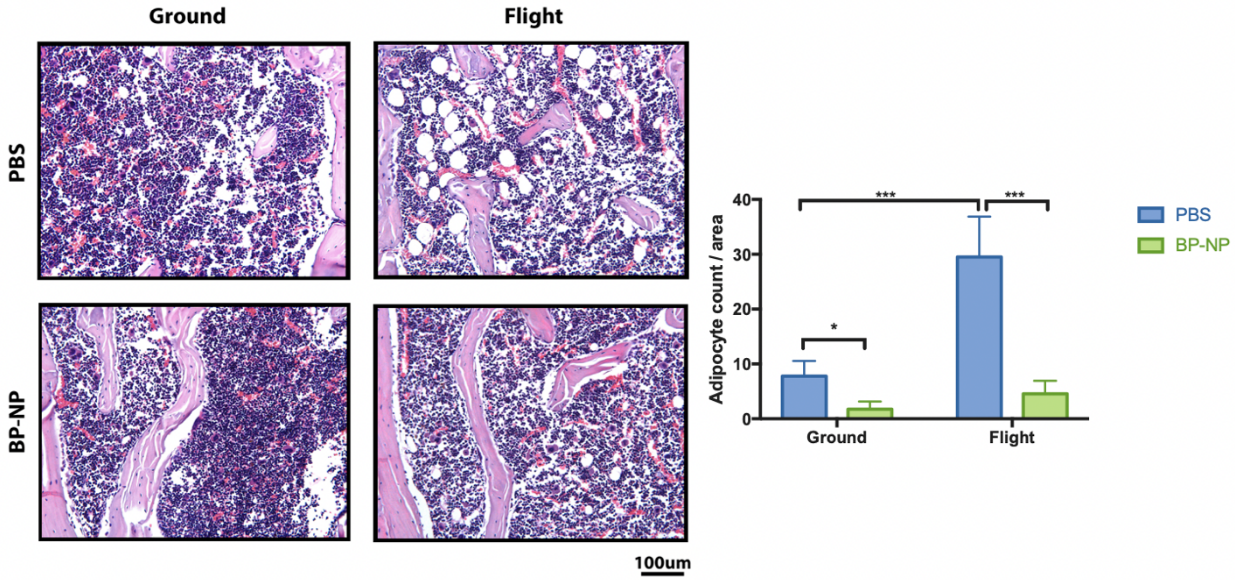

Figure 27. H&E staining for femur bone marrow lipid counts. histology images on the left are representative of the femur bone marrow with quantification of adipocytes shown in the bar graph to the right. Results showed significantly decreased lipid vacuoles with BP-NELL-PEG treatment and significantly increased lipid vacuoles with microgravity exposure. BP-NP, BP-NELL-PEG. *p<0.05, ***p<0.001.

Group	Flight Duration	Treatment	Animal #
Flight	9 weeks (Terminal groups)	BP-NELL-PEG	10
		PBS control	10
	4 weeks (Live-return groups)	BP-NELL-PEG	10
		PBS control	10
Ground	9 weeks (Terminal groups)	BP-NELL-PEG	10
		PBS control	10
	4 weeks (Live-return groups)	BP-NELL-PEG	10
		PBS control	10
Baseline			20
Total			100

Table 1. Experimental groups of Flight Operation (Rodent Research-5 mission)

Sites	Measurements	Mean (± SD)	Maximum	Minimum
Distal femur	EPD (mm)	3.81 (±0.15)	4	3.58
	EPA (°)	14.62 (±1.8)	17	11
Proximal tibia	EPD (mm)	2.36 (±0.08)	2.5	2.25
	EPA (°)	7.54 (±1.44)	10	5
Lumbar vertebrae				
L5	Height (mm)	3.02 (±0.09)	3.14	2.85
	Width (mm)	1.64 (±0.10)	1.76	1.47
L6	Height (mm)	3.04 (±0.09)	3.21	2.92
	Width (mm)	1.51 (±0.05)	1.59	1.42
	ID (mm)	1.13 (±0.79)	2.07	-0.81

Table 2. Results of anatomic analysis

EPA, epiphyseal plate angle; EPD, epiphyseal plate distance; ID, distance between the intervertebral space of L5/6 and intercristal line; SD, standard deviation.

	Inter-observer reliability		Intra-observer reliability	
Sites	ICC	95% CI	ICC	95% CI
Distal femur	0.945	0.923, 0.972	0.964	0.939, 0.995
Proximal tibia	0.932	0.0887, 0.973	0.952	0.924, 0.988
L6	0.801	0.764, 0.843	0.835	0.810, 0.858
L5	0.743	0.647, 0.831	0.783	0.683, 0.879

Table 3. Inter- and Intra-Observer Reliability of DXA BMD Measurement at Various Trabecular Bone-Rich Sites

BMD, bone mineral density; CI, confidence interval; DXA, dual energy X-ray absorptiometry; ICC, intra-class correlation.

Sites	Terms	New method	Conventional method
Distal femur	Mean (%)	2.77	2.64
	SD	0.076[a]	0.108
	CV	2.726	4.089
Proximal tibia	Mean	2.89	2.97
	SD	0.0727[b]	0.089
	CV	2.516	2.994
Lumbar Vertebrae	Mean	3.96	1.94
	SD	0.099[a]	0.147
	CV	2.507	7.576

Table 4. Results of BMD Percentage Changes of Every 2 weeks in DXA by New and Conventional Methods

a Significant at $p < 0.01$ compared to SD of conventional method.
b Significant at $p < 0.05$ compared to SD of conventional method.
CV, coefficient of variation.

5 REFERENCES

1. Berry SD, Kiel DP, Donaldson MG, Cummings SR, Kanis JA, Johansson H, Samelson EJ. Application of the National Osteoporosis Foundation Guidelines to postmenopausal women and men: the Framingham Osteoporosis Study. Osteoporosis international : a journal established as result of cooperation between the European Foundation for Osteoporosis and the National Osteoporosis Foundation of the USA. 2010;21(1):53-60. Epub 2009/11/26. doi: 10.1007/s00198-009-1127-3. PubMed PMID: 19937426; PMCID: PMC2889692.

2. Czerwinski E, Badurski JE, Marcinowska-Suchowierska E, Osieleniec J. Current understanding of osteoporosis according to the position of the World Health Organization (WHO) and International Osteoporosis Foundation. Ortopedia, traumatologia, rehabilitacja. 2007;9(4):337-56. Epub 2007/09/21. PubMed PMID: 17882114.

3. Heinemann DF. Osteoporosis. An overview of the National Osteoporosis Foundation clinical practice guide. Geriatrics (Basel). 2000;55(5):31-6; quiz 9. PubMed PMID: 10826263.

4. Jilka RL. Biology of the basic multicellular unit and the pathophysiology of osteoporosis. Medical and pediatric oncology. 2003;41(3):182-5. Epub 2003/07/18. doi: 10.1002/mpo.10334. PubMed PMID: 12868116.

5. Shuler FD, Conjeski J, Kendall D, Salava J. Understanding the burden of osteoporosis and use of the World Health Organization FRAX. Orthopedics. 2012;35(9):798-805. Epub 2012/09/08. doi: 10.3928/01477447-20120822-12. PubMed PMID: 22955392.

6. Watts NB, Lewiecki EM, Miller PD, Baim S. National Osteoporosis Foundation 2008 Clinician's Guide to Prevention and Treatment of Osteoporosis and the World Health Organization Fracture Risk Assessment Tool (FRAX): what they mean to the bone densitometrist and bone technologist. Journal of clinical densitometry : the official journal of the International Society for

Clinical Densitometry. 2008;11(4):473-7. Epub 2008/06/20. doi: 10.1016/j.jocd.2008.04.003. PubMed PMID: 18562228.

7. Roche JJ, Wenn RT, Sahota O, Moran CG. Effect of comorbidities and postoperative complications on mortality after hip fracture in elderly people: prospective observational cohort study. BMJ (Clinical research ed). 2005;331(7529):1374. Epub 2005/11/22. doi: 10.1136/bmj.38643.663843.55. PubMed PMID: 16299013; PMCID: PMC1309645.

8. Lindsay R. The burden of osteoporosis: cost. The American journal of medicine. 1995;98(2a):9s-11s. Epub 1995/02/27. PubMed PMID: 7709941.

9. Pisani P, Renna MD, Conversano F, Casciaro E, Di Paola M, Quarta E, Muratore M, Casciaro S. Major osteoporotic fragility fractures: Risk factor updates and societal impact. World journal of orthopedics. 2016;7(3):171-81. Epub 2016/03/24. doi: 10.5312/wjo.v7.i3.171. PubMed PMID: 27004165; PMCID: PMC4794536.

10. Solomon DH, Johnston SS, Boytsov NN, McMorrow D, Lane JM, Krohn KD. Osteoporosis medication use after hip fracture in U.S. patients between 2002 and 2011. Journal of bone and mineral research : the official journal of the American Society for Bone and Mineral Research. 2014;29(9):1929-37. Epub 2014/02/19. doi: 10.1002/jbmr.2202. PubMed PMID: 24535775; PMCID: PMC4258070.

11. Bilezikian JP. Combination anabolic and antiresorptive therapy for osteoporosis: opening the anabolic window. Current osteoporosis reports. 2008;6(1):24-30. Epub 2008/04/24. PubMed PMID: 18430397.

12. Cusano NE, Bilezikian JP. Combination anabolic and antiresorptive therapy for osteoporosis. Endocrinology and metabolism clinics of North America. 2012;41(3):643-54. Epub 2012/08/11. doi: 10.1016/j.ecl.2012.04.005. PubMed PMID: 22877434.

13. Kawai M, Modder UI, Khosla S, Rosen CJ. Emerging therapeutic opportunities for skeletal restoration. Nature reviews Drug discovery. 2011;10(2):141-56. Epub 2011/02/02. doi: 10.1038/nrd3299. PubMed PMID: 21283108; PMCID: PMC3135105.

14. Miller PD, Derman RJ. What is the best balance of benefits and risks among anti-resorptive therapies for postmenopausal osteoporosis? Osteoporosis international : a journal established as result of cooperation between the European Foundation for Osteoporosis and the National Osteoporosis Foundation of the USA. 2010;21(11):1793-802. Epub 2010/03/24. doi: 10.1007/s00198-010-1208-3. PubMed PMID: 20309524.

15. Rachner TD, Khosla S, Hofbauer LC. Osteoporosis: now and the future. Lancet (London, England). 2011;377(9773):1276-87. Epub 2011/04/01. doi: 10.1016/s0140-6736(10)62349-5. PubMed PMID: 21450337; PMCID: PMC3555696.

16. Body JJ, Gaich GA, Scheele WH, Kulkarni PM, Miller PD, Peretz A, Dore RK, Correa-Rotter R, Papaioannou A, Cumming DC, Hodsman AB. A randomized double-blind trial to compare the efficacy of teriparatide [recombinant human parathyroid hormone (1-34)] with alendronate in postmenopausal women with osteoporosis. The Journal of clinical endocrinology and metabolism. 2002;87(10):4528-35. Epub 2002/10/05. doi: 10.1210/jc.2002-020334. PubMed PMID: 12364430.

17. Jilka RL. Molecular and cellular mechanisms of the anabolic effect of intermittent PTH. Bone. 2007;40(6):1434-46. Epub 2007/05/23. doi: 10.1016/j.bone.2007.03.017. PubMed PMID: 17517365; PMCID: PMC1995599.

18. Neer RM, Arnaud CD, Zanchetta JR, Prince R, Gaich GA, Reginster JY, Hodsman AB, Eriksen EF, Ish-Shalom S, Genant HK, Wang O, Mitlak BH. Effect of parathyroid hormone (1-34) on fractures and bone mineral density in postmenopausal women with osteoporosis. The New

England journal of medicine. 2001;344(19):1434-41. Epub 2001/05/11. doi: 10.1056/nejm200105103441904. PubMed PMID: 11346808.

19. Vahle JL, Sato M, Long GG, Young JK, Francis PC, Engelhardt JA, Westmore MS, Linda Y, Nold JB. Skeletal changes in rats given daily subcutaneous injections of recombinant human parathyroid hormone (1-34) for 2 years and relevance to human safety. Toxicologic pathology. 2002;30(3):312-21. Epub 2002/06/08. doi: 10.1080/01926230252929882. PubMed PMID: 12051548.

20. Minear S, Leucht P, Jiang J, Liu B, Zeng A, Fuerer C, Nusse R, Helms JA. Wnt proteins promote bone regeneration. Science translational medicine. 2010;2(29):29ra30. Epub 2010/04/30. doi: 10.1126/scitranslmed.3000231. PubMed PMID: 20427820.

21. Wagner ER, Zhu G, Zhang BQ, Luo Q, Shi Q, Huang E, Gao Y, Gao JL, Kim SH, Rastegar F, Yang K, He BC, Chen L, Zuo GW, Bi Y, Su Y, Luo J, Luo X, Huang J, Deng ZL, Reid RR, Luu HH, Haydon RC, He TC. The therapeutic potential of the Wnt signaling pathway in bone disorders. Current molecular pharmacology. 2011;4(1):14-25. Epub 2010/09/10. PubMed PMID: 20825362.

22. Behrens J, von Kries JP, Kuhl M, Bruhn L, Wedlich D, Grosschedl R, Birchmeier W. Functional interaction of beta-catenin with the transcription factor LEF-1. Nature. 1996;382(6592):638-42. Epub 1996/08/15. doi: 10.1038/382638a0. PubMed PMID: 8757136.

23. He TC, Sparks AB, Rago C, Hermeking H, Zawel L, da Costa LT, Morin PJ, Vogelstein B, Kinzler KW. Identification of c-MYC as a target of the APC pathway. Science (New York, NY). 1998;281(5382):1509-12. Epub 1998/09/04. PubMed PMID: 9727977.

24. Tetsu O, McCormick F. Beta-catenin regulates expression of cyclin D1 in colon carcinoma cells. Nature. 1999;398(6726):422-6. Epub 1999/04/14. doi: 10.1038/18884. PubMed PMID: 10201372.

25. Cajanek L, Adlerz L, Bryja V, Arenas E. WNT unrelated activities in commercially available preparations of recombinant WNT3a. Journal of cellular biochemistry. 2010;111(5):1077-9. Epub 2010/07/29. doi: 10.1002/jcb.22771. PubMed PMID: 20665540.

26. Jing L, Lefebvre JL, Gordon LR, Granato M. Wnt signals organize synaptic prepattern and axon guidance through the zebrafish unplugged/MuSK receptor. Neuron. 2009;61(5):721-33. Epub 2009/03/17. doi: 10.1016/j.neuron.2008.12.025. PubMed PMID: 19285469; PMCID: PMC2671566.

27. Willert K, Brown JD, Danenberg E, Duncan AW, Weissman IL, Reya T, Yates JR, 3rd, Nusse R. Wnt proteins are lipid-modified and can act as stem cell growth factors. Nature. 2003;423(6938):448-52. Epub 2003/04/30. doi: 10.1038/nature01611. PubMed PMID: 12717451.

28. Franch-Marro X, Wendler F, Griffith J, Maurice MM, Vincent JP. In vivo role of lipid adducts on Wingless. Journal of cell science. 2008;121(Pt 10):1587-92. Epub 2008/04/24. doi: 10.1242/jcs.015958. PubMed PMID: 18430784.

29. Morrell NT, Leucht P, Zhao L, Kim JB, ten Berge D, Ponnusamy K, Carre AL, Dudek H, Zachlederova M, McElhaney M, Brunton S, Gunzner J, Callow M, Polakis P, Costa M, Zhang XM, Helms JA, Nusse R. Liposomal packaging generates Wnt protein with in vivo biological activity. PloS one. 2008;3(8):e2930. Epub 2008/08/14. doi: 10.1371/journal.pone.0002930. PubMed PMID: 18698373; PMCID: PMC2515347.

30. Hoeppner LH, Secreto FJ, Westendorf JJ. Wnt signaling as a therapeutic target for bone diseases. Expert opinion on therapeutic targets. 2009;13(4):485-96. Epub 2009/04/02. doi: 10.1517/14728220902841961. PubMed PMID: 19335070; PMCID: PMC3023986.

31. Lang T, LeBlanc A, Evans H, Lu Y, Genant H, Yu A. Cortical and trabecular bone mineral loss from the spine and hip in long-duration spaceflight. Journal of bone and mineral research : the official journal of the American Society for Bone and Mineral Research. 2004;19(6):1006-12. Epub 2004/05/06. doi: 10.1359/jbmr.040307. PubMed PMID: 15125798.

32. LeBlanc A, Lin C, Shackelford L, Sinitsyn V, Evans H, Belichenko O, Schenkman B, Kozlovskaya I, Oganov V, Bakulin A, Hedrick T, Feeback D. Muscle volume, MRI relaxation times (T2), and body composition after spaceflight. Journal of applied physiology (Bethesda, Md : 1985). 2000;89(6):2158-64. Epub 2000/11/25. doi: 10.1152/jappl.2000.89.6.2158. PubMed PMID: 11090562.

33. LeBlanc A, Schneider V, Shackelford L, West S, Oganov V, Bakulin A, Voronin L. Bone mineral and lean tissue loss after long duration space flight. Journal of musculoskeletal & neuronal interactions. 2000;1(2):157-60. Epub 2005/03/11. PubMed PMID: 15758512.

34. McCarthy I, Goodship A, Herzog R, Oganov V, Stussi E, Vahlensieck M. Investigation of bone changes in microgravity during long and short duration space flight: comparison of techniques. European journal of clinical investigation. 2000;30(12):1044-54. Epub 2000/12/21. PubMed PMID: 11122319.

35. Kanis JA, Johnell O, Oden A, Sembo I, Redlund-Johnell I, Dawson A, De Laet C, Jonsson B. Long-term risk of osteoporotic fracture in Malmo. Osteoporosis international : a journal established as result of cooperation between the European Foundation for Osteoporosis and the

National Osteoporosis Foundation of the USA. 2000;11(8):669-74. Epub 2000/11/30. PubMed PMID: 11095169.

36. Melton LJ, 3rd, Atkinson EJ, O'Connor MK, O'Fallon WM, Riggs BL. Bone density and fracture risk in men. Journal of bone and mineral research : the official journal of the American Society for Bone and Mineral Research. 1998;13(12):1915-23. Epub 1998/12/09. doi: 10.1359/jbmr.1998.13.12.1915. PubMed PMID: 9844110.

37. Melton LJ, 3rd, Chrischilles EA, Cooper C, Lane AW, Riggs BL. Perspective. How many women have osteoporosis? Journal of bone and mineral research : the official journal of the American Society for Bone and Mineral Research. 1992;7(9):1005-10. Epub 1992/09/01. doi: 10.1002/jbmr.5650070902. PubMed PMID: 1414493.

38. Lang T, Van Loon J, Bloomfield S, Vico L, Chopard A, Rittweger J, Kyparos A, Blottner D, Vuori I, Gerzer R, Cavanagh PR. Towards human exploration of space: the THESEUS review series on muscle and bone research priorities. NPJ microgravity. 2017;3:8. Epub 2017/06/27. doi: 10.1038/s41526-017-0013-0. PubMed PMID: 28649630; PMCID: PMC5445590.

39. Ohshima H. [Bone loss and bone metabolism in astronauts during long-duration space flight]. Clinical calcium. 2006;16(1):81-5. Epub 2006/01/07. doi: CliCa06018185. PubMed PMID: 16397355.

40. Blaber E, Sato K, Almeida EA. Stem cell health and tissue regeneration in microgravity. Stem cells and development. 2014;23 Suppl 1:73-8. Epub 2014/12/03. doi: 10.1089/scd.2014.0408. PubMed PMID: 25457968; PMCID: PMC4235978.

41. Blaber EA, Finkelstein H, Dvorochkin N, Sato KY, Yousuf R, Burns BP, Globus RK, Almeida EA. Microgravity Reduces the Differentiation and Regenerative Potential of Embryonic

Stem Cells. Stem cells and development. 2015;24(22):2605-21. Epub 2015/09/29. doi: 10.1089/scd.2015.0218. PubMed PMID: 26414276; PMCID: PMC4652210.

42. Di Giulio C. Do we age faster in absence of gravity? Frontiers in physiology. 2013;4:134. Epub 2013/06/14. doi: 10.3389/fphys.2013.00134. PubMed PMID: 23760280; PMCID: PMC3672673.

43. Ting K, Vastardis H, Mulliken JB, Soo C, Tieu A, Do H, Kwong E, Bertolami CN, Kawamoto H, Kuroda S, Longaker MT. Human NELL-1 expressed in unilateral coronal synostosis. Journal of bone and mineral research : the official journal of the American Society for Bone and Mineral Research. 1999;14(1):80-9. Epub 1999/01/20. doi: 10.1359/jbmr.1999.14.1.80. PubMed PMID: 9893069.

44. Zhang X, Zara J, Siu RK, Ting K, Soo C. The role of NELL-1, a growth factor associated with craniosynostosis, in promoting bone regeneration. Journal of dental research. 2010;89(9):865-78. Epub 2010/07/22. doi: 10.1177/0022034510376401. PubMed PMID: 20647499; PMCID: PMC2959101.

45. Aghaloo T, Cowan CM, Chou YF, Zhang X, Lee H, Miao S, Hong N, Kuroda S, Wu B, Ting K, Soo C. Nell-1-induced bone regeneration in calvarial defects. The American journal of pathology. 2006;169(3):903-15. Epub 2006/08/29. doi: 10.2353/ajpath.2006.051210. PubMed PMID: 16936265; PMCID: PMC1698834.

46. Aghaloo T, Jiang X, Soo C, Zhang Z, Zhang X, Hu J, Pan H, Hsu T, Wu B, Ting K, Zhang X. A study of the role of nell-1 gene modified goat bone marrow stromal cells in promoting new bone formation. Molecular therapy : the journal of the American Society of Gene Therapy. 2007;15(10):1872-80. Epub 2007/07/27. doi: 10.1038/sj.mt.6300270. PubMed PMID: 17653100; PMCID: PMC2705762.

47. Cowan CM, Zhang X, James AW, Kim TM, Sun N, Wu B, Ting K, Soo C. NELL-1 increases pre-osteoblast mineralization using both phosphate transporter Pit1 and Pit2. Biochemical and biophysical research communications. 2012;422(3):351-7. Epub 2012/05/15. doi: 10.1016/j.bbrc.2012.04.077. PubMed PMID: 22580275.

48. Kwak J, Zara JN, Chiang M, Ngo R, Shen J, James AW, Le KM, Moon C, Zhang X, Gou Z, Ting K, Soo C. NELL-1 injection maintains long-bone quantity and quality in an ovariectomy-induced osteoporotic senile rat model. Tissue engineering Part A. 2013;19(3-4):426-36. Epub 2012/10/23. doi: 10.1089/ten.TEA.2012.0042. PubMed PMID: 23083222; PMCID: PMC3542871.

49. Li W, Lee M, Whang J, Siu RK, Zhang X, Liu C, Wu BM, Wang JC, Ting K, Soo C. Delivery of lyophilized Nell-1 in a rat spinal fusion model. Tissue engineering Part A. 2010;16(9):2861-70. Epub 2010/06/10. doi: 10.1089/ten.tea.2009.0550. PubMed PMID: 20528102; PMCID: PMC2928135.

50. Lu SS, Zhang X, Soo C, Hsu T, Napoli A, Aghaloo T, Wu BM, Tsou P, Ting K, Wang JC. The osteoinductive properties of Nell-1 in a rat spinal fusion model. The spine journal : official journal of the North American Spine Society. 2007;7(1):50-60. Epub 2007/01/02. doi: 10.1016/j.spinee.2006.04.020. PubMed PMID: 17197333.

51. Siu RK, Lu SS, Li W, Whang J, McNeill G, Zhang X, Wu BM, Turner AS, Seim HB, 3rd, Hoang P, Wang JC, Gertzman AA, Ting K, Soo C. Nell-1 protein promotes bone formation in a sheep spinal fusion model. Tissue engineering Part A. 2011;17(7-8):1123-35. Epub 2010/12/07. doi: 10.1089/ten.TEA.2010.0486. PubMed PMID: 21128865; PMCID: PMC3063712.

52. Karasik D, Hsu YH, Zhou Y, Cupples LA, Kiel DP, Demissie S. Genome-wide pleiotropy of osteoporosis-related phenotypes: the Framingham Study. Journal of bone and mineral research :

the official journal of the American Society for Bone and Mineral Research. 2010;25(7):1555-63. Epub 2010/03/05. doi: 10.1002/jbmr.38. PubMed PMID: 20200953; PMCID: PMC3153998.

53. James AW, Shen J, Zhang X, Asatrian G, Goyal R, Kwak JH, Jiang L, Bengs B, Culiat CT, Turner AS, Seim Iii HB, Wu BM, Lyons K, Adams JS, Ting K, Soo C. NELL-1 in the treatment of osteoporotic bone loss. Nature communications. 2015;6:7362. Epub 2015/06/18. doi: 10.1038/ncomms8362. PubMed PMID: 26082355; PMCID: PMC4557288.

54. Aghaloo T, Cowan CM, Zhang X, Freymiller E, Soo C, Wu B, Ting K, Zhang Z. The effect of NELL1 and bone morphogenetic protein-2 on calvarial bone regeneration. Journal of oral and maxillofacial surgery : official journal of the American Association of Oral and Maxillofacial Surgeons. 2010;68(2):300-8. Epub 2010/02/02. doi: 10.1016/j.joms.2009.03.066. PubMed PMID: 20116699; PMCID: PMC3113462.

55. Zhang X, Ting K, Bessette CM, Culiat CT, Sung SJ, Lee H, Chen F, Shen J, Wang JJ, Kuroda S, Soo C. Nell-1, a key functional mediator of Runx2, partially rescues calvarial defects in Runx2(+/-) mice. Journal of bone and mineral research : the official journal of the American Society for Bone and Mineral Research. 2011;26(4):777-91. Epub 2010/10/13. doi: 10.1002/jbmr.267. PubMed PMID: 20939017; PMCID: PMC3179324.

56. Li W, Zara JN, Siu RK, Lee M, Aghaloo T, Zhang X, Wu BM, Gertzman AA, Ting K, Soo C. Nell-1 enhances bone regeneration in a rat critical-sized femoral segmental defect model. Plastic and reconstructive surgery. 2011;127(2):580-7. Epub 2011/02/03. doi: 10.1097/PRS.0b013e3181fed5ae. PubMed PMID: 21285762; PMCID: PMC3089952.

57. James AW, Shen J, Tsuei R, Nguyen A, Khadarian K, Meyers CA, Pan HC, Li W, Kwak JH, Asatrian G, Culiat CT, Lee M, Ting K, Zhang X, Soo C. NELL-1 induces Sca-1+ mesenchymal

progenitor cell expansion in models of bone maintenance and repair. JCI insight. 2017;2(12). Epub 2017/06/15. doi: 10.1172/jci.insight.92573. PubMed PMID: 28614787; PMCID: PMC5470886.

58. Tang R, Wang Q, Du J, Yang P, Wang X. Expression and localization of Nell-1 during murine molar development. Journal of molecular histology. 2013;44(2):175-81. Epub 2012/12/25. doi: 10.1007/s10735-012-9472-5. PubMed PMID: 23264108.

59. Zhu S, Zhang B, Man C, Ma Y, Hu J. NEL-like molecule-1-modified bone marrow mesenchymal stem cells/poly lactic-co-glycolic acid composite improves repair of large osteochondral defects in mandibular condyle. Osteoarthritis and cartilage. 2011;19(6):743-50. Epub 2011/03/03. doi: 10.1016/j.joca.2011.02.015. PubMed PMID: 21362490.

60. James AW, Pan A, Chiang M, Zara JN, Zhang X, Ting K, Soo C. A new function of Nell-1 protein in repressing adipogenic differentiation. Biochemical and biophysical research communications. 2011;411(1):126-31. Epub 2011/07/05. doi: 10.1016/j.bbrc.2011.06.111. PubMed PMID: 21723263; PMCID: PMC3166249.

61. Zhang X, Carpenter D, Bokui N, Soo C, Miao S, Truong T, Wu B, Chen I, Vastardis H, Tanizawa K, Kuroda S, Ting K. Overexpression of Nell-1, a craniosynostosis-associated gene, induces apoptosis in osteoblasts during craniofacial development. Journal of bone and mineral research : the official journal of the American Society for Bone and Mineral Research. 2003;18(12):2126-34. Epub 2003/12/16. doi: 10.1359/jbmr.2003.18.12.2126. PubMed PMID: 14672347.

62. Zhang X, Kuroda S, Carpenter D, Nishimura I, Soo C, Moats R, Iida K, Wisner E, Hu FY, Miao S, Beanes S, Dang C, Vastardis H, Longaker M, Tanizawa K, Kanayama N, Saito N, Ting K. Craniosynostosis in transgenic mice overexpressing Nell-1. The Journal of clinical investigation.

2002;110(6):861-70. Epub 2002/09/18. doi: 10.1172/jci15375. PubMed PMID: 12235118; PMCID: PMC151127.

63. Shen J, James AW, Chung J, Lee K, Zhang JB, Ho S, Lee KS, Kim TM, Niimi T, Kuroda S, Ting K, Soo C. NELL-1 promotes cell adhesion and differentiation via Integrinbeta1. Journal of cellular biochemistry. 2012;113(12):3620-8. Epub 2012/07/19. doi: 10.1002/jcb.24253. PubMed PMID: 22807400.

64. Li C, Zheng Z, Ha P, Chen X, Jiang W, Sun S, Chen F, Asatrian G, Berthiaume EA, Kim JK, Chen EC, Pang S, Zhang X, Ting K, Soo C. Neurexin Superfamily Cell Membrane Receptor Contactin-Associated Protein Like-4 (Cntnap4) Is Involved in Neural EGFL-Like 1 (Nell-1)-Responsive Osteogenesis. Journal of bone and mineral research : the official journal of the American Society for Bone and Mineral Research. 2018;33(10):1813-25. Epub 2018/06/16. doi: 10.1002/jbmr.3524. PubMed PMID: 29905970; PMCID: PMC6390490.

65. Glantschnig H, Scott K, Hampton R, Wei N, McCracken P, Nantermet P, Zhao JZ, Vitelli S, Huang L, Haytko P, Lu P, Fisher JE, Sandhu P, Cook J, Williams D, Strohl W, Flores O, Kimmel D, Wang F, An Z. A rate-limiting role for Dickkopf-1 in bone formation and the remediation of bone loss in mouse and primate models of postmenopausal osteoporosis by an experimental therapeutic antibody. The Journal of pharmacology and experimental therapeutics. 2011;338(2):568-78. Epub 2011/05/03. doi: 10.1124/jpet.111.181404. PubMed PMID: 21531794.

66. Jevsevar S, Kunstelj M, Porekar VG. PEGylation of therapeutic proteins. Biotechnology journal. 2010;5(1):113-28. Epub 2010/01/14. doi: 10.1002/biot.200900218. PubMed PMID: 20069580.

67. Levy Y, Hershfield MS, Fernandez-Mejia C, Polmar SH, Scudiery D, Berger M, Sorensen RU. Adenosine deaminase deficiency with late onset of recurrent infections: response to treatment

with polyethylene glycol-modified adenosine deaminase. The Journal of pediatrics. 1988;113(2):312-7. Epub 1988/08/01. PubMed PMID: 3260944.

68. Ng EW, Shima DT, Calias P, Cunningham ET, Jr., Guyer DR, Adamis AP. Pegaptanib, a targeted anti-VEGF aptamer for ocular vascular disease. Nature reviews Drug discovery. 2006;5(2):123-32. Epub 2006/03/07. doi: 10.1038/nrd1955. PubMed PMID: 16518379.

69. Bansal R, Post E, Proost JH, de Jager-Krikken A, Poelstra K, Prakash J. PEGylation improves pharmacokinetic profile, liver uptake and efficacy of Interferon gamma in liver fibrosis. Journal of controlled release : official journal of the Controlled Release Society. 2011;154(3):233-40. Epub 2011/06/15. doi: 10.1016/j.jconrel.2011.05.027. PubMed PMID: 21664391.

70. Kwak JH, Zhang Y, Park J, Chen E, Shen J, Chawan C, Tanjaya J, Lee S, Zhang X, Wu BM, Ting K, Soo C. Pharmacokinetics and osteogenic potential of PEGylated NELL-1 in vivo after systemic administration. Biomaterials. 2015;57:73-83. Epub 2015/04/29. doi: 10.1016/j.biomaterials.2015.03.063. PubMed PMID: 25913252; PMCID: PMC4426150.

71. Hirabayashi H, Fujisaki J. Bone-specific drug delivery systems: approaches via chemical modification of bone-seeking agents. Clinical pharmacokinetics. 2003;42(15):1319-30. Epub 2003/12/17. doi: 10.2165/00003088-200342150-00002. PubMed PMID: 14674786.

72. Talmage RV. Morphological and physiological considerations in a new concept of calcium transport in bone. The American journal of anatomy. 1970;129(4):467-76. Epub 1970/12/01. doi: 10.1002/aja.1001290408. PubMed PMID: 5493823.

73. Azuma Y, Sato H, Oue Y, Okabe K, Ohta T, Tsuchimoto M, Kiyoki M. Alendronate distributed on bone surfaces inhibits osteoclastic bone resorption in vitro and in experimental hypercalcemia models. Bone. 1995;16(2):235-45. Epub 1995/02/01. PubMed PMID: 7756053.

74. Fleisch H, Russell RG, Francis MD. Diphosphonates inhibit hydroxyapatite dissolution in vitro and bone resorption in tissue culture and in vivo. Science (New York, NY). 1969;165(3899):1262-4. Epub 1969/09/19. PubMed PMID: 5803538.

75. Reynolds JJ, Minkin C, Morgan DB, Spycher D, Fleisch H. The effect of two diphosphonates on the resorption of mouse calvaria in vitro. Calcified tissue research. 1972;10(4):302-13. Epub 1972/01/01. PubMed PMID: 4345096.

76. Rogers MJ, Gordon S, Benford HL, Coxon FP, Luckman SP, Monkkonen J, Frith JC. Cellular and molecular mechanisms of action of bisphosphonates. Cancer. 2000;88(12 Suppl):2961-78. Epub 2000/07/18. PubMed PMID: 10898340.

77. Russell RG, Bisaz S, Fleisch H, Currey HL, Rubinstein HM, Dietz AA, Boussina I, Micheli A, Fallet G. Inorganic pyrophosphate in plasma, urine, and synovial fluid of patients with pyrophosphate arthropathy (chondrocalcinosis or pseudogout). Lancet (London, England). 1970;2(7679):899-902. Epub 1970/10/31. PubMed PMID: 4097282.

78. Lin JH. Bisphosphonates: a review of their pharmacokinetic properties. Bone. 1996;18(2):75-85. Epub 1996/02/01. PubMed PMID: 8833200.

79. Myers HM. Structure-activity relationships (SAR) of hydroxyapatite-binding molecules. Calcified tissue international. 1987;40(6):344-8. doi: 10.1007/BF02556697.

80. Bisaz S, Jung A, Fleisch H. Uptake by bone of pyrophosphate, diphosphonates and their technetium derivatives. Clinical science and molecular medicine. 1978;54(3):265-72. Epub 1978/03/01. PubMed PMID: 204442.

81. Miller SC, Jee WS. The effect of dichloromethylene diphosphonate, a pyrophosphate analog, on bone and bone cell structure in the growing rat. The Anatomical record. 1979;193(3):439-62. Epub 1979/03/01. doi: 10.1002/ar.1091930309. PubMed PMID: 154858.

82. Murakami H, Takahashi N, Sasaki T, Udagawa N, Tanaka S, Nakamura I, Zhang D, Barbier A, Suda T. A possible mechanism of the specific action of bisphosphonates on osteoclasts: tiludronate preferentially affects polarized osteoclasts having ruffled borders. Bone. 1995;17(2):137-44. Epub 1995/08/01. PubMed PMID: 8554921.

83. Plasmans CM, Jap PH, Kuijpers W, Slooff TJ. Influence of a diphosphonate on the cellular aspect of young bone tissue. Calcified tissue international. 1980;32(3):247-66. Epub 1980/01/01. PubMed PMID: 6775793.

84. Rowe EJ, Hausmann E. The alteration of osteoclast morphology by diphosphonates in bone organ culture. Calcified tissue research. 1976;20(1):53-60. Epub 1976/04/13. PubMed PMID: 1260493.

85. Sato M, Grasser W. Effects of bisphosphonates on isolated rat osteoclasts as examined by reflected light microscopy. Journal of bone and mineral research : the official journal of the American Society for Bone and Mineral Research. 1990;5(1):31-40. Epub 1990/01/01. doi: 10.1002/jbmr.5650050107. PubMed PMID: 2106763.

86. Schenk R, Merz WA, Muhlbauer R, Russell RG, Fleisch H. Effect of ethane-1-hydroxy-1,1-diphosphonate (EHDP) and dichloromethylene diphosphonate (Cl 2 MDP) on the calcification and resorption of cartilage and bone in the tibial epiphysis and metaphysis of rats. Calcified tissue research. 1973;11(3):196-214. Epub 1973/03/12. PubMed PMID: 4707191.

87. Hiroi-Furuya E, Kameda T, Hiura K, Mano H, Miyazawa K, Nakamaru Y, Watanabe-Mano M, Okuda N, Shimada J, Yamamoto Y, Hakeda Y, Kumegawa M. Etidronate (EHDP) inhibits osteoclastic-bone resorption, promotes apoptosis and disrupts actin rings in isolate-mature osteoclasts. Calcified tissue international. 1999;64(3):219-23. Epub 1999/02/19. PubMed PMID: 10024379.

88. Sato M, Grasser W, Endo N, Akins R, Simmons H, Thompson DD, Golub E, Rodan GA. Bisphosphonate action. Alendronate localization in rat bone and effects on osteoclast ultrastructure. The Journal of clinical investigation. 1991;88(6):2095-105. Epub 1991/12/01. doi: 10.1172/jci115539. PubMed PMID: 1661297; PMCID: PMC295810.

89. Selander K, Lehenkari P, Vaananen HK. The effects of bisphosphonates on the resorption cycle of isolated osteoclasts. Calcified tissue international. 1994;55(5):368-75. Epub 1994/11/01. PubMed PMID: 7532540.

90. Rogers MJ, Crockett JC, Coxon FP, Monkkonen J. Biochemical and molecular mechanisms of action of bisphosphonates. Bone. 2011;49(1):34-41. Epub 2010/11/30. doi: 10.1016/j.bone.2010.11.008. PubMed PMID: 21111853.

91. Benford HL, McGowan NW, Helfrich MH, Nuttall ME, Rogers MJ. Visualization of bisphosphonate-induced caspase-3 activity in apoptotic osteoclasts in vitro. Bone. 2001;28(5):465-73. Epub 2001/05/10. PubMed PMID: 11344045.

92. Halasy-Nagy JM, Rodan GA, Reszka AA. Inhibition of bone resorption by alendronate and risedronate does not require osteoclast apoptosis. Bone. 2001;29(6):553-9. Epub 2001/12/01. PubMed PMID: 11728926.

93. Lehenkari PP, Kellinsalmi M, Napankangas JP, Ylitalo KV, Monkkonen J, Rogers MJ, Azhayev A, Vaananen HK, Hassinen IE. Further insight into mechanism of action of clodronate: inhibition of mitochondrial ADP/ATP translocase by a nonhydrolyzable, adenine-containing metabolite. Molecular pharmacology. 2002;61(5):1255-62. Epub 2002/04/19. PubMed PMID: 11961144.

94. Selander KS, Monkkonen J, Karhukorpi EK, Harkonen P, Hannuniemi R, Vaananen HK. Characteristics of clodronate-induced apoptosis in osteoclasts and macrophages. Molecular pharmacology. 1996;50(5):1127-38. Epub 1996/11/01. PubMed PMID: 8913344.

95. Sutherland KA, Rogers HL, Tosh D, Rogers MJ. RANKL increases the level of Mcl-1 in osteoclasts and reduces bisphosphonate-induced osteoclast apoptosis in vitro. Arthritis research & therapy. 2009;11(2):R58. Epub 2009/05/02. doi: 10.1186/ar2681. PubMed PMID: 19405951; PMCID: PMC2688211.

96. Bergstrom JD, Bostedor RG, Masarachia PJ, Reszka AA, Rodan G. Alendronate is a specific, nanomolar inhibitor of farnesyl diphosphate synthase. Archives of biochemistry and biophysics. 2000;373(1):231-41. Epub 2000/01/06. doi: 10.1006/abbi.1999.1502. PubMed PMID: 10620343.

97. Keller RK, Fliesler SJ. Mechanism of aminobisphosphonate action: characterization of alendronate inhibition of the isoprenoid pathway. Biochemical and biophysical research communications. 1999;266(2):560-3. Epub 1999/12/22. doi: 10.1006/bbrc.1999.1849. PubMed PMID: 10600541.

98. Mitrofan LM, Pelkonen J, Monkkonen J. The level of ATP analog and isopentenyl pyrophosphate correlates with zoledronic acid-induced apoptosis in cancer cells in vitro. Bone. 2009;45(6):1153-60. Epub 2009/08/25. doi: 10.1016/j.bone.2009.08.010. PubMed PMID: 19699819.

99. van Beek E, Pieterman E, Cohen L, Lowik C, Papapoulos S. Nitrogen-containing bisphosphonates inhibit isopentenyl pyrophosphate isomerase/farnesyl pyrophosphate synthase activity with relative potencies corresponding to their antiresorptive potencies in vitro and in vivo.

Biochemical and biophysical research communications. 1999;255(2):491-4. Epub 1999/03/02. doi: 10.1006/bbrc.1999.0224. PubMed PMID: 10049736.

100. Fleisch H. Bisphosphonates: a new class of drugs in diseases of bone and calcium metabolism. Recent results in cancer research Fortschritte der Krebsforschung Progres dans les recherches sur le cancer. 1989;116:1-28. Epub 1989/01/01. PubMed PMID: 2669065.

101. Drake MT, Clarke BL, Khosla S. Bisphosphonates: mechanism of action and role in clinical practice. Mayo Clinic proceedings. 2008;83(9):1032-45. Epub 2008/09/09. doi: 10.4065/83.9.1032. PubMed PMID: 18775204; PMCID: PMC2667901.

102. Russell RG. Bisphosphonates: from bench to bedside. Annals of the New York Academy of Sciences. 2006;1068:367-401. Epub 2006/07/13. doi: 10.1196/annals.1346.041. PubMed PMID: 16831938.

103. Dunford JE, Thompson K, Coxon FP, Luckman SP, Hahn FM, Poulter CD, Ebetino FH, Rogers MJ. Structure-activity relationships for inhibition of farnesyl diphosphate synthase in vitro and inhibition of bone resorption in vivo by nitrogen-containing bisphosphonates. The Journal of pharmacology and experimental therapeutics. 2001;296(2):235-42. Epub 2001/02/13. PubMed PMID: 11160603.

104. Dunford JE, Kwaasi AA, Rogers MJ, Barnett BL, Ebetino FH, Russell RG, Oppermann U, Kavanagh KL. Structure-activity relationships among the nitrogen containing bisphosphonates in clinical use and other analogues: time-dependent inhibition of human farnesyl pyrophosphate synthase. Journal of medicinal chemistry. 2008;51(7):2187-95. Epub 2008/03/11. doi: 10.1021/jm7015733. PubMed PMID: 18327899.

105. Shi J, Lee S, Uyeda M, Tanjaya J, Kim JK, Pan HC, Reese P, Stodieck L, Lin A, Ting K, Kwak JH, Soo C. Guidelines for Dual Energy X-Ray Absorptiometry Analysis of Trabecular

Bone-Rich Regions in Mice: Improved Precision, Accuracy, and Sensitivity for Assessing Longitudinal Bone Changes. Tissue engineering Part C, Methods. 2016;22(5):451-63. Epub 2016/03/10. doi: 10.1089/ten.TEC.2015.0383. PubMed PMID: 26956416; PMCID: PMC4870654.

106. Parfitt AM, Drezner MK, Glorieux FH, Kanis JA, Malluche H, Meunier PJ, Ott SM, Recker RR. Bone histomorphometry: standardization of nomenclature, symbols, and units. Report of the ASBMR Histomorphometry Nomenclature Committee. Journal of bone and mineral research : the official journal of the American Society for Bone and Mineral Research. 1987;2(6):595-610. Epub 1987/12/01. doi: 10.1002/jbmr.5650020617. PubMed PMID: 3455637.

107. Shiotsuki H, Yoshimi K, Shimo Y, Funayama M, Takamatsu Y, Ikeda K, Takahashi R, Kitazawa S, Hattori N. A rotarod test for evaluation of motor skill learning. Journal of neuroscience methods. 2010;189(2):180-5. Epub 2010/04/03. doi: 10.1016/j.jneumeth.2010.03.026. PubMed PMID: 20359499.

108. Tevlin R, McArdle A, Chan CK, Pluvinage J, Walmsley GG, Wearda T, Marecic O, Hu MS, Paik KJ, Senarath-Yapa K, Atashroo DA, Zielins ER, Wan DC, Weissman IL, Longaker MT. Osteoclast derivation from mouse bone marrow. J Vis Exp. 2014(93):e52056. Epub 2014/11/20. doi: 10.3791/52056. PubMed PMID: 25407120; PMCID: PMC4353410.

109. Zhang Y, Velasco O, Zhang X, Ting K, Soo C, Wu BM. Bioactivity and circulation time of PEGylated NELL-1 in mice and the potential for osteoporosis therapy. Biomaterials. 2014;35(24):6614-21. Epub 2014/05/14. doi: 10.1016/j.biomaterials.2014.04.061. PubMed PMID: 24818884; PMCID: PMC4077898.

110. Beamer WG, Donahue LR, Rosen CJ, Baylink DJ. Genetic variability in adult bone density among inbred strains of mice. Bone. 1996;18(5):397-403. Epub 1996/05/01. PubMed PMID: 8739896.

111. Buie HR, Moore CP, Boyd SK. Postpubertal architectural developmental patterns differ between the L3 vertebra and proximal tibia in three inbred strains of mice. Journal of bone and mineral research : the official journal of the American Society for Bone and Mineral Research. 2008;23(12):2048-59. Epub 2008/08/08. doi: 10.1359/jbmr.080808. PubMed PMID: 18684086.

112. Glatt V, Canalis E, Stadmeyer L, Bouxsein ML. Age-related changes in trabecular architecture differ in female and male C57BL/6J mice. Journal of bone and mineral research : the official journal of the American Society for Bone and Mineral Research. 2007;22(8):1197-207. Epub 2007/05/10. doi: 10.1359/jbmr.070507. PubMed PMID: 17488199.

113. He YX, Zhang G, Pan XH, Liu Z, Zheng LZ, Chan CW, Lee KM, Cao YP, Li G, Wei L, Hung LK, Leung KS, Qin L. Impaired bone healing pattern in mice with ovariectomy-induced osteoporosis: A drill-hole defect model. Bone. 2011;48(6):1388-400. Epub 2011/03/23. doi: 10.1016/j.bone.2011.03.720. PubMed PMID: 21421090.

114. Gargiulo S, Gramanzini M, Megna R, Greco A, Albanese S, Manfredi C, Brunetti A. Evaluation of growth patterns and body composition in C57Bl/6J mice using dual energy X-ray absorptiometry. BioMed research international. 2014;2014:253067. Epub 2014/08/12. doi: 10.1155/2014/253067. PubMed PMID: 25110666; PMCID: PMC4119710.

115. Tanjaya J, Zhang Y, Lee S, Shi J, Chen E, Ang P, Zhang X, Tetradis S, Ting K, Wu B, Soo C, Kwak JH. Efficacy of Intraperitoneal Administration of PEGylated NELL-1 for Bone Formation. BioResearch open access. 2016;5(1):159-70. Epub 2016/06/30. doi: 10.1089/biores.2016.0018. PubMed PMID: 27354930; PMCID: PMC4921932.

116. Woodard G. CHAPTER 9 - Principles in Drug Administration. In: Gay WI, editor. Methods of Animal Experimentation: Academic Press; 1965. p. 343-59.

117. Barbu E. Advanced Drug Delivery. Edited by Ashim K. Mitra, Chi H. Lee, Kun Chen. ChemMedChem. 2015;10(1):209-10. doi: doi:10.1002/cmdc.201402388.

118. Shuid AN, Ibrahim N, Mohd Amin MC, Mohamed IN. Drug delivery systems for prevention and treatment of osteoporotic fracture. Current drug targets. 2013;14(13):1558-64. Epub 2013/11/10. PubMed PMID: 24200294.

119. de Bekker-Grob EW, Essink-Bot ML, Meerding WJ, Pols HA, Koes BW, Steyerberg EW. Patients' preferences for osteoporosis drug treatment: a discrete choice experiment. Osteoporosis international : a journal established as result of cooperation between the European Foundation for Osteoporosis and the National Osteoporosis Foundation of the USA. 2008;19(7):1029-37. Epub 2008/01/15. doi: 10.1007/s00198-007-0535-5. PubMed PMID: 18193329; PMCID: PMC2440927.

120. Bone HG, Hosking D, Devogelaer JP, Tucci JR, Emkey RD, Tonino RP, Rodriguez-Portales JA, Downs RW, Gupta J, Santora AC, Liberman UA. Ten years' experience with alendronate for osteoporosis in postmenopausal women. The New England journal of medicine. 2004;350(12):1189-99. Epub 2004/03/19. doi: 10.1056/NEJMoa030897. PubMed PMID: 15028823.

121. Leu CT, Luegmayr E, Freedman LP, Rodan GA, Reszka AA. Relative binding affinities of bisphosphonates for human bone and relationship to antiresorptive efficacy. Bone. 2006;38(5):628-36. Epub 2005/09/28. doi: 10.1016/j.bone.2005.07.023. PubMed PMID: 16185944.

122. Ebetino FH, Bayless AV, Amburgey J, Ibbotson KJ, Dansereau S, Ebrahimpour A. Elucidation of a Pharmacophore for the Bisphosphonate Mechanism of Bone Antiresorptive Activity. Phosphorus, Sulfur, and Silicon and the Related Elements. 1996;109(1-4):217-20. doi: 10.1080/10426509608545129.

123. Nancollas GH, Tang R, Phipps RJ, Henneman Z, Gulde S, Wu W, Mangood A, Russell RG, Ebetino FH. Novel insights into actions of bisphosphonates on bone: differences in interactions with hydroxyapatite. Bone. 2006;38(5):617-27. Epub 2005/07/28. doi: 10.1016/j.bone.2005.05.003. PubMed PMID: 16046206.

124. Russell RG, Watts NB, Ebetino FH, Rogers MJ. Mechanisms of action of bisphosphonates: similarities and differences and their potential influence on clinical efficacy. Osteoporosis international : a journal established as result of cooperation between the European Foundation for Osteoporosis and the National Osteoporosis Foundation of the USA. 2008;19(6):733-59. Epub 2008/01/25. doi: 10.1007/s00198-007-0540-8. PubMed PMID: 18214569.

125. Uludag H, Yang J. Targeting systemically administered proteins to bone by bisphosphonate conjugation. Biotechnology progress. 2002;18(3):604-11. Epub 2002/06/08. doi: 10.1021/bp0200447. PubMed PMID: 12052079.

126. Uludag H, Kousinioris N, Gao T, Kantoci D. Bisphosphonate conjugation to proteins as a means to impart bone affinity. Biotechnology progress. 2000;16(2):258-67. Epub 2000/04/08. doi: 10.1021/bp990154m. PubMed PMID: 10753453.

127. Kuroda S, Oyasu M, Kawakami M, Kanayama N, Tanizawa K, Saito N, Abe T, Matsuhashi S, Ting K. Biochemical characterization and expression analysis of neural thrombospondin-1-like proteins NELL1 and NELL2. Biochemical and biophysical research communications. 1999;265(1):79-86. Epub 1999/11/05. doi: 10.1006/bbrc.1999.1638. PubMed PMID: 10548494.

128. Butler MG, Rafi SK, Manzardo AM. High-resolution chromosome ideogram representation of currently recognized genes for autism spectrum disorders. International journal of molecular sciences. 2015;16(3):6464-95. Epub 2015/03/25. doi: 10.3390/ijms16036464. PubMed PMID: 25803107; PMCID: PMC4394543.

129. Connolly JJ, Glessner JT, Hakonarson H. A genome-wide association study of autism incorporating autism diagnostic interview-revised, autism diagnostic observation schedule, and social responsiveness scale. Child development. 2013;84(1):17-33. Epub 2012/09/01. doi: 10.1111/j.1467-8624.2012.01838.x. PubMed PMID: 22935194.

130. Zhang L, Guo XQ, Chu JF, Zhang X, Yan ZR, Li YZ. Potential hippocampal genes and pathways involved in Alzheimer's disease: a bioinformatic analysis. Genetics and molecular research : GMR. 2015;14(2):7218-32. Epub 2015/07/01. doi: 10.4238/2015.June.29.15. PubMed PMID: 26125932.

131. Han Y, You X, Xing W, Zhang Z, Zou W. Paracrine and endocrine actions of bone-the functions of secretory proteins from osteoblasts, osteocytes, and osteoclasts. Bone research. 2018;6:16. Epub 2018/05/31. doi: 10.1038/s41413-018-0019-6. PubMed PMID: 29844945; PMCID: PMC5967329.

132. Karsenty G, Olson EN. Bone and Muscle Endocrine Functions: Unexpected Paradigms of Inter-organ Communication. Cell. 2016;164(6):1248-56. Epub 2016/03/12. doi: 10.1016/j.cell.2016.02.043. PubMed PMID: 26967290; PMCID: PMC4797632.

133. Oury F, Khrimian L, Denny CA, Gardin A, Chamouni A, Goeden N, Huang YY, Lee H, Srinivas P, Gao XB, Suyama S, Langer T, Mann JJ, Horvath TL, Bonnin A, Karsenty G. Maternal and offspring pools of osteocalcin influence brain development and functions. Cell. 2013;155(1):228-41. Epub 2013/10/01. doi: 10.1016/j.cell.2013.08.042. PubMed PMID: 24074871; PMCID: PMC3864001.

134. Martin TJ, Sims NA. Osteoclast-derived activity in the coupling of bone formation to resorption. Trends in molecular medicine. 2005;11(2):76-81. Epub 2005/02/08. doi: 10.1016/j.molmed.2004.12.004. PubMed PMID: 15694870.

135. Howard GA, Bottemiller BL, Turner RT, Rader JI, Baylink DJ. Parathyroid hormone stimulates bone formation and resorption in organ culture: evidence for a coupling mechanism. Proceedings of the National Academy of Sciences of the United States of America. 1981;78(5):3204-8. Epub 1981/05/01. PubMed PMID: 6942425; PMCID: PMC319529.

136. Sims NA, Jenkins BJ, Quinn JM, Nakamura A, Glatt M, Gillespie MT, Ernst M, Martin TJ. Glycoprotein 130 regulates bone turnover and bone size by distinct downstream signaling pathways. The Journal of clinical investigation. 2004;113(3):379-89. Epub 2004/02/03. doi: 10.1172/jci19872. PubMed PMID: 14755335; PMCID: PMC324544.

137. Walker EC, McGregor NE, Poulton IJ, Pompolo S, Allan EH, Quinn JM, Gillespie MT, Martin TJ, Sims NA. Cardiotrophin-1 is an osteoclast-derived stimulus of bone formation required for normal bone remodeling. Journal of bone and mineral research : the official journal of the American Society for Bone and Mineral Research. 2008;23(12):2025-32. Epub 2008/07/31. doi: 10.1359/jbmr.080706. PubMed PMID: 18665789.

138. Furuya Y, Inagaki A, Khan M, Mori K, Penninger JM, Nakamura M, Udagawa N, Aoki K, Ohya K, Uchida K, Yasuda H. Stimulation of bone formation in cortical bone of mice treated with a receptor activator of nuclear factor-κB ligand (RANKL)-binding peptide that possesses osteoclastogenesis inhibitory activity. The Journal of biological chemistry. 2013;288(8):5562-71. Epub 2013/01/14. doi: 10.1074/jbc.M112.426080. PubMed PMID: 23319583.

139. Nakagawa H, Takagi K, Kitaoka M, Iyama KI, Usuku G. Influence of monocyte-macrophage lineage cells on alkaline phosphatase activity of developing osteoblasts derived from rat bone marrow stromal cells. Nihon Seikeigeka Gakkai zasshi. 1993;67(5):480-9. Epub 1993/05/01. PubMed PMID: 8336068.

140. Rifas L, Cheng S-L, Shen V, Peck WA. Monokines Produced by Macrophages Stimulate the Growth of Osteoblasts. Connective Tissue Research. 1989;23(2-3):163-78. doi: 10.3109/03008208909002416.

141. Nabavi N, Khandani A, Camirand A, Harrison RE. Effects of microgravity on osteoclast bone resorption and osteoblast cytoskeletal organization and adhesion. Bone. 2011;49(5):965-74. Epub 2011/08/16. doi: 10.1016/j.bone.2011.07.036. PubMed PMID: 21839189.

142. Rucci N, Rufo A, Alamanou M, Teti A. Modeled microgravity stimulates osteoclastogenesis and bone resorption by increasing osteoblast RANKL/OPG ratio. Journal of cellular biochemistry. 2007;100(2):464-73. Epub 2006/08/24. doi: 10.1002/jcb.21059. PubMed PMID: 16927271.

143. Bikle DD, Morey-Holton ER, Doty SB, Currier PA, Tanner SJ, Halloran BP. Alendronate increases skeletal mass of growing rats during unloading by inhibiting resorption of calcified cartilage. Journal of bone and mineral research : the official journal of the American Society for Bone and Mineral Research. 1994;9(11):1777-87. Epub 1994/11/01. doi: 10.1002/jbmr.5650091115. PubMed PMID: 7863829.

144. Machwate M, Zerath E, Holy X, Pastoureau P, Marie PJ. Insulin-like growth factor-I increases trabecular bone formation and osteoblastic cell proliferation in unloaded rats. Endocrinology. 1994;134(3):1031-8. Epub 1994/03/01. doi: 10.1210/endo.134.3.8119139. PubMed PMID: 8119139.

145. Machwate M, Zerath E, Holy X, Hott M, Modrowski D, Malouvier A, Marie PJ. Skeletal unloading in rat decreases proliferation of rat bone and marrow-derived osteoblastic cells. The American journal of physiology. 1993;264(5 Pt 1):E790-9. Epub 1993/05/01. doi: 10.1152/ajpendo.1993.264.5.E790. PubMed PMID: 8498500.

146. Di S, Tian Z, Qian A, Li J, Wu J, Wang Z, Zhang D, Yin D, Brandi ML, Shang P. Large gradient high magnetic field affects FLG29.1 cells differentiation to form osteoclast-like cells. International journal of radiation biology. 2012;88(11):806-13. Epub 2012/05/31. doi: 10.3109/09553002.2012.698365. PubMed PMID: 22642494.

147. Arfat Y, Xiao WZ, Iftikhar S, Zhao F, Li DJ, Sun YL, Zhang G, Shang P, Qian AR. Physiological effects of microgravity on bone cells. Calcified tissue international. 2014;94(6):569-79. Epub 2014/04/02. doi: 10.1007/s00223-014-9851-x. PubMed PMID: 24687524.

148. Zhang J, Niu C, Ye L, Huang H, He X, Tong WG, Ross J, Haug J, Johnson T, Feng JQ, Harris S, Wiedemann LM, Mishina Y, Li L. Identification of the haematopoietic stem cell niche and control of the niche size. Nature. 2003;425(6960):836-41. Epub 2003/10/24. doi: 10.1038/nature02041. PubMed PMID: 14574412.

149. Mendez-Ferrer S, Michurina TV, Ferraro F, Mazloom AR, Macarthur BD, Lira SA, Scadden DT, Ma'ayan A, Enikolopov GN, Frenette PS. Mesenchymal and haematopoietic stem cells form a unique bone marrow niche. Nature. 2010;466(7308):829-34. Epub 2010/08/13. doi: 10.1038/nature09262. PubMed PMID: 20703299; PMCID: PMC3146551.

150. Calvi LM, Adams GB, Weibrecht KW, Weber JM, Olson DP, Knight MC, Martin RP, Schipani E, Divieti P, Bringhurst FR, Milner LA, Kronenberg HM, Scadden DT. Osteoblastic cells regulate the haematopoietic stem cell niche. Nature. 2003;425(6960):841-6. Epub 2003/10/24. doi: 10.1038/nature02040. PubMed PMID: 14574413.

151. Kiel MJ, Yilmaz OH, Iwashita T, Yilmaz OH, Terhorst C, Morrison SJ. SLAM family receptors distinguish hematopoietic stem and progenitor cells and reveal endothelial niches for stem cells. Cell. 2005;121(7):1109-21. Epub 2005/07/02. doi: 10.1016/j.cell.2005.05.026. PubMed PMID: 15989959.

152. Sadie-Van Gijsen H, Crowther NJ, Hough FS, Ferris WF. The interrelationship between bone and fat: from cellular see-saw to endocrine reciprocity. Cellular and molecular life sciences : CMLS. 2013;70(13):2331-49. Epub 2012/11/28. doi: 10.1007/s00018-012-1211-2. PubMed PMID: 23178849.

153. Kawai M, de Paula FJ, Rosen CJ. New insights into osteoporosis: the bone-fat connection. Journal of internal medicine. 2012;272(4):317-29. Epub 2012/06/19. doi: 10.1111/j.1365-2796.2012.02564.x. PubMed PMID: 22702419; PMCID: PMC3634716.

154. Liu Y, Song CY, Wu SS, Liang QH, Yuan LQ, Liao EY. Novel adipokines and bone metabolism. International journal of endocrinology. 2013;2013:895045. Epub 2013/02/23. doi: 10.1155/2013/895045. PubMed PMID: 23431296; PMCID: PMC3575660.

155. Payne MW, Uhthoff HK, Trudel G. Anemia of immobility: caused by adipocyte accumulation in bone marrow. Medical hypotheses. 2007;69(4):778-86. Epub 2007/04/06. doi: 10.1016/j.mehy.2007.01.077. PubMed PMID: 17408874.

156. Trudel G, Payne M, Madler B, Ramachandran N, Lecompte M, Wade C, Biolo G, Blanc S, Hughson R, Bear L, Uhthoff HK. Bone marrow fat accumulation after 60 days of bed rest persisted 1 year after activities were resumed along with hemopoietic stimulation: the Women International Space Simulation for Exploration study. Journal of applied physiology (Bethesda, Md : 1985). 2009;107(2):540-8. Epub 2009/05/30. doi: 10.1152/japplphysiol.91530.2008. PubMed PMID: 19478189.

157. Monica Edwards LA. NASA Twins Study Confirms Preliminary Findings

NASA Human Research Strategic Communications2019 [updated April 3, 2019].

158. Ohayon S, Avni O, Taylor AL, Perona P, Roian Egnor SE. Automated multi-day tracking of marked mice for the analysis of social behaviour. Journal of neuroscience methods.

2013;219(1):10-9. Epub 2013/07/03. doi: 10.1016/j.jneumeth.2013.05.013. PubMed PMID: 23810825; PMCID: PMC3762481.

159. Bouxsein ML, Myers KS, Shultz KL, Donahue LR, Rosen CJ, Beamer WG. Ovariectomy-induced bone loss varies among inbred strains of mice. Journal of bone and mineral research : the official journal of the American Society for Bone and Mineral Research. 2005;20(7):1085-92. Epub 2005/06/09. doi: 10.1359/jbmr.050307. PubMed PMID: 15940361.